POLITECNICO
MILANO 1863

Scuola di Ingegneria Industriale e dell'Informazione
Corso di Laurea Magistrale in Ingegneria Chimica

Kinetic model discrimination for a new Fischer-Tropsch iron catalyst and reactor staging optimization for a Gas to Liquids plant

Relatore: Prof. Flavio Manenti
Correlatori: Prof. Carlo Pirola
Prof. Magne Hillestad

Tesi di Laurea Magistrale di:
Enea Polonini
Matr. 782997

A. A. 2014-2015

Preface

This dissertation has been made possible only through the collaboration between the Politecnico di Milano, the Università degli Studi di Milano and the Norwegian University of Science and Technology.

In particular, the thesis work, first started and carried out for 5 months at the Norwegian University of Science and Technology of Trondheim, has been then finished at the Politecnico di Milano with the support of the Università degli Studi di Milano.

NTNU – Trondheim
Norwegian University of
Science and Technology

POLITECNICO
MILANO 1863

UNIVERSITÀ
DEGLI STUDI
DI MILANO

Sommario

Questa dissertazione ha avuto come obiettivi principali la determinazione di un modello cinetico per un nuovo catalizzatore a base di ferro per la sintesi di Fischer-Tropsch e la massimizzazione dei profitti di un impianto industriale Gas-to-Liquids ottenuta ottimizzando il numero di stadi e la lunghezza del reattore Fischer-Tropsch utilizzato nella simulazione del suddetto impianto.

I dati sperimentali necessari ad individuare il miglior modello cinetico per il catalizzatore considerato sono stati forniti dall'Università degli Studi di Milano. Prima di tutto è stato modellato in MATLAB® il reattore di laboratorio utilizzato per eseguire le prove sperimentali. Grazie a questa simulazione vari modelli cinetici tratti dalla letteratura sono stati messi a confronto; i parametri cinetici di questi modelli sono stati inoltre ottimizzati con una regressione non lineare utilizzando i risultati sperimentali. Il modello cinetico che presentava il minor errore quadratico medio tra risultati simulati e sperimentali è stato quindi scelto come il migliore tra quelli considerati.

Per l'impianto GTL è stato scelto un reattore multitubolare a letto fisso per eseguire la sintesi di Fischer-Tropsch. Questo reattore è stato simulato approfonditamente in MATLAB®, includendo nel modello il calcolo dell'efficienza del catalizzatore e considerando la possibile formazione di una fase liquida, mentre la parte restante dell'impianto GTL è stata invece simulata in Aspen HYSYS®. L'ottimizzazione delle dimensioni e del numero di stadi del reattore Fischer-Tropsch è stata ancora gestita da MATLAB®, ponendo il valore attuale netto del progetto d'impianto GTL come funzione obiettivo da massimizzare.

Parole chiave: Fischer-Tropsch, Gas-to-Liquids, reattore multitubolare, ottimizzazione staging, analisi di profittabilità.

Abstract

This dissertation has had as main objectives the kinetic model discrimination for a new Fischer-Tropsch iron based catalyst and the profit maximization of a Gas-to-Liquids industrial plant by optimizing the size and number of stages of the Fischer-Tropsch reactor used in said plant.

The experimental data necessary to identify the best kinetic model for the considered catalyst have been provided by the Università degli Studi di Milano. Firstly, the laboratory reactor used to run the experimental tests has been modelled in MATLAB®. Thanks to this simulation various kinetic models taken from the literature were compared; the kinetic parameters of these models have also been optimized with a nonlinear regression using the experimental data. The kinetic model that presented the lower mean squared error between simulated and experimental results has been therefore chosen as the best among those considered.

For the GTL plant it has been chosen a multi-tubular fixed bed reactor to perform the Fischer-Tropsch Synthesis. This reactor has been simulated in depth in MATLAB®, including in the model the evaluation of the catalyst efficiency and considering the possible formation of a liquid phase, while the remaining sections of the GTL plant have been instead simulated in Aspen HYSYS®. The optimization of the size and number of stages of the Fischer-Tropsch reactor has been still managed by MATLAB®, setting the net present value of the GTL plant project as objective function to maximize.

Keywords: Fischer-Tropsch, Gas-to-Liquids, multi-tubular reactor, staging optimization, profitability analysis.

Table of Contents

Preface 1

Sommario 3

Abstract 5

List of Figures 10

List of Tables 12

List of Abbreviations 14

1 Literature Study 17

- 1.1 Introduction 17
- 1.2 History of Fischer-Tropsch process 18
- 1.3 Fischer-Tropsch GTL process 19
  - 1.3.1 Syngas production 20
  - 1.3.2 Fischer-Tropsch synthesis 21
  - 1.3.3 Cracking of Fischer-Tropsch products 23
- 1.4 Fischer-Tropsch Thermodynamics 25
- 1.5 Fischer-Tropsch reaction mechanism 27
- 1.6 FT product selectivity 32
  - 1.6.1 Anderson-Schulz-Flory equation 33
- 1.7 FT catalysts 36
  - 1.7.1 Iron FT catalysts 40

1.8 FT plants overview 41

2 Laboratory reactor equipment and results 45

2.1 High loading Fe-supported FT catalysts 45

2.2 FT laboratory plant 47

2.3 Experimental procedure 49

1.8.1 Catalyst loading 50

1.8.2 Catalyst activation 51

1.8.3 Fischer-Tropsch runs 52

2.4 Results and discussion 52

3 Laboratory reactor model and kinetic models discrimination 57

3.1 Laboratory reactor model 57

3.2 Kinetic models 58

3.3 Data regression 61

3.4 Kinetic model discrimination 63

4 Industrial Fischer-Tropsch reactor model 69

4.1 Lumping of hydrocarbon components 69

4.2 Industrial reactor model 71

4.2.1 Heat of reaction 73

4.2.2 Overall heat transfer coefficient 74

4.3 Catalyst pellet model 75

4.4 Vapour-liquid equilibrium 78

5 Industrial plant economic optimization 83

5.1 MATLAB and HYSYS connection 83

5.2 Syngas plant section 86

5.3 Fischer-Tropsch plant section 87

5.4 Profitability analysis 88
5.4.1 Capital expenses 89
5.4.2 Operating expenses 90
5.4.3 Revenues 91
5.4.4 Net Present Value 91
5.5 Economic optimization 93
5.5.1 Calculation of the catalyst effectiveness factor 96
5.5.2 GlobalSearch algorithm 96
5.6 Results and discussion 97
6 Conclusions 101
Bibliography 103
Appendix A – Kinetic Parameters 109
Appendix B – Boston and Britt algorithm 115
Appendix C – Plant Costs 119
Syngas plant section cost 119
Purchased equipment costs 119
Pressure factors 120
Material factors and bare module factors 122
Bare module cost for heat exchangers, process vessels and pumps 122
Bare module cost for the remaining process equipment 123
Appendix D – Program Code 125
MATLAB and HYSYS interface 125
Catalyst effectiveness factor approximation 127

List of Figures

Figure 1.1 - Types of FT reactor in commercial use [12] 23
Figure 1.2 - Refinery volume yields versus FT GTL yields [7] 24
Figure 1.3 - Standard Gibbs free energy of formation of some FTS products [20] 27
Figure 1.4 - Examples of CO activation pathways: (a) direct CO dissociation (carbide mechanism) and (b) H-assisted CO dissociation (carbide mechanism); (c) CO hydrogenation (CO-insertion mechanism) [28] 29
Figure 1.5 - Different steps of the FTS reaction mechanism 30
Figure 1.6 - Paraffin formation step 31
Figure 1.7 - Olefin formation step 31
Figure 1.8 - Anderson-Schulz-Flory mechanism 33
Figure 1.9 - Mass fractions on chain growth probability 34
Figure 1.10 - Molar fractions on chain growth probability 35
Figure 1.11 - Catalytic activity of transition metals in the Fischer-Tropsch reaction [40] 37
Figure 2.1 - Rotavapor used for the catalyst preparation 47
Figure 2.2 - Laboratory plant flowsheet [47] 48
Figure 2.3 - Fischer-Tropsch laboratory equipment 49
Figure 2.4 - Laboratory reactor thermic profile [47] 50
Figure 2.5 - FT reactor internal loading arrangement 51
Figure 2.6 - Experimental results (1) 53
Figure 2.7 - Experimental results (2) 54
Figure 3.1 - Zimmerman and Bukur model results 61
Figure 3.2 - Lox and Froment-Zimmerman and Bukur reactions model results (1) 66
Figure 3.3 - Lox and Froment-Zimmerman and Bukur reactions model results (2) 67
Figure 4.1 - Multi-tubular fixed bed reactor 71

Figure 4.2 - Thermal resistances for a reactor tube 74
Figure 4.3 - Concentration profiles of the reacting components inside the catalytic pellet ...77
Figure 4.4 - Flash separator 78
Figure 5.1 - C_{11+} lump function 84
Figure 5.2 - $C_{5\text{-}10}$ lump function 85
Figure 5.3 - Syngas plant section 86
Figure 5.4 - Fischer-Tropsch plant section......88
Figure 5.5 - Cash flow model [57]......92
Figure 5.6 - Optimization flow diagram......94
Figure 5.7 - Cumulative sums of the discounted cash flows for the four plant configurations considered 99

List of Tables

Table 1.1 - Comparison of cobalt and iron catalysts [41] 39

Table 2.1 - List of reagents used in the catalyst preparation 46

Table 2.2 - Reaction conditions of the FT experimental runs 52

Table 2.3 - Experimental results at different H_2/CO ratios and temperatures....................... 55

Table 3.1 - FT and WGS reaction sets 62

Table 3.2 - Regressed parameters 63

Table 3.3 - Regression results 64

Table 3.4 - Regressed parameters values for Lox and Froment-Zimmerman and Bukur reactions set... 65

Table 5.1 - Utilities costs 90

Table 5.2 - Raw materials costs.. 91

Table 5.3 - Products costs 91

Table 5.4 - Profitability analysis results of the four plant configurations.............................. 98

Table A.1 - Parameters values for the chain growth probability evaluation 109

Table A.2 - Kinetic parameters of the FT reaction proposed by Zimmerman and Bukur 110

Table A.3 - Kinetic parameters of the WGS reaction proposed by Zimmerman and Bukur ..110

Table A.4 - Kinetic parameters of the first FT reaction proposed by van der Laan and Beenackers 111

Table A.5 - Kinetic parameters of the second FT reaction proposed by van der Laan and Beenackers 111

Table A.6 - Kinetic parameters of the third FT reaction proposed by van der Laan and Beenackers 112

Table A.7 - Kinetic parameters of the first WGS reaction proposed by van der Laan and Beenackers 112

Table A.8 - Kinetic parameters of the second WGS reaction proposed by van der Laan and Beenackers 112

Table C.1 - Equipment costs of the syngas production section 119

Table C.2 - Coefficients values for the purchased cost evaluation 120

Table C.3 – Coefficients values for the pressure factor evaluation 121

Table C.4 – Coefficients values of the bare module factor for heat exchangers, process vessels and pumps 122

Table C.5 - Material factors for heat exchangers, process vessels and pumps 123

Table C.6 – Bare module factors for the remaining process equipment 124

List of Abbreviations

ASF	Anderson-Schulz-Flory
ATR	Auto thermal reforming
BTL	Biomass to Liquids
CAPEX	Capital expenses
CEPCI	Chemical Engineering Plant Cost Index
CTL	Coal to Liquids
DCF	Discounted cash flow
FT	Fischer-Tropsch
FTS	Fischer-Tropsch Synthesis
GTL	Gas to Liquids
HTFT	High temperature Fischer-Tropsch
LPG	Liquid petroleum gas
LTFT	Low temperature Fischer-Tropsch
MOC	Material of construction
MSE	Mean squared error
NPV	Net Present Value
ODE	Ordinary Differential Equation
OPEX	Operative expenses
PDAE	Partial Differential Algebraic Equation

PI	Profitability index
SMR	Steam methane reforming
VLE	Vapour-liquid equilibrium
WGS	Water-gas shift
XTL	Anything to Liquids

1 Literature Study

1.1 Introduction

The climate changes in the last years have raised people's awareness about the threats generated by the emissions released in the atmosphere. The global warming caused by the increase of CO_2 concentration in the atmosphere has therefore led many environmental agencies around the world to impose increasingly demanding limits on exhaust gases, like the control of particulate emissions from diesel engines. Considering also that oil reserves are large but not unlimited, many companies have researched viable alternatives to avoid the flaws of fossil fuels.

Normally diesel fuel is obtained from the fractional distillation of crude oil between 200°C and 350°C under atmospheric pressure, resulting in a mixture of paraffins which typically contain between 8 and 21 carbon atoms per molecule. In these mixtures linear paraffins are highly preferred given their high cetane number and therefore better ignition performance.

Fischer-Tropsch Synthesis (FTS) presents itself as an excellent alternative to the usual production process: starting from syngas (CO and H_2) it can produce a clean diesel oil fraction with high cetane number (generally above 70) without the formation of any sulphur or aromatic compounds.

The aim of this thesis is to evaluate this alternative way to obtain fuel provided by the Fischer-Tropsch (FT) reaction process. First of all, the kinetic model of a Fe-supported FT catalyst studied by the Università degli Studi di Milano has been selected through a discrimination of various kinetic models (whose parameters have been regressed using the provided experimental data). The selected kinetic model, with its regressed parameters, has then been used for the simulation of an industrial FT reactor, which is part of a gas-to-liquids (GTL) plant. Finally, through a reactor sizing and staging optimization, it has been estimated if the considered GTL plant is economically viable.

1.2 History of Fischer-Tropsch process

Hydrocarbon synthesis through hydrogenation of CO on transition metals was discovered in 1902, when Sabatier and Senderens produced methane from a mixture of H_2 and CO using Ni, Fe and Co catalysts [1]. However, the real origin of the Fischer-Tropsch Synthesis dates back to 1923 at the hands of Franz Fischer and Hans Tropsch, two researchers working at the Kaiser Wilhelm Institute of Chemistry. They showed that the synthesis gas, obtained from the gasification of coal and consisting of mainly CO and H_2, reacted on iron, cobalt and nickel catalysts, producing several hydrocarbons at a temperature of 180-200°C and atmospheric pressure [2].

FTS received particular attention for its industrial purposes before and during the Second World War, when Germany needed to become energy independent. In 1938 the first plants with fixed bed reactors were built for the production of hydrocarbons from coal, an abundant raw material in Germany, though these facilities were closed at the end of the war as not economically sustainable [3].

Starting from the 50's South Africa, rich in coal deposits but commercially isolated as a result of the oil embargo during the apartheid era, saw the FTS as a way to free itself from foreign energy resources. Sasol, the South African company created to exploit the coal gasification to produce fuel through the FTS, then built an industrial plant using Fischer-Tropsch technology (using a fluidized bed reactor with a 700×10^3 t/year production). In the following period Sasol continued to study the process of indirect liquefaction of coal, developing new technologies both in the rector design and the catalyst composition and producing waxes and paraffins of high value. In any case, except for some remaining activities in East Germany which lasted until the early 60's, the FT process didn't attract great interest industrially in the post-war period as the oil price put it out of the market.

Later in the 70's, following a sharp rise in oil prices, Sasol developed two new fluidized bed plants with a production capacity of 4200×10^3 t/year, mainly consisting of ethylene and petrol (C_5-C_{10}) [4].

In 1993 Shell built in Bintulu (Malaysia) a FT facility which used syngas obtained by controlled non-catalytic oxidation of methane, to synthetize diesel and waxes. Given the new type of syngas production, the overall process was called gas to liquids (GTL) to distinguish it from the coal to liquids (CTL) process originally used in Germany and South Africa.

Syngas is also obtainable by anaerobic fermentation of landfills, called BTL (biomass to liquids) process; the raw material is lignocellulosic biomass, such as forest wastes and scraps of wood processing, currently used only in a few pilot plants (with less than a 5 t/year productivity). However, BTL installations are much affected by economies of scale, becoming cost-effective only for very large sizes (about 10^6 t/year of biomass) and so making it difficult to supply sufficient raw material.

The FT process has gained interest in recent years because of the continuous oil prices increases; it has been estimated that the FTS should be economically viable at crude oil prices of about 20 $/barrel [5].

Another advantage of this process is the aforementioned lower environmental impact, guaranteed by the substantial absence of aromatics, sulphur and nitrogen-containing compounds in the synthetic fuels obtained, resulting in lower emissions of NO_x and SO_2 in the atmosphere [6].

1.3 Fischer-Tropsch GTL process

The FT GTL process is characterized by three fundamental steps, which require significant supporting infrastructures and a constant supply of feed gas to function effectively [7]:

1. **The synthesis gas (syngas) production**. The methane molecule is reconfigured by steam reforming and/or partial oxidation. Its elements, carbon and hydrogen, are so divided and form syngas, a mixture primarily composed of carbon monoxide and hydrogen.
2. **The Fischer-Tropsch synthesis**. The previously obtained syngas is now processed in FT reactors to synthetize a wide range of paraffinic hydrocarbon products.
3. **The cracking of the FT products**. The crude oil coming from the FTS is refined using conventional refinery cracking processes to produce diesel, naphtha and lube oils for commercial use.

1.3.1 Syngas production

Synthesis gas is usually produced through partial oxidation or steam reforming processes [8]. Syngas is an intermediate feed for many petrochemical processes, including a range of GTL technologies:

- Partial oxidation of methane

$$CH_4 + \frac{1}{2}O_2 \longrightarrow CO + 2H_2 \tag{1.1}$$

  This exothermic reaction requires air separation units to remove the nitrogen from air to guarantee an oxygen-based atmosphere for the process. For this approach is required a combustion chamber operating at high temperatures (1200-1500°C) without catalysts and a special process design to avoid undesired reactions, like the decomposition of methane to carbon black.

  The partial oxidation reactor typically consists of three parts: a burner section where oxygen-only combustion occurs, a heat recovery section and a carbon black removal section (first by water scrubbing, then by extraction with naphtha).

- Steam reforming

$$CH_4 + H_2O \longrightarrow CO + 3H_2 \tag{1.2}$$

It’s an endothermic process widely used to generate the syngas feedstock for other petrochemical processes and for the hydrogen production needed in refinery hydrocrackers. Steam reforming is typically realized in the presence of a metal-based catalyst (nickel dispersed in alumina) at temperatures of 850-940°C and a pressure of about 3 MPa.
The process is usually carried out in tubular, packed reactors with heat recovery from flue gases used to pre-heat the feed gas or to raise steam in waste heat boilers.

- Autothermic synthesis gas production
  In Auto Thermal Reforming (ATR) reactors the syngas production process combines steam reforming and partial oxidation. It takes advantage of the heat produced from partial oxidation to provide the necessary heat for steam reforming. Gases from the partial oxidation burner are mixed with steam and sent to the steam reformer, obtaining an autothermic process. In autothermic reactors the temperature at which the reaction takes place is then maintained by the heat of reaction alone.

1.3.2 Fischer-Tropsch synthesis

The Fischer-Tropsch synthesis is one of the many technologies able to convert carbon and hydrogen components into long chain molecules:

$$\begin{aligned} &nCO+(1+2n)H_2 \longrightarrow C_nH_{(2n+2)}+nH_2O \\ &\Delta H_r \cong -39.4 \quad kcal/mol \end{aligned} \tag{1.3}$$

The overall kinetic scheme involves also other by-products besides water, mainly carbon dioxide coming from the water-gas shift (WGS) equilibrium reaction:

$$\begin{aligned} &CO+H_2O \longleftrightarrow CO_2+H_2 \\ &\Delta H_r \cong -9.9 \quad kcal/mol \end{aligned} \tag{1.4}$$

The FT reaction also competes with the methanation, which has a high heat of reaction:

$$\begin{aligned} &CO+3H_2 \longleftrightarrow CH_4+H_2O \\ &\Delta H_r \cong -49.2 \quad kcal/mol \end{aligned} \tag{1.5}$$

In order to limit methanation and promote the FT reaction, the synthesis is performed at low temperatures of 220-350°C and a pressure of 2-3 MPa. In the reactor selected catalysts (cobalt or iron) promote the growth of long chain hydrocarbon molecules. Many companies hold patents associated with XTL (“anything” to liquids, such as GTL, CTL or BTL processes) catalysts, but only Sasol and Shell have built large-scale commercial plants (GTL production >5000 barrels/day) rather than pilot or demonstration plants. The industry therefore doesn’t grow and the many patents held by few firms act as a high cost barrier to overcome for resource-rich gas companies and countries wishing to use GTL as an alternative way to monetize their gas.

The FT process technologies can be divided into two major categories, a high temperature and a low temperature approach:

- **HTFT** (high temperature Fischer-Tropsch)
  In this process, given the operating conditions and catalysts involved, the syncrude produced includes a high percentage of short chain (<10 carbon atoms) molecules, with a significant presence of propane and butane mixed with their respective olefins. The short chain hydrocarbons are typically extracted from the tail gas stream utilizing cryogenic separation. The resultant lean tail gas is then recycled and mixed with additional feed lean gas for further syngas production [9]. The iron catalysts used for the high-temperature process produce gasoline and diesel which are close to those obtained from conventional oil refining; the resultant GTL fuels are sulphur free, but contain some aromatics. HTFT processes usually run at temperatures of approximately 320°C and a pressures of about 2.5 MPa. In HTFT a conversion efficiency greater than 85% can be reached [10], but not all products are readily usable as transport fuels. HTFT processes are typically conducted in either circulating fluidized bed reactors or fluidized bed reactors [11], shown in Figure 1.1.
- **LTFT** (low temperature Fischer-Tropsch)
  It involves the use of iron or cobalt-based catalysts either in a slurry phase bubble column reactor (e.g. Sasol) or in a multi-tubular fixed bed reactor (e.g. Shell), as depicted in Figure 1.1. LTFT provides a synthetic fraction of diesel virtually free of sulphur and aromatics. The operating conditions for LTFT are temperatures in the 220-

240°C range and pressures of approximately 2-2.5 MPa. Conversion efficiency in LTFT is lower, typically only about 60%, with recycle or reactors operating in series to limit catalysts deactivation [10].

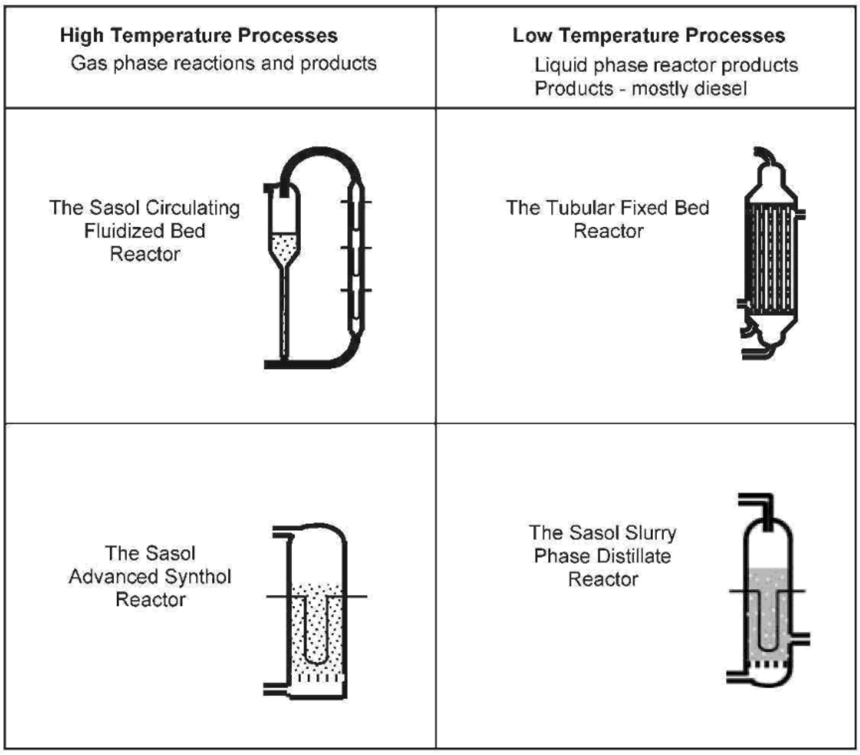
High Temperature Processes
Gas phase reactions and products
Low Temperature Processes
Liquid phase reactor products
Products - mostly diesel
The Sasol Circulating Fluidized Bed Reactor
The Tubular Fixed Bed Reactor
The Sasol Advanced Synthol Reactor
The Sasol Slurry Phase Distillate Reactor

Figure 1.1 - Types of FT reactor in commercial use [12]

In current market condition the main objective of most large-scale technologies is to produce high quality low emissions GTL diesel, jet fuel and naphtha (for petrochemical feedstock or gasoline blending).

1.3.3 Cracking of Fischer-Tropsch products

According to [7] most of the FT GTL plants target the production of diesel fuels (C_{14}-C_{20}), kerosene (C_{10}-C_{13}), naphtha (C_5-C_{10}), lubricants (>C_{50}) and some LPG (C_3-C_4). The mix of hydrocarbons can be altered by adjusting the operating conditions in the FT reactor to target the high-value petroleum products supplied by conventional oil refineries.

However, a typical FT GTL plant has a significantly different yield pattern from a crude oil refinery: the diesel yield of FT GTL plants is about 70%, much higher than the typically 40% of crude oil refineries [13].

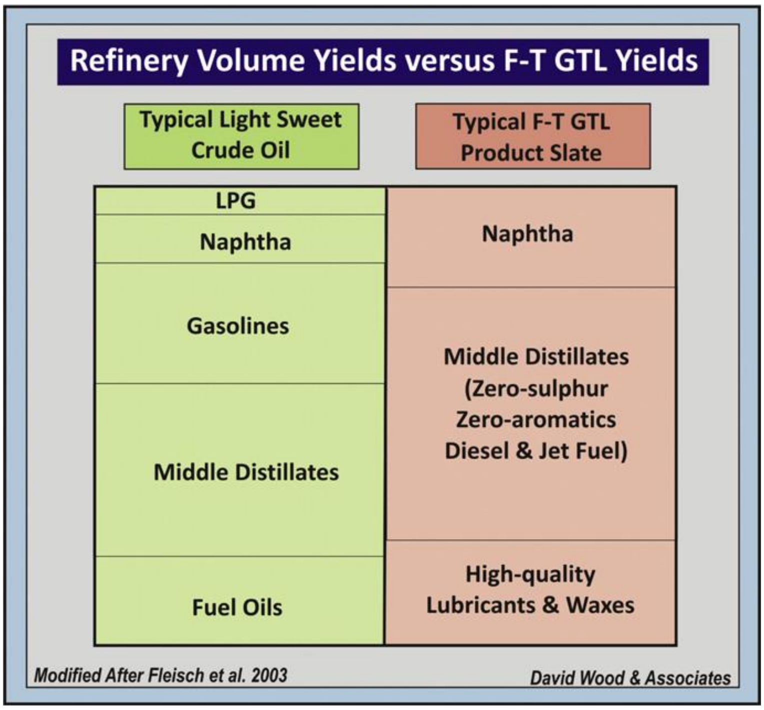
Refinery Volume Yields versus F-T GTL Yields
Typical Light Sweet Crude Oil
Typical F-T GTL Product Slate
LPG
Naphtha
Gasolines
Middle Distillates
Fuel Oils
Naphtha
Middle Distillates (Zero-sulphur Zero-aromatics Diesel & Jet Fuel)
High-quality Lubricants & Waxes
Modified After Fleisch et al. 2003
David Wood & Associates

Figure 1.2 - Refinery volume yields versus FT GTL yields [7]

From Figure 1.2 the FT GTL technology produces more high value, sulphur free products, especially middle distillates, while the traditional crude oil refineries produce substantial quantities of low-value fuel oil, i.e. more than requested by the market. A FT GTL plant with existing technology provides a yield in middle distillates (diesel and kerosene) which is nearly a third more than that from a traditional crude oil refinery [14].

As predicted more than a decade ago [15], diesel demand is globally growing at a 3% rate for year, faster than other refinery products. Against this growth, refiners have significant difficulties to meet diesel demand and quality in the future as crude oil becomes heavier and sourer [16].

To be commercially competitive at oil prices of less than 40 $/barrel, FT GTL plant capital, operating and feed gas costs have to be substantially lower on a unit basis than large-scale plants built in recent years have been able to deliver. Given a FT GTL plant with a unit capital cost close to 100.000 $/barrel/day, operating costs close to 20 $/barrel of product and feed gas costs in the vicinity of 5.00 $/MMBtu, the liquid products would cost approximately 100 $/barrel, an uninviting price in today's market. For this reason, companies have to achieve lower plant and feed gas costs to make FT process economically attractive.

1.4 Fischer-Tropsch Thermodynamics

In order to better understand the FTS process, various aspects of the FT reaction will be now discussed in this and the following sections. The main reactions involved in FTS are the following [17, 18]:

Irreversible reactions

- Synthesis reaction between hydrogen and carbon monoxide to form paraffins:

$$\begin{aligned} & nCO+\left(1+2n\right)H_2 \longrightarrow C_nH_{(2n+2)}+nH_2O \\ & \Delta H_r \cong -39.4 \quad kcal/mol \end{aligned} \tag{1.6}$$

- Synthesis reaction between hydrogen and carbon monoxide to form olefins:

$$\begin{aligned} & nCO+2nH_2 \longrightarrow C_nH_{2n}+nH_2O \\ & \Delta H_r \cong -35.6 \quad kcal/mol \end{aligned} \tag{1.7}$$

$$\begin{aligned} & 2nCO+nH_2 \longrightarrow C_nH_{2n}+nCO_2 \\ & \Delta H_r \cong -49 \quad kcal/mol \end{aligned} \tag{1.8}$$

- Synthesis reaction between hydrogen and carbon monoxide to form alcohols:

$$\begin{aligned} & nCO+2nH_2 \longrightarrow C_nH_{(2n+1)}OH+\left(n-1\right)H_2O \\ & \Delta H_r \cong -7.6 \quad kcal/mol \end{aligned} \tag{1.9}$$

Equilibrium reactions

- Water-gas shift reaction:

$$\begin{aligned}&CO+H_2O\longleftrightarrow CO_2+H_2\\&\Delta H_r\cong -9.9\quad kcal/mol\end{aligned}\tag{1.10}$$

- Methanation reaction:

$$\begin{aligned}&CO+3H_2\longleftrightarrow CH_4+H_2O\\&\Delta H_r\cong -49.2\quad kcal/mol\end{aligned}\tag{1.11}$$

- Carbon deposition:

$$\begin{aligned}&CO+H_2\longleftrightarrow C+H_2O\\&\Delta H_r\cong -32\quad kcal/mol\end{aligned}\tag{1.12}$$

- Boudouard equilibrium:

$$\begin{aligned}&2CO\longleftrightarrow C+CO_2\\&\Delta H_r\cong -42\quad kcal/mol\end{aligned}\tag{1.13}$$

The whole reaction set gives an overall energetic contribution strongly exothermic (about 150 kJ/mol of CO reacted). FTS is a complex system with different reactions: the irreversible Fischer-Tropsch reactions produce hydrocarbons while the equilibrium reactions between CO, CO_2, CH_4 and C, like the WGS reaction or the Boudouard equilibrium, are also present. In any case, the FTS process can be simplified as a combination of the FT reactions and the WGS reaction [19]. According to this hypothesis, hydrocarbons are primary products of FT reaction and CO_2 can only be produced by WGS reaction, a reversible reaction with respect to CO.

The formation of hydrocarbons at the operating conditions of FTS is thermodynamically favourable. Synthetized hydrocarbons and alcohols vary their standard Gibbs free energies of formation as a function of temperature:

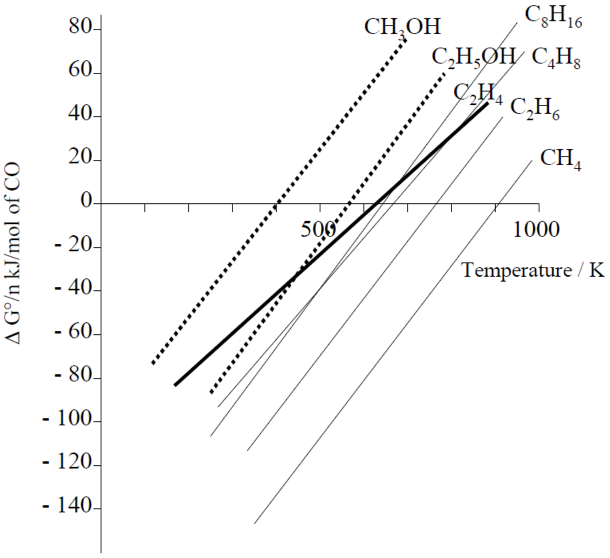

Figure 1.3 - Standard Gibbs free energy of formation of some FTS products [20]

In Figure 1.3 it can be seen how the formation of methane is highly favoured over the other hydrocarbons with increasing molecular weight. To show all the curves on the same scale in the diagram, the free energy changes have been divided by the number of carbon atoms in the product. Many different molecules can be produced up to 400°C and some up to 500°C, particularly at elevated pressures, including acetaldehyde and higher aldehydes, ketones, esters. A broad spectrum of molecules with different carbon numbers and carbon-chains structures is produced, and their distribution depends on the selectivity of the catalyst employed.

1.5 Fischer-Tropsch reaction mechanism

FTS follows the polymerization mechanism according to [21]. It is generally proposed that CO undergoes dissociative or hydrogen-assisted dissociative adsorption on the surface of Ru, Co or Fe metal forming CH_x (x = 0-3) intermediates as the monomers for the polymerization. The chain growth caused by the combination of CH_x monomers leads to the formation of C_nH_m intermediates with different carbon numbers. These intermediates can then undergo hydrogenation to give paraffins as final product, or dehydrogenation to provide olefins. The coupling between methylene (CH_2) groups is mainly accounted for the chain growth but, depending on the type and structure of the surface, other CH_x monomeric species could be also involved in the polymerization. The calculation of energy barrier indeed suggests that the couplings of CH+CH, C+CH, $C+CH_2$ or CH_x+HCO may all be possible [22-27].

Many researches have been carried out to identify the surface species involved in the chain initiation and growth, but the mechanism of the FT reaction is still under debate.

The carbide theory by Fischer in 1926 was the first mechanism proposed but it had a problem, it didn't explain the relatively large production of oxygenated products, i.e. alcohols.

Elementary steps of FTS can be grouped into few basic steps [28]:

1. Reactant (H_2 and CO) adsorption
2. CO activation (or chain initiation)
3. Chain propagation
4. Chain termination (product formation)

Figure 1.4 displays the possible activation steps in the carbide (also reported as alkyl or methylene) and the CO insertion mechanisms. In the traditional carbide pathway, the CO activation step consists of a direct CO dissociation, meaning that the C-O bond is severed before C is hydrogenated. Instead in the CO insertion mechanism the CO molecule is first hydrogenated and only then the C-O bond is broken to give the chain starter (CH_3S). A new change to the carbide mechanism also assumes that the C-O bond scission is hydrogen assisted.

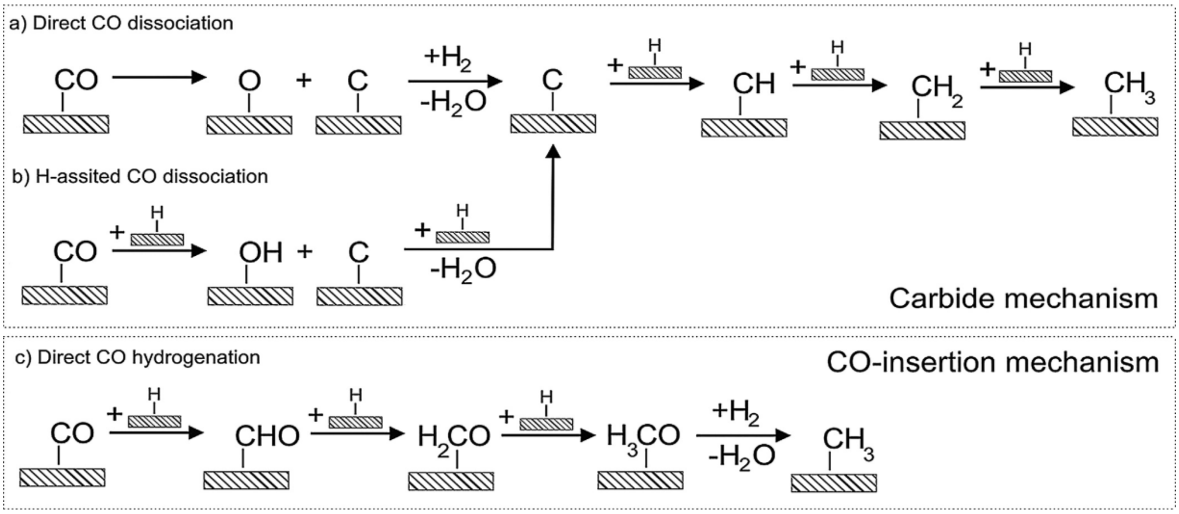
a) Direct CO dissociation
CO
O
C
+H2
-H2O
H
CH
CH2
CH3
b) H-assited CO dissociation
OH
Carbide mechanism
c) Direct CO hydrogenation
CO-insertion mechanism
CHO
H2CO
H3CO

Figure 1.4 - Examples of CO activation pathways: (a) direct CO dissociation (carbide mechanism) and (b) H-assisted CO dissociation (carbide mechanism); (c) CO hydrogenation (CO-insertion mechanism) [28]

The main difference between the two pathways is the type of molecule inserted into the growing chain: CH_x for the carbide (most often CH_2) and absorbed CO for the CO insertion mechanism. A comparative study of the two mechanisms by Storsæter et al. [29] showed that the CO insertion pathway had a lower activation barrier compared to both direct and hydrogen assisted mechanisms. Based on these observations, it was suggested that the CO insertion mechanism was likely the prevailing mechanism of FTS.

Figure 1.5 shows a simplified scheme for the chain initiation, growth and termination of the FT reaction. The CH_3 groups are assumed to act as chain growth centres: the addition of a hydrogen atom produces methane while the insertion of a CH_2 group into the metal-carbon bond of a CH_3 group gives an ethyl group; the continuation of this type of process provides a wide spectrum of adsorbed alkyl groups [30].

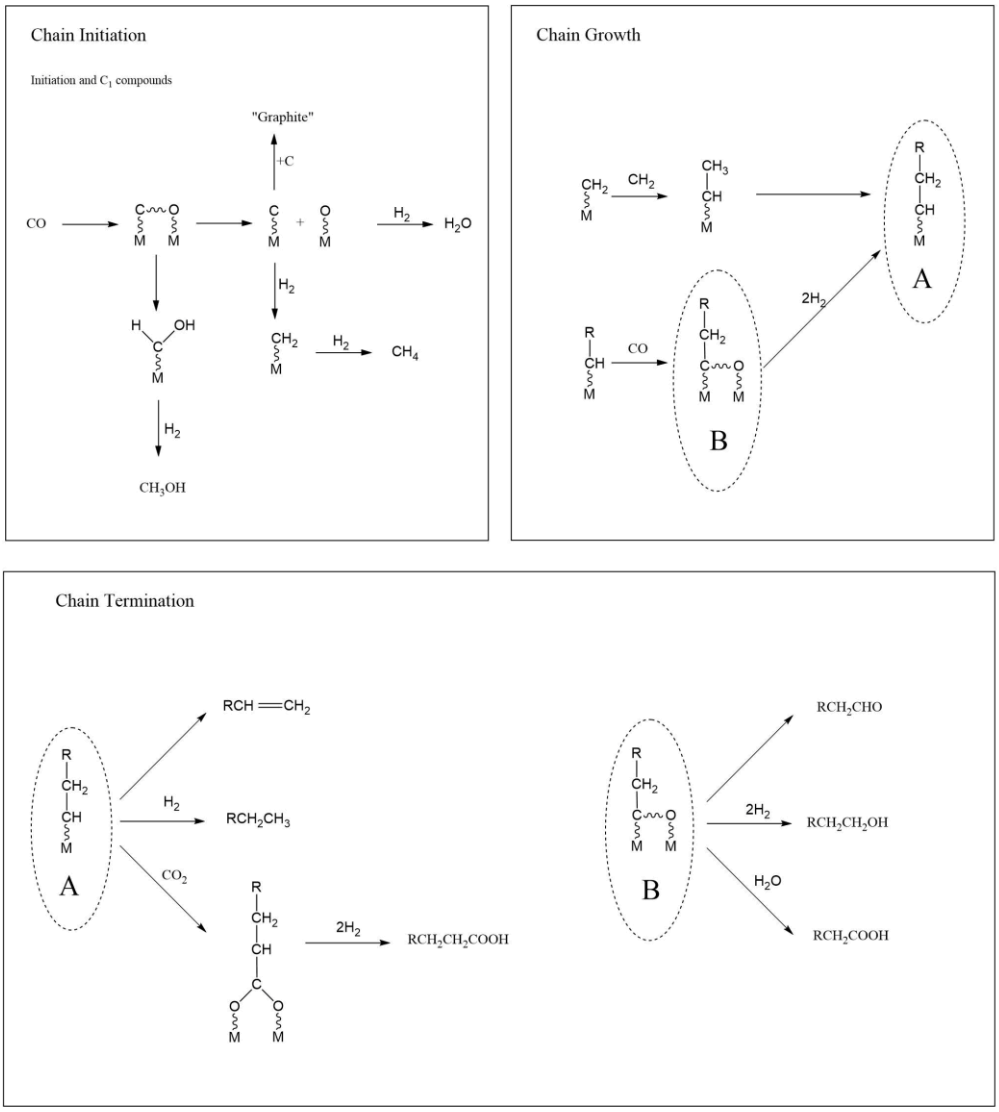
Chain Initiation
Initiation and C₁ compounds
"Graphite"
+C
CO
H₂
H₂O
CH₄
CH₃OH
Chain Growth
CH₂
CO
2H₂
A
B
Chain Termination
RCH=CH₂
RCH₂CH₃
CO₂
2H₂
RCH₂CH₂COOH
RCH₂CHO
RCH₂CH₂OH
H₂O
RCH₂COOH

Figure 1.5 - Different steps of the FTS reaction mechanism

The oxygen released during the CO dissociation is removed from the catalyst as either H_2O or CO_2. Regarding the hydrogenation process, there are still debates about the reaction mechanism, i.e. if the monomer formation proceeds via hydrogenation of dissociated or undissociated CO.

The nature of primary FT products reflects the type of intermediates from which they originate. Hydrocarbon FT products are preferentially straight chain olefins or paraffins. The typical paraffin formation is represented in Figure 1.6 as:

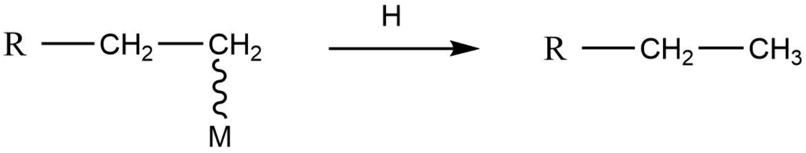

Figure 1.6 - Paraffin formation step

Terminally bonded (alpha) alkyl species on the catalyst can be considered the most common intermediates. Instead olefin formation is given by the dissociative desorption of the alkyl species (β-elimination), as shown in Figure 1.7:

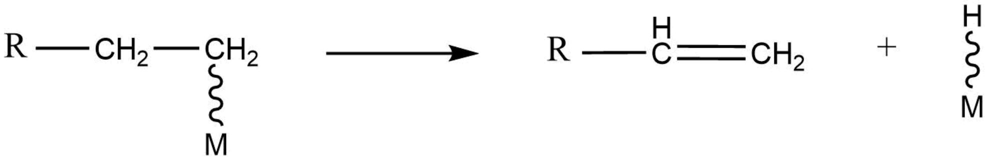

Figure 1.7 - Olefin formation step

The probability ratio of primary desorption as a paraffin over olefin is usually 0.25, meaning that the reactions of desorption as a paraffin is less probable of the reaction of desorption as an olefin. The chain propagation is favoured against chain termination because of the "selective inhibition" principle, i.e. termination reactions are more inhibited by steric hindrance than propagation.

This effect is more pronounced with paraffin than olefin formation: while paraffin desorption, being between alkyl and hydrogen, requires two metal sites, olefin desorption needs only the intermediate, i.e. the transition state with π and σ bonding at the same metal site. Chain termination can also occur by CO insertion into surface alkyls, leading to the formation of predominantly primary alcohols [30].

1.6 FT product selectivity

The hydrocarbon products synthesized through the FT process on Co, Fe and Ru generally show the following properties [19]:

- The hydrocarbon distribution by carbon number gives the highest concentration for C_1 and then decreases monotonically for higher carbon numbers, although around C_3-C_4 a local maximum is often observed.
- Monomethyl hydrocarbons are present in moderate quantities, while dimethyl products are present in significantly smaller amounts than monomethyl. None of these branched hydrocarbons contains quaternary carbon atoms.
- Olefins from iron catalysts stand for more than 50% of the hydrocarbon products at low carbon number, more than 60% being α-olefins. The ethylene selectivity is low compared to propylene. The olefin content decreases asymptotically to zero with increasing carbon number.
- A change in chain growth probability can be observed for linear paraffins, but not for olefins.
- Yield of alcohols is maximum at C_2 and decreases with carbon number. The low yield of methanol is probably due to the thermodynamic limitations.

Several authors investigated the carbon number spectrum based on the assumption of a stepwise chain mechanism. Anderson studied the spectrum of many different catalysts and noticed that the plot of $\ln\left(w_n/n\right)$ against carbon number gave an almost straight line over a large carbon number range (where w_n is the mass fraction and n the carbon number). This indicated that the probability of chain growth was fairly constant [12].

Schulz modified and applied to the FT hydrocarbon spectrum the Flory equation dealing with the product distribution in a polymerization process. This new theory was referred as the Anderson-Schulz-Flory (ASF) equation, used to model the distribution of hydrocarbons obtained in the FT process.

1.6.1 Anderson-Schulz-Flory equation

The parameter α is defined as the chain growth probability, which is the probability that a molecule will continue reacting to form a longer chain:

$$\alpha = \frac{r_{propagation}}{r_{propagation} + r_{\mathrm{termination}}} \tag{1.14}$$

where $r_{propagation}$ is the chain growth reaction rate and $r_{\mathrm{termination}}$ is the desorption rate of the adsorbed chains.

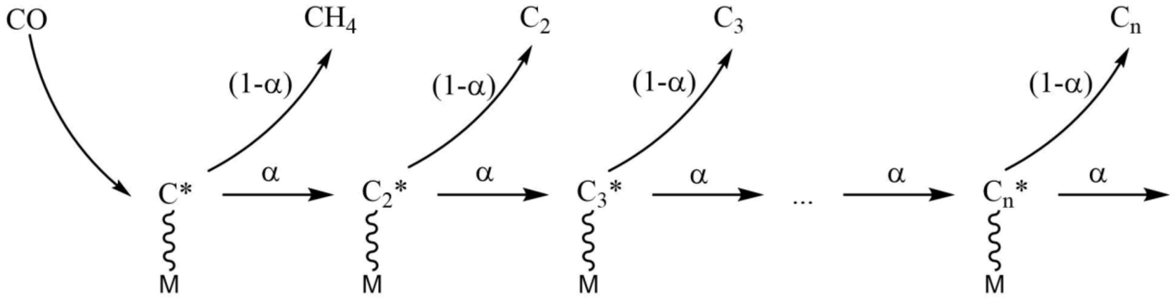

Figure 1.8 - Anderson-Schulz-Flory mechanism

As can be seen from Figure 1.8, the probability of producing a molecule with n carbon atoms is:

$$p_n = (1-\alpha)\alpha^{n-1} \tag{1.15}$$

which is also equal to the instantaneous molar fractions produced x_n. The instantaneous distribution of mass fraction will be then calculated from:

$$w_n = A \cdot n \cdot x_n \tag{1.16}$$

where A is a constant obtainable setting to one the sum of all mass fractions:

$$\sum_{n=1}^{\infty} w_n = 1 \tag{1.17}$$

Solving this equation and substituting the value of A in the previous expression of w_n will provide:

$$w_n = n(1-\alpha)^2 \alpha^{n-1} \tag{1.18}$$

It is assumed that the growth factor α is independent of chain length; it can be estimated by a linear least square regression of the previous equation in logarithmic form:

$$\ln(w_n/n) = \ln\left((1-\alpha)^2\right) + (n-1)\ln(\alpha) \tag{1.19}$$

Plotting $\ln(w_n/n)$ against the carbon number, the value of α is derived from the slope of the drawn line.

Many factors influence the value of α, such as process conditions, type of catalyst and chemical promoters [31, 32]. Figure 1.9 and Figure 1.10 depict the ASF product distribution as a function of α, showing how the average carbon number of the products increases with higher values of the growth factor.

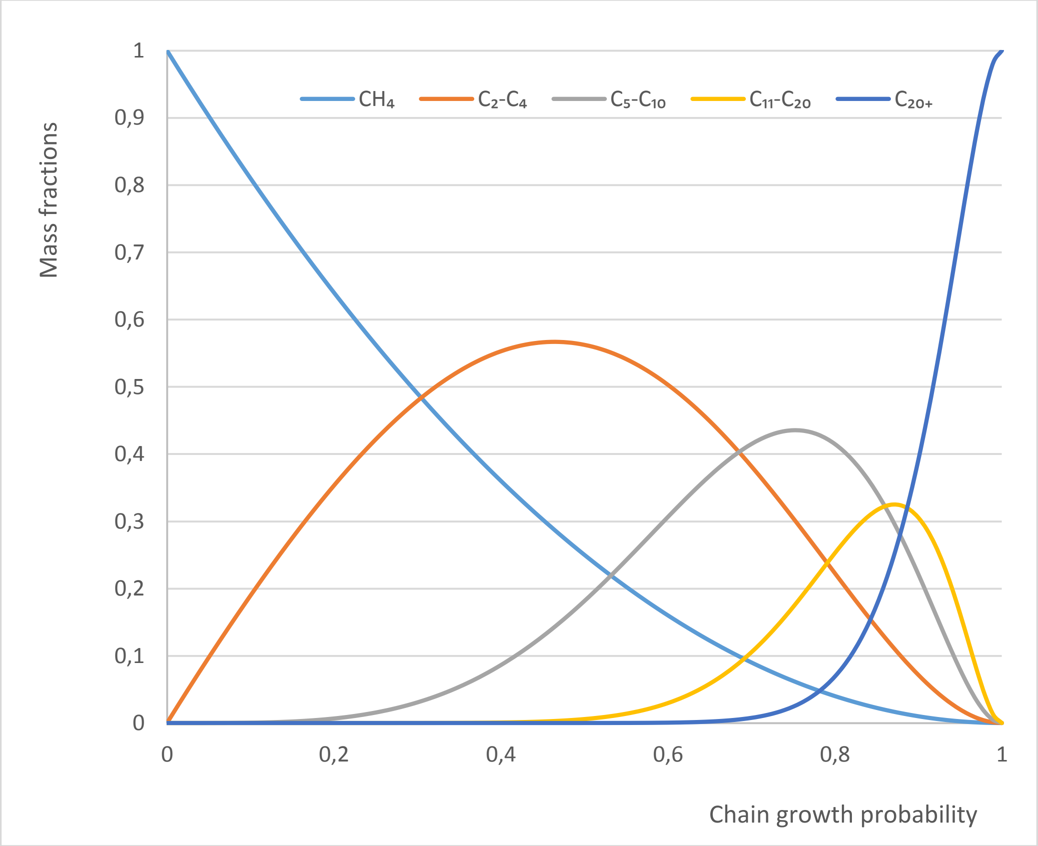

Figure 1.9 - Mass fractions on chain growth probability

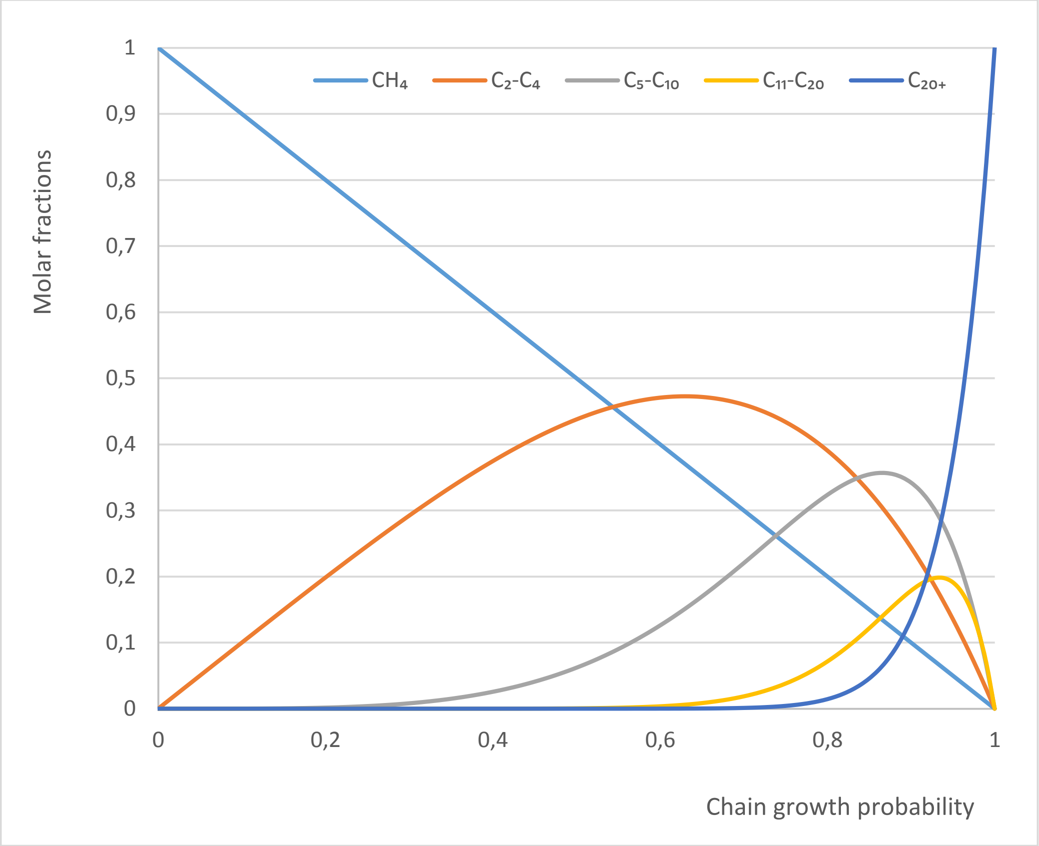

Figure 1.10 - Molar fractions on chain growth probability

The ASF model does not differentiate between different product types, while in reality a multicomponent mixture is formed. According to the ASF equation, the selectivity to C_2-C_4 olefins is maximum with an α value between 0.4 and 0.5. it's possible to shift product selectivity to low α values by increasing the process temperature. Anyway this decrease in chain growth also involves an increase in selectivity to methane as shown in Figure 1.9 and Figure 1.10. This effect has long been one of the major restrictions for the industrial application of the direct conversion of syngas into lower olefins through FTS [33, 34].

The ASF distribution is a well-accepted model for describing selectivity of the FT products, but it also has some flaws. Significant deviations have been reported in literature:

- Methane selectivity is usually higher than theoretically predicted from the ASF equation. Several mechanisms have been formulated to justify this deviation [35, 36].

- Both ethane and ethylene selectivity in practice is lower than predicted by the ASF model. This is commonly observed on iron, cobalt and ruthenium catalysts, where C_2 selectivity is lower than both the C_1 and C_3 selectivity [19].
- In the ASF model α is considered a parameter independent of the product carbon number n; nevertheless, it has been observed that, at a carbon number of about 10, the slope of $\ln\left(w_n/n\right)$ against carbon number increases. This phenomenon has been observed on iron, cobalt and ruthenium catalysts [37].

  Studies have suggested that the increase of growth probability, or the presence of two probabilities of growth, may be caused by the occurrence of different catalytic sites or different reactions of chain termination. The assumption of multiple catalytic sites anyhow cannot explain the decrease of the olefin to paraffin ratio with increasing chain length, decreasing space velocity and increasing H_2/CO ratio in the reactor. It has been stated that the existence of secondary reactions gives the most satisfying explanation for the deviations from the ASF distribution.

1.7 FT catalysts

The type of catalyst is an important factor to consider for the FT process since not many metals show catalytic activity in the FTS [38]. The reaction, as explained before, is assumed to start with the adsorption of CO on the catalyst surface where it reacts with absorbed hydrogen to form a methylene group, which is responsible for the C-C coupling of the chain growth. Probably, there are at least two reactions paths which coexist in the initial step of the FT process: one with CO adsorbed in a dissociative way (i.e. the C-O bond is broken before any possible reaction with hydrogen) and another where some hydrogenation by the adsorbed hydrogen precedes the C-O cleavage [39]. A good FT catalyst should then adsorb both CO, possibly in a dissociative way, and H_2.

Moreover, the formation of metal oxides is possible during the FT process either by dissociative CO absorption or by metal reaction with the produced water; these metal oxides have to be easily reduced under reaction conditions. For this reason, most early transition metals are not good FT catalysts because, despite their capability to adsorb CO, they form stable oxides which cannot be reduced under FT conditions. Iridium, platinum and palladium adsorb CO in a non-dissociative way, while metals of groups 11 and 12 hardly adsorb it: none of them is an effective catalyst for the FTS. The specific activities (i.e. the reaction rates per unit surface area of metal) of the metals of the former Group VIII (all but osmium) were tested under comparable conditions, with ruthenium being the most active catalyst.

Nickel (and, to even a larger extent palladium) showed high selectivity towards methane formation, an unwanted feature for a FT catalyst [39]. Osmium was also evaluated, but turned out to be ca. 100 times less active than ruthenium. The best FT catalysts are then based on iron, cobalt and ruthenium, while nickel, rhodium and osmium (and possibly rhenium) are only moderately active [40]. All these concepts have been summarized in Figure 1.11.

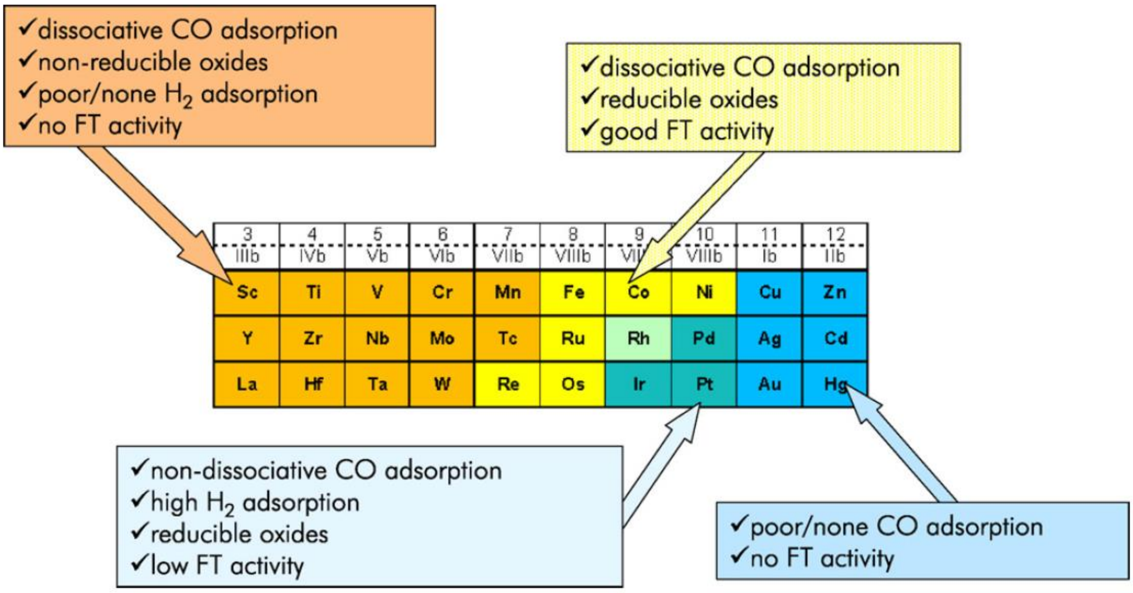
✓dissociative CO adsorption
✓non-reducible oxides
✓poor/none H_2 adsorption
✓no FT activity
✓dissociative CO adsorption
✓reducible oxides
✓good FT activity
3 IIIb
4 IVb
5 Vb
6 VIb
7 VIIb
8 VIIIb
9 VIIIb
10 VIIIb
11 Ib
12 IIb
Sc
Ti
V
Cr
Mn
Fe
Co
Ni
Cu
Zn
Y
Zr
Nb
Mo
Tc
Ru
Rh
Pd
Ag
Cd
La
Hf
Ta
W
Re
Os
Ir
Pt
Au
Hg
✓non-dissociative CO adsorption
✓high H_2 adsorption
✓reducible oxides
✓low FT activity
✓poor/none CO adsorption
✓no FT activity

Figure 1.11 - Catalytic activity of transition metals in the Fischer-Tropsch reaction [40].

However, huge amounts of catalyst are required for FT industrial purposes and ruthenium is too rare and expensive to be considered on this scale. Ultimately only iron and cobalt are the metals suitable for FT industrial applications. Iron is obviously cheaper than cobalt but also the carbon feedstock has to be considered. Iron is a good catalyst of the water-gas shift reaction and therefore is particularly suitable for hydrogen-poor syngas, like those obtained from biomasses or coal gasification. Cobalt instead performs better with an almost stoichiometric ratio of hydrogen to carbon monoxide, so it is preferred when the carbon feedstock is natural gas [38].

Except for methane, which usually forms in amounts higher than expected, the FT product distribution follows the Anderson-Schulz-Flory model pretty well [39]. The FT output is a complex mixture of products, ranging from methane to high molecular weight waxes. The correct choice of catalyst and reaction conditions allows tuning the composition of the final mixture, but it is nevertheless impossible to produce selectively a well-defined range of products, i.e. middle distillates. So, the best way to maximize diesel production is to select the conditions which greatly favour the formation of long chain linear paraffins, that can be then fed to a hydrocracking stage to be transformed into valuable fuel.

Cobalt and iron are the first metals which were proposed by Fischer and Tropsch as catalysts for syngas conversion; at industrial level both have been used for FTS. A brief comparison of the iron and cobalt catalysts [41] is shown in Table 1.1. Cobalt catalyst are more expensive, but they are more resistant to deactivation. Even if the activity of the two metals is comparable at low conversions, the productivity at higher conversion is more significant with cobalt catalysts. Water generated by the FTS slows the reaction rate on iron to a greater extent than on cobalt. At relatively low temperatures of 200-250°C chain growth probabilities of about 0.94 have been reported [5] for cobalt-based catalysts and about 0.95 for iron catalysts. The water-gas shift reaction is more significant on iron than on cobalt catalysts.

Table 1.1 - Comparison of cobalt and iron catalysts [41]

Parameter	**Cobalt catalyst**	**Iron catalyst**
Cost	More expensive	Less expensive
Lifetime	Resistant to deactivation	Less resistant to deactivation (coking, carbon deposit, iron carbide)
Activity at low conversions	Comparable	
Productivity at high conversion	Higher; less significant effect of water on the rate of CO conversion	Lower; strong negative effect of water on the rate of CO conversion
Maximal chain growth probability	0.94	0.95
Water-gas shift reaction	Not very significant, more noticeable at high conversions	Significant
Maximal sulphur content	<0.1 ppm	<0.2 ppm
Flexibility (temperature and pressure)	Less flexible; significant influence of temperature and pressure on hydrocarbon selectivity	Flexible; methane selectivity is relatively low even at 613K
H_2/CO ratio	≈2	0.5-2.5
Attrition resistance	Good	Not very resistant

Iron catalysts usually produce more olefins. Both catalysts are very sensitive to sulphur, which can poison them: the fed syngas for iron-based catalysts should not contain more than 0.2 ppm of sulphur, while for cobalt-based catalysts it should contain much less than 0.1 ppm of sulphur. Cobalt catalysts supported on oxide are generally more resistant to attrition than iron co-precipitated counterparts and for this reason they are more suitable for use in slurry reactors.

Iron catalysts produce a mixture of hydrocarbons and oxygenated compounds under different pressures, H_2/CO ratios and temperatures (up to 340°C). Cobalt catalysts operate at a very specific range of temperatures and pressures; an increase in temperature leads to a great increase in methane selectivity. Iron catalysts seem to be more appropriate than cobalt systems for conversion of biomass-derived syngas since they can work at lower H_2/CO ratios [41].

1.7.1 Iron FT catalysts

Iron catalysts can be used to pursue two different directions for product selectivity. The first one aims to produce a low molecular weight olefinic hydrocarbon mixture in an entrained phase or fluid bed process (Sasol Synthol process). Given the relatively high temperature necessary for this process (340°C), the average molecular weight is so low that no liquid phase occurs under reaction conditions. The catalyst particles moving in the reactor are small (between 0.3 and 0.6 µm [42]) and carbon deposition on the iron surface does not disturb reaction operation. For this reason, the use of low porosity catalysts with small pore diameters is appropriate. To maximise the overall gasoline yield, the C_3 and C_4 olefins have been oligomerized at Sasol. However, nowadays the recovering the olefins for use as chemicals (e.g. polymerisation processes) is more advantageous [42].

The second direction of iron catalyst development, the same pursued by this thesis, aims at the highest catalyst activity obtainable at low temperatures, where most of the hydrocarbon products are in the liquid phase. Such catalysts are usually obtained through precipitation from nitrate solutions. A high content of catalyst support provides mechanical strength and the wide pores needed for an easy mass transfer of the reactants in the liquid product filling the pores. The main product of this process is a paraffin wax, that can be refined to marketable wax or can also be selectively hydrocracked to a high quality diesel fuel.

As has been noted, iron catalysts are very flexible. Selective FT synthesis of linear α-olefins seems only possible with iron catalysts. Iron FT catalysts also exhibit water-gas shift activity (in contrast to cobalt catalysts). This is a desirable feature for FT synthesis with CO-rich syngas, as obtained from coal and biomass gasification ($H_2/CO = 1$). The activity of iron catalysts is inhibited by the water produced in the FTS [43], thus restricting the maximum degree of conversion. In order to fix this problem a gas recycle can be added at the FT reactor outlet stream, after the removal of the water and organic condensate produced.

1.8 FT plants overview

The potential market for coal and natural gas (otherwise not “recoverable”) together with the awareness of an inevitable rise in oil prices have pushed many companies towards the FT industrial process. Here follows an overview of the main companies that have built, or propose to realize, plants producing liquid fuels through the FTS, using different catalysts, reactors and operative conditions [44].

- **SASOL**: The political reasons previously mentioned have prompted South Africa, through Sasol, to develop a FT industrial process using coal as raw material, widely available throughout the country. Sasol began its production of liquid fuels in Sasolburg (Sasol I, 1955) using two different technologies: a fixed bed (ARGE) process as well as a circulating fluidized bed (Synthol) process. The former process is characterised by a low reaction temperature around 250°C (LTFT), while the latter works at higher temperatures, around 350°C (HTFT). The ARGE fixed bed reactor produces diesel and heavy paraffins, while the Synthol circulating bed reactor gives gasoline and olefins. In the 80’s Sasol built Sasol II and Sasol III plants in Secunda with their second generation FT technologies: the Synthol advanced process (HTFT) and liquid phase process (LTFT). Overall today Sasol produces about 150,000 barrels/day of liquid fuel, plus a range of chemical products, all derived from the gasification of coal.
- **SHELL**: Shell has built in 1993 in Bintulu (Malaysia) a natural gas synthesis plant, able to convert 100 million ft^3/day of natural gas into 12,500 barrels/day. The investment made at the time amounted to approximately $530 million. The Shell process (Shell Middle Distillate Synthesis, SMDS) produces heavy paraffins, which are subsequently fed to a hydrocracking unit to obtain middle distillates and special-use products (additives for detergent, additives for solvents and various waxes). The plant was stopped in ’97 for the explosion of an air separation unit, and then restarted in 2000. In October 2003 Shell signed a pre-agreement with Qatar for the construction of a $19 billion GTL plant (Pearl GTL) capable of treating the natural gas extracted from the deposits in the northern region of the country. With full ramp-up achieved towards

the end of 2012, Pearl GTL is now capable of producing 140,000 barrels of GTL products each day. The plant also produces 120,000 barrels/day of natural gas liquids and ethane.

- **MOBIL**: Mobil (now ExxonMobil) has used a different route to get liquid fuels from natural gas. The process, developed in the 80s by Mobil, produces gasoline passing through an intermediate stage where methanol is obtained. This MTG (Methanol to Gasoline) process was employed in a plant in New Zealand in 1986, where a charge of 130 million ft^3 of natural gas is daily converted into 14,500 barrels of gasoline. The plant at the end of the 90s was converted to the production of chemical grade methanol, obtained by the distillation of the crude methanol.
- **EXXONMOBIL**: ExxonMobil has developed a technology named AGC-21 (Advanced Gas Conversion Technology 21st century). The industrial process, covered by many U.S. and international patents, converts the synthesis gas into heavy hydrocarbons with a cobalt catalysts and a fluid bed reactor of their own design. The product synthetized, consisting principally of linear paraffins with a high boiling point (approximately 340°C), is sent to a subsequent finishing step to obtain the desired cuts. ExxonMobil has also built in 1996 a pilot plant in Baton Rouge (Louisiana, USA) with a capacity of 200 barrels/day and, in July 2004, signed an agreement with Qatar to build a GTL plant with a production capacity of 154,000 barrels/day by using the AGC-21 technology.
- **SYNTROLEUM**: Syntroleum was founded in 1984 and from the beginning became interested in the FT process, with the objective to reduce the investment costs of the GTL plants. Following this logic Syntroleum developed its own technology for the production of syngas, where most of the investment costs of a GTL plant are located, using air rather than oxygen and consequently avoiding the need of an expensive air separation unit. Syntroleum built in 1990 a first pilot plant with a production of 2 barrels/day, where they tested various types of catalysts and even a reactor of their own design. In 1999 Syntroleum started a pilot plant with a capacity of 70 barrels/day at the BP refinery (formerly ARCO) in Cherry Point (Washington). A plant of the same capacity, able to convert 1 million ft^3/day was constructed in early 2004 in Tulsa (Oklahoma USA).

- **BP**: BP has been working on GTL technology since the 80s by developing in 1985 a cobalt-based catalyst, whose performance has been significantly improved in the following years. In the second half of the 90s BP began a collaboration with Davy Process Technology (DPT), which had developed its own technology for the production of syngas. In 2000 BP began the construction of a pilot plant in Nikiski (Alaska) using DPT technology for the production of syngas and using proprietary technology (cobalt catalyst and a fixed bed reactor) in the synthesis section. The investment cost of the plant amounted to \$86 million and it is able to convert 3 million ft^3/day into 300 barrels/day of fuel.
- **ENI-IFP**: EniTecnologie and IFP (Institute Français du Pétrole) have realized, at the Agip refinery in Sannazzaro de’ Burgondi (Pavia), a pilot plant with a capacity of 20 barrels/day. The plant required an investment of 16 million € and became operational in November 2001.

2 Laboratory reactor equipment and results

The first objective of this thesis work has been the development of a kinetic model based on the experimental data provided by the Università degli Studi di Milano from their laboratory FT plant.

The experimental results were obtained performing multiple runs at different temperatures and H_2/CO ratios, thus allowing the kinetic model discrimination that will be discussed in chapter 3.

This chapter will focus instead on the description of the laboratory equipment and catalyst used during the experimental runs, reporting the collected test results.

2.1 High loading Fe-supported FT catalysts

The iron catalyst selected for the experimental runs has been extensively studied in various works by Pirola et al. [45, 46]. In these papers many properties of the high loading Fe-silica supported catalyst have been evaluated and optimized, like its composition, preparation, activation and mechanical resistance. All these analyses showed that the best catalyst to perform a series of experimental runs was the one loaded with $Fe_{30}K_{2.0}Cu_{3.75}$ (where the percentages concerning the composition are on a weight basis):

- It had a good CO conversion and yield to C_{2+}, second only to the Fe_{50} loaded catalyst (catalysts with an iron load >50% do not really support all the active metal on silica).

- It did not present any problem during the mechanical resistance evaluation, while the Fe_{50} loaded catalyst showed some abrasion phenomena with loss of iron from silica particles.

The tested iron-based catalysts were prepared according to the traditional impregnation method, as described in [45], starting from an aqueous solution of precursor and subsequently adding the support (silica). The reagents used for the samples preparation are reported in Table 2.1.

Table 2.1 - List of reagents used in the catalyst preparation

	Reagent	**Technical Data**		
		Company	**Molecular weight**	**Purity**
Support	SiO_2	Fluka	60.086 g/mol	>99%
Precursors	$Fe(NO_3)_3 \cdot 9H_2O$	Riedel de Hean	403.85 g/mol	98%
	KNO_3	Merk	101.11 g/mol	>99%
	$Cu(CH_3COO)_2 \cdot H_2O$	Fluka	199.65 g/mol	99%
Solvent	Extra pure water			

The methodology for the catalyst preparation consists of several steps, described here:

- Drying, then activation, of the silica support in oven for a night at T=120°C.
- Weight of the calculated amount of iron, potassium and copper precursors.
- In a pyrex vessel (250 ml) the weighted precursors, the water (25 ml) and silica (5 g) are added.
- The vessel is put on a rotavapor (36 rpm, T=40°C, atmospheric pressure) for 24 hours (Figure 2.1).
- The solvent is evaporated from the rotavapor under vacuum and raising the temperature to 60-70°C.
- The powder is dried in oven at T=120°C for a night, to completely evaporate the remaining water.
- Calcination (T=500°C) in a muffle furnace for 4 hours.
- The catalyst is sieved to obtain a powder mesh between 100 and 140.

Figure 2.1 - Rotavapor used for the catalyst preparation

2.2 FT laboratory plant

The experimental tests were carried out in a laboratory plant compromising a tubular reactor (made by "Renato Brignole" Company) with a fixed bed of catalyst placed vertically. The quantities of gas and catalyst that come into play are very small in order to be able to perform a basic research with limited costs and avoid problems related to safety or to the radial and axial thermal gradients within the catalytic bed.

The feed is prepared in situ mixing three flows of pure CO, pure H_2 and pure N_2 using three different flow meters. Then the gases enter from the top side of the catalytic reactor, react with the catalyst/diluent mixture (1 g of fresh catalyst with 1 g of α-Al_2O_3 Fluka used as diluting material) and finally come out from the lower part with the formed products. The plant pipes are heated till the cold trap to avoid the condensation of heavier products. In the cold trap, cooled at 5°C, the heavy hydrocarbons and the water condense, while the light fraction leaves the trap in gaseous state.

The gases and the light hydrocarbons go into a flow meter for their quantification and in an analytical zone where they are analysed by a micro gas chromatograph (Agilent 3000). The liquid condensed in the trap consists of two phases: an aqueous phase (containing water with traces of C_5-C_7 hydrocarbons and oxygenates) and a lighter organic phase (containing hydrocarbons in the C_7-C_{30} range).

In Figure 2.2 the detailed scheme of the FT laboratory plant is reported.

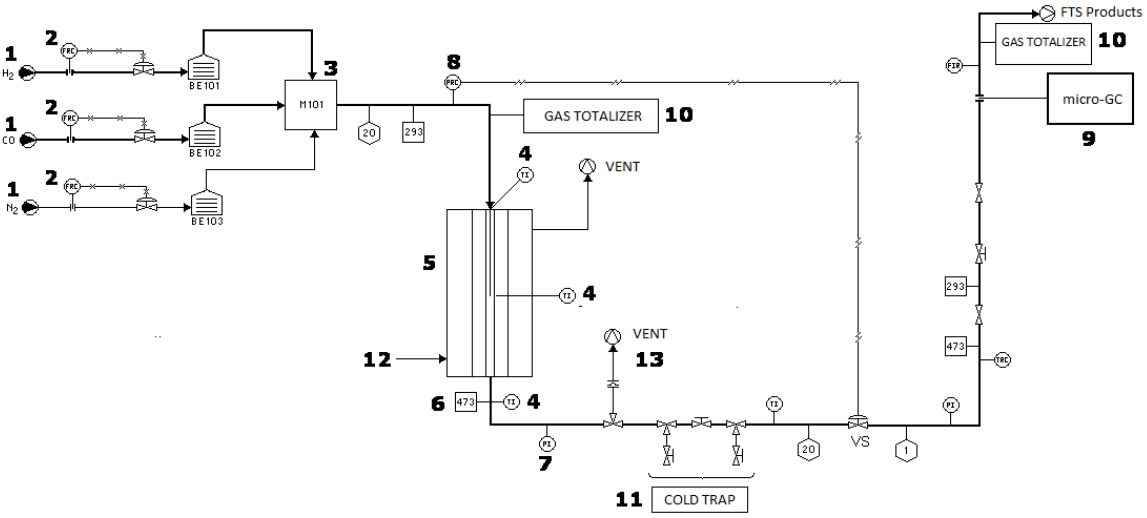
FTS Products
GAS TOTALIZER
10
FIR
micro-GC
9
1
H2
2
FRC
BE101
3
M101
1
CO
2
FRC
BE102
1
N2
2
FRC
BE103
8
PRC
20
293
GAS TOTALIZER
10
4
TI
VENT
5
TI
4
293
473
TRC
VENT
13
12
6
473
TI
4
TI
PI
7
20
VS
1
PI
11
COLD TRAP

Figure 2.2 - Laboratory plant flowsheet [47]

The legend for the laboratory plant flowsheet is the following:

1. Micrometer needle valve.
2. FRC: mass flow meters (Brooks® mod. 5850TR) for hydrogen and carbon monoxide with a maximum measurable flow of 100 Nml/min and for nitrogen with a maximum measurable flow of 20 Nml/min.
3. Gas mixer.
4. TI: thermocouples for the reading of the temperatures of the catalytic bed, of the reactor and of the heated downstream pipe.
5. Fixed-bed tubular reactor made by "Renato Brignole" Company.
6. PSV: rupture disc calibrated to burst at 30 bar.
7. PI: pressure indicator.
8. PRC: micrometer needle valve for pressure control and regulation.
9. Micro gas chromatograph "Agilent 3000".
10. Upstream and downstream gas totalizer.

11. Water-cooled cold trap operating at 5°C and 20 bar.
12. Cooling air for the temperature control of the reactor (about 5 bar).
13. Vent connected to the fume hood.

A photo of the FT laboratory plant is reported in Figure 2.3.

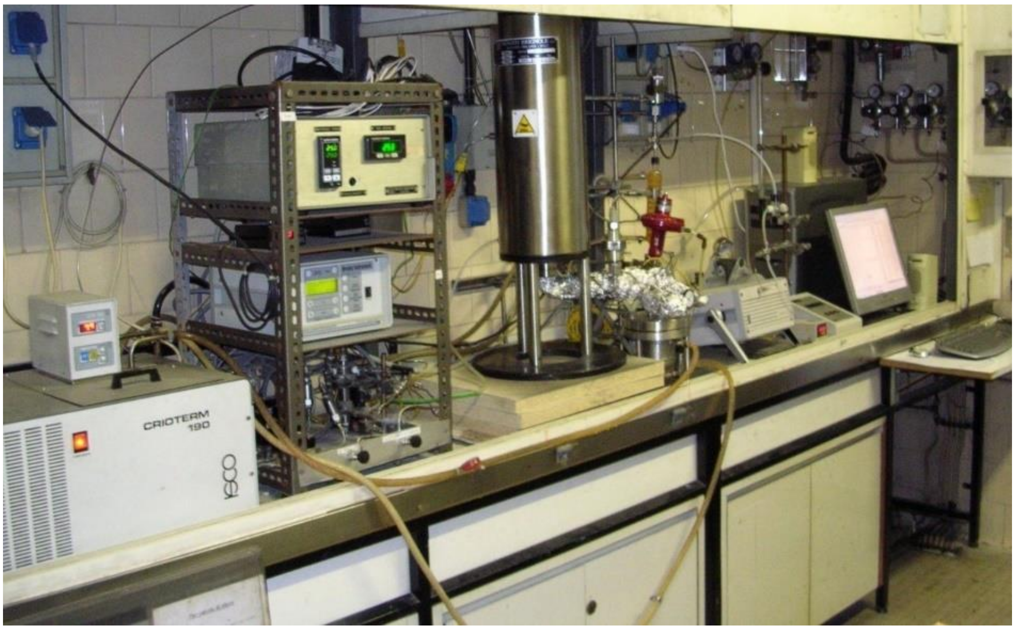

Figure 2.3 - Fischer-Tropsch laboratory equipment

2.3 Experimental procedure

The catalyst, before being loaded in the reactor, undergoes a standard preparation which involves three fundamental steps:

1. Catalyst mesh between 106 and 150 microns, performed to have a uniform catalyst size distribution and so avoid clogging phenomena of the reactor.
2. Drying in oven at T=120°C for a night at least, to obtain a sample as dehydrated as possible.

3. Catalyst dilution with anhydrous α-Al_2O_3 in a 1:1 ratio. The dilution is important to achieve a homogenous flow of the reactants inside the reactor and improve the dispersion of the heat of reaction to avoid the formation of hotspots.

1.8.1 Catalyst loading

The catalyst and the diluent are then carefully loaded in the middle of the reactor, where the isothermal zone is located as seen in Figure 2.4.

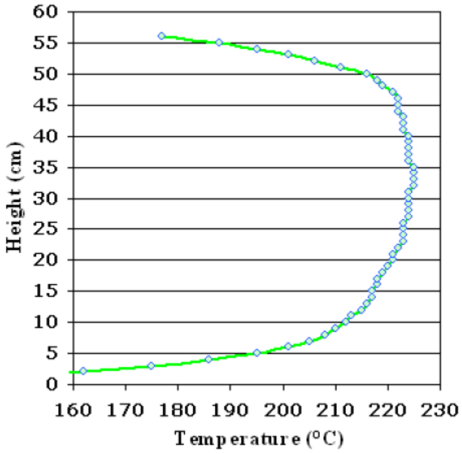

Figure 2.4 - Laboratory reactor thermic profile [47]

The mixture of catalyst and α-Al_2O_3 is approximately 7 cm in height to ensure that all the charged material is placed in the isothermal zone, while the steel pipe diameter is 6 mm. The catalyst is held in place using two layers of quartz wool, thus preventing also the formation of preferential paths for the gas flow. The reactor internal loading arrangement is shown in Figure 2.5.

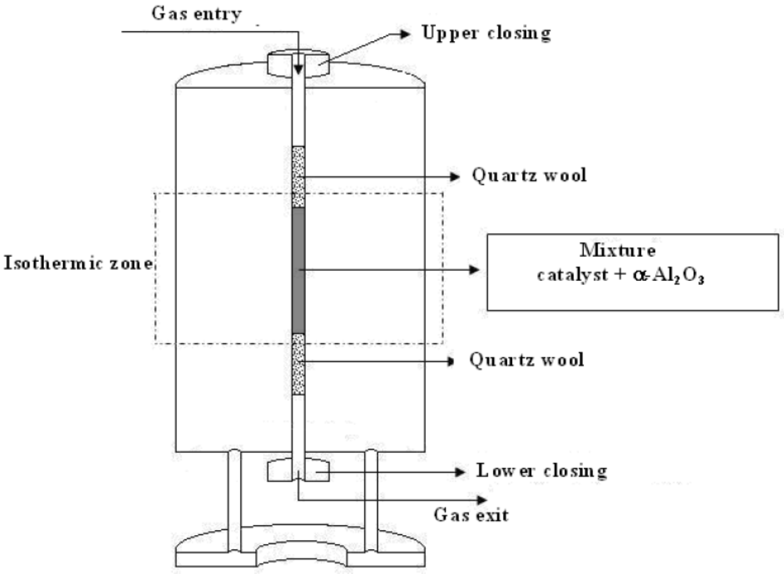
Gas entry
Upper closing
Quartz wool
Isothermic zone
Mixture
catalyst + α-Al₂O₃
Quartz wool
Lower closing
Gas exit

Figure 2.5 - FT reactor internal loading arrangement

1.8.2 Catalyst activation

After the closing the pressure inside the reactor is raised to 4 bar with the activation gases. The gas flow is then stopped and the reactor pressure checked to find possible gas losses. If the reactor pressure remains stable, the catalyst activation step is performed.

The catalyst activation is the process in which the catalyst is reduced from its oxidised state to the reduced or metallic state. In the FT reaction the active form for the iron-based catalysts are the carbide iron forms. The catalyst was charged into the reactor in the oxidised form since the last step in the catalyst preparation is the calcination in air. The catalyst activation/reduction was performed at high temperature (T=350°C) and rather low pressure (P=4 bar) for 4 hours using:

- A hydrogen flow equal to 31.2 Nml/min.
- A carbon monoxide flow equal to 15.6 Nml/min.

1.8.3 Fischer-Tropsch runs

After the catalyst activation, the plant is ready for the FT runs. The reaction conditions used for the experimental runs are shown in Table 2.2:

Table 2.2 - Reaction conditions of the FT experimental runs

H_2/CO	Temperature [°C]	H_2 flow in [Nml/min]	CO flow in [Nml/min]	N_2 flow in [Nml/min]	Pressure [bar]
1	250	23.4	23.4	5.02	20
1	260	23.4	23.4	5.02	20
1.5	250	28.1	18.7	5.02	20
1.5	260	28.1	18.7	5.02	20
2	220	31.2	15.6	5.02	20
2	235	31.2	15.6	5.02	20
2	250	31.2	15.6	5.02	20
2	260	31.2	15.6	5.02	20

The FT runs have durations between 48 and 90 hours. Every hour the micro-GC makes one analysis of the out coming gas flow. At the end of each run the cold trap is opened and both the organic phase and aqueous phase are first separated and then weighted and analysed. Finally, all these data are collected in an Excel database, where it is possible to calculate various parameter like CO conversion or the products selectivities.

2.4 Results and discussion

Thanks to the collected data, it is possible to represent the ASF distribution, CO conversion, C_{2+} yield and CO_2, CH_4, C_2-C_6, C_7-C_{30} selectivities for each one of the tests performed as shown in Figure 2.6 and Figure 2.7:

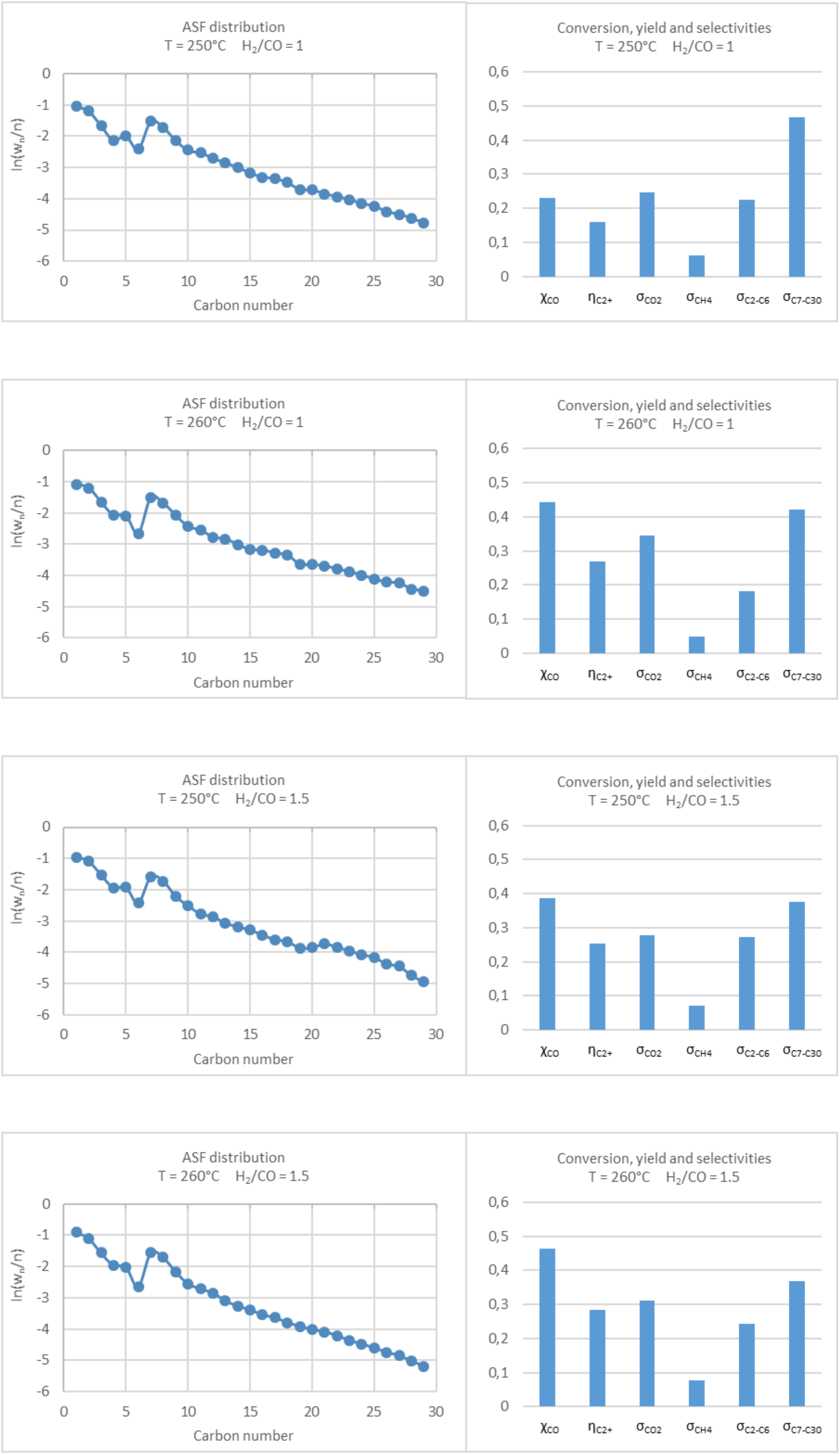

Figure 2.6 - Experimental results (1)

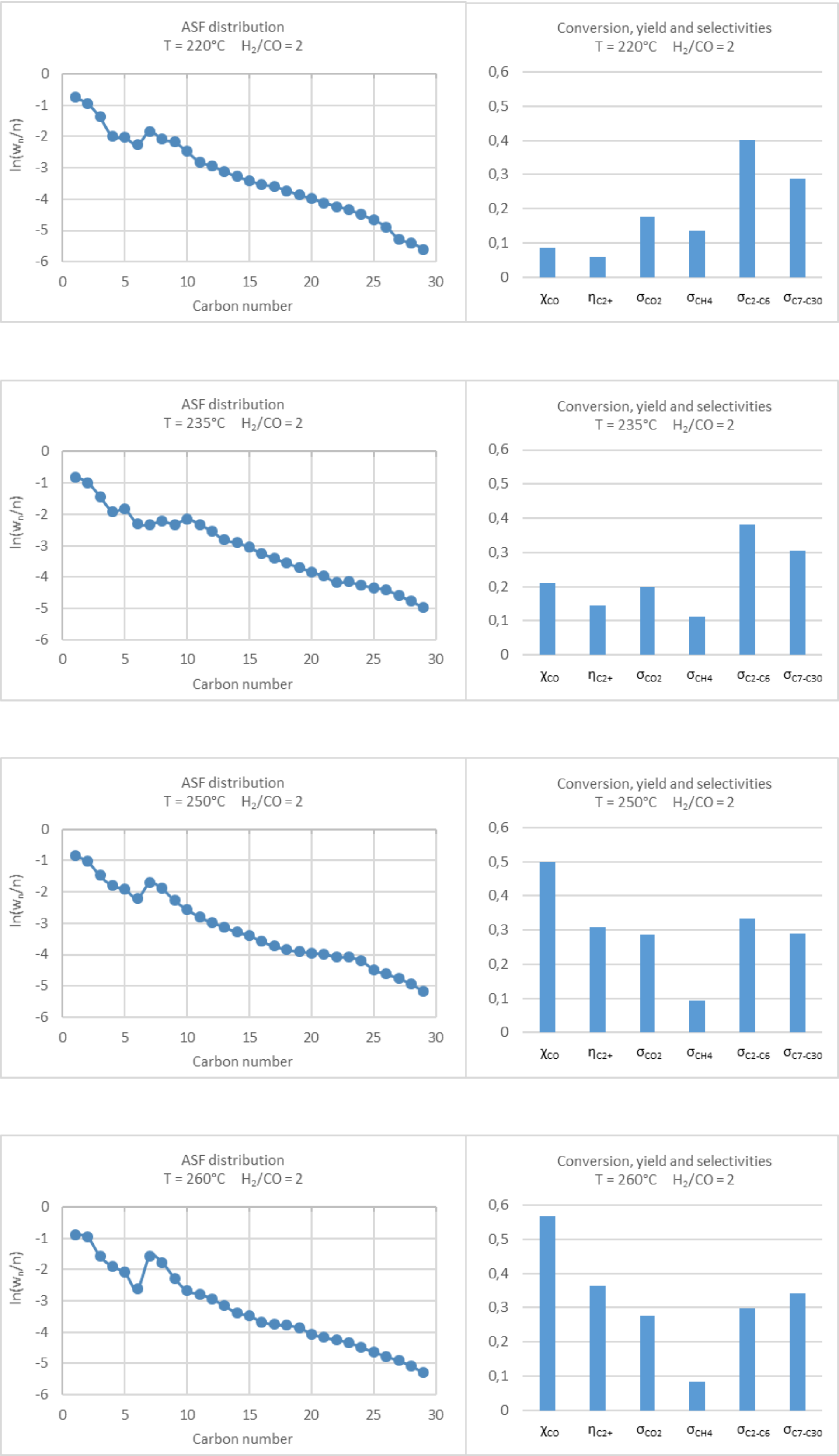

Figure 2.7 - Experimental results (2)

To better visualize the reaction data, the experimental results are also reported in Table 2.3.

Table 2.3 - Experimental results at different H_2/CO ratios and temperatures

				Selectivity [%]			
H_2/CO	**T [°C]**	**CO conversion [%]**	**C_{2+} yield [%]**	**CO_2**	**CH_4**	**C_2-C_6**	**C_7-C_{30}**
1	250	23.0	15.9	24.7	6.1	22.6	46.6
1	260	44.4	26.9	34.7	4.8	18.3	42.3
1.5	250	38.8	25.2	27.9	7.1	27.3	37.7
1.5	260	46.3	28.3	31.0	7.8	24.2	37.0
2	220	8.5	5.9	17.6	13.5	40.0	28.9
2	235	21.0	14.5	19.9	11.3	38.2	30.6
2	250	49.8	31.0	28.6	9.3	33.2	28.9
2	260	56.7	36.3	27.7	8.4	29.7	34.2

From Table 2.3 it is possible to observe that the CO conversion increases with the temperature and the H_2/CO feed ratio. Higher temperatures also lead to a lower selectivity to the hydrocarbon products and a higher selectivity to CO_2, probably due to the increased activity of the WGS reaction. Despite the higher selectivity to CO_2, the overall C_{2+} yield increases with higher temperatures thanks to the concomitant CO conversion increase. Finally, as the H_2/CO feed ratio increases, the hydrocarbon selectivity shifts from heavier to lighter hydrocarbons; this trend is explained by the higher concentration of hydrogen present, which leads to a higher chain termination reaction rate and lower chain growth probability.

3 Laboratory reactor model and kinetic models discrimination

Firstly, in this chapter the reactor model used to simulate the experimental results obtained with the laboratory FT plant is described.

Various kinetic models taken from literature for the FT and WGS reactions are then presented. The parameters of the reaction models are regressed, to better simulate the experimental results.

Finally, a kinetic discrimination is performed to choose the best kinetic model among those examined.

3.1 Laboratory reactor model

The laboratory reactor model can be considered a simplified version of the industrial reactor discussed in chapter 4, given the simplifying assumptions that can be made under the ideal laboratory conditions:

- There are no diffusive resistances inside the catalyst due to its small dimension (between 106 and 150 microns); for this reason, the effectiveness factor of the catalyst pellet is not taken into account for the laboratory reactor model.
- The formation of a liquid phase is not considered, given the low production of heavy products during the experimental runs.
- The temperature of the catalytic bed is considered constant, given the small size of the reactor and the presence of α-Al_2O_3 as diluent.

- Also the pressure is assumed constant, given the short length of the reactor bed.

The material balances of all the reactants and products of the FTS are then the only equations taken into consideration for the ODE model of the laboratory reactor. The mass balances have the following structure, similar to the material balances presented in chapter 4 for the industrial reactor:

$$\dot{w}_{tot} \frac{d\omega_i}{dV} = \rho_{cat} \cdot (1-\varepsilon) \cdot \psi \cdot \sum_{j=1}^{N_R} \nu_{i,j} \cdot r_j \cdot M_i \tag{3.1}$$

where $\dot{w}_{tot}$ is the total mass flow rate, ω_i the mass fraction of component i, ρ_{cat} the catalyst density, ε the fixed bed void fraction, ψ the ratio between the catalyst volume and the total solid volume, $\nu_{i,j}$ the stoichiometric coefficient of the i^{th} component for the j^{th} chemical reaction r_j and M_i the molecular weight of component i. The reaction rates r_j for the FT and WGS reactions are discussed in the following section.

3.2 Kinetic models

The Fischer-Tropsch synthesis for an iron catalyst can be simplified as a combination of the FT and WGS reaction [48]:

$$CO + U_{H_2} H_2 \xrightarrow{r_{FT}} \sum_{i=1}^{\infty} \nu_i C_i H_{2i+2} + H_2O \tag{3.2}$$

$$CO + H_2O \underset{}{\overset{r_{WGS}}{\rightleftarrows}} CO_2 + H_2 \tag{3.3}$$

The stoichiometric coefficients ν_i of the hydrocarbons follow the Anderson-Schulz-Flory distribution model (seen in section 1.6.1). Their values are a function of the chain growth probability α; for this thesis in particular, α has been evaluated with the equation proposed by Lox and Froment [49, 50]:

$$\alpha = \frac{k_1 P_{CO}}{k_1 P_{CO} + k_2 P_{H_2} + k_3} \tag{3.4}$$

The k_i parameters can be obtained as a function of temperature by using the following equation:

$$k_i = k_{ref,i} \exp\left(-\frac{E_{act,i}}{R_{gas}} \left(\frac{1}{T} - \frac{1}{T_{ref}} \right) \right) \tag{3.5}$$

where the reference temperature T_{ref} is 573 K and the $k_{ref,i}$, $E_{act,i}$ constants are reported in Appendix A.

After calculating the chain growth probability, it is possible to derive the stoichiometric coefficients of the hydrocarbons with i carbon atoms:

$$\nu_i = (1-\alpha)^2 \alpha^{i-1} \tag{3.6}$$

It can be noted by looking at equation (3.6) that the sum $\sum_{i=1}^{\infty} i\nu_i$ is equal to 1, which respects the balance of carbon atoms.

Always thanks to α, the hydrogen usage U_{H_2} for the FT reaction balance (3.2) can be calculated:

$$U_{H_2} = (3-\alpha)\frac{1}{1-\gamma} + \left((1-\alpha)^2 + 2\right)\frac{\gamma}{1-\gamma} \tag{3.7}$$

The hydrogen usage, written in this way, takes into account the production of olefin and paraffin through their ratio, γ. In particular, $(3-\alpha)$ represents the hydrogen usage for paraffin formation, while $\left((1-\alpha)^2 + 2\right)$ considers the olefin production.

For the calculation of the FT and WGS reaction rates, many kinetic models taken from the literature have been examined and compared. The first model was proposed by Zimmerman and Bukur [51]:

$$r_{FT_{ZB}} = k_{FT} \frac{P_{H_2} P_{CO}}{P_{CO} + a_{FT} P_{H_2O} + b_{FT} P_{CO_2}} \tag{3.8}$$

$$r_{WGS_{ZB}} = k_{WGS} \frac{P_{CO} P_{H_2O} - \frac{P_{H_2} P_{CO_2}}{K_p}}{P_{CO} + a_{WGS} P_{H_2O} + b_{WGS} P_{CO_2}} \tag{3.9}$$

Afterwards, the various reaction rate expressions analysed by van der Laan and Beenackers in their work were considered [48]:

$$r_{FT_{VB-I}} = k_{FT} \frac{P_{H_2}^{0.5} P_{CO}}{\left(1 + a_{FT} P_{CO} + b_{FT} P_{H_2O}\right)^2} \tag{3.10}$$

$$r_{FT_{VB-II}} = k_{FT} \frac{P_{H_2} P_{CO}}{\left(1 + a_{FT} P_{CO} + b_{FT} P_{H_2O}\right)^2} \tag{3.11}$$

$$r_{FT_{VB-III}} = k_{FT} \frac{P_{H_2} P_{CO}}{1 + a_{FT} P_{CO} + b_{FT} P_{H_2O}} \tag{3.12}$$

$$r_{WGS_{VB-I}} = k_{WGS} \frac{P_{CO} P_{H_2O} - \frac{P_{H_2} P_{CO_2}}{K_p}}{\left(1 + a_{WGS} P_{CO} + b_{WGS} P_{H_2O}\right)^2} \tag{3.13}$$

$$r_{WGS_{VB-II}} = k_{WGS} \frac{\frac{P_{CO} P_{H_2O}}{P_{H_2}^{0.5}} - \frac{P_{H_2}^{0.5} P_{CO_2}}{K_p}}{\left(1 + a_{WGS} P_{CO} + b_{WGS} P_{H_2O}\right)^2} \tag{3.14}$$

The kinetic constants k_i of the reaction models have the following form:

$$k_i = k_i^0 \exp\left(-\frac{E_{act,i}}{R_{gas} T} \right) \tag{3.15}$$

All the parameters, different for each reaction rate, are reported in Appendix A.

These models, used with their original kinetic parameters found in the literature, fail to simulate satisfactorily the experimental results of the laboratory reactor. As an example, the model proposed by Zimmerman and Bukur behaves as shown in Figure 3.1.

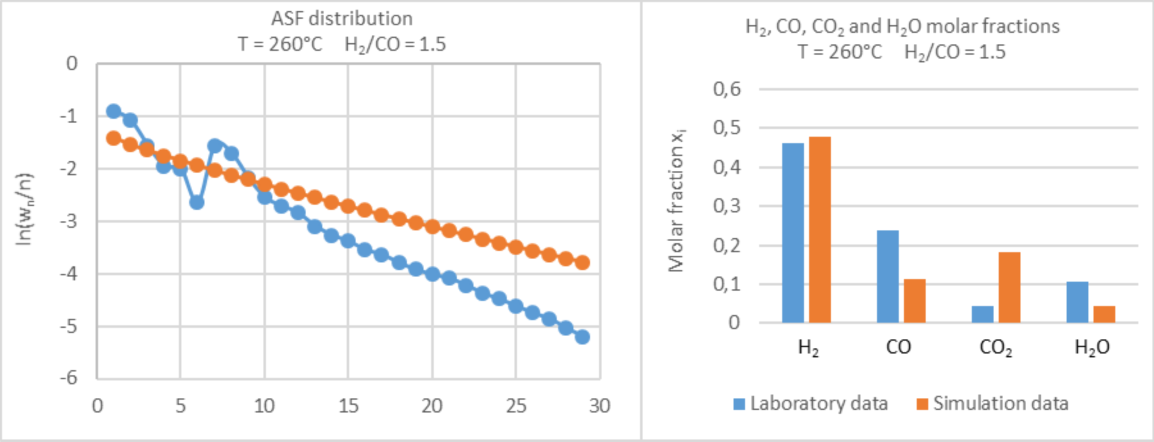

Figure 3.1 - Zimmerman and Bukur model results

In this case the calculated hydrocarbon distribution does not deviate excessively from the real distribution measured in the laboratory. However the model, with its original parameters, does not simulate correctly the outlet molar fraction of the main components, probably overestimating the WGS reaction rate.

The same holds true for all the other examined kinetic models, which tend to overestimate or underestimate the H_2, CO, CO_2 and H_2O compositions at the reactor outlet. For this reason, it was decided to perform a regression of the kinetic parameters to improve the predictive ability of the models and then choose the most accurate.

3.3 Data regression

The nonlinear regression of the kinetic parameters has been implemented in the MATLAB environment. The chosen solver, lsqnonlin, solves nonlinear least squares curve fitting problems of the form:

$$\begin{gathered} \min_x \| f(x) \|_2^2 = \min_x \left(f_1(x)^2 + f_2(x)^2 + \ldots + f_n(x)^2 \right) \\ f(x) = w_{i,j}^{\exp} - w_{i,j}^{sim} \qquad i = 1, \ldots, N_{runs} \qquad j = 1, \ldots, N_{comp} \end{gathered} \tag{3.16}$$

where, in this case, the function $f(x)$ consists of the differences between the mass fractions $w_{i,j}^{\exp}$ of the laboratory data and the mass fractions $w_{i,j}^{sim}$ of the simulation, for all the performed experimental runs N_{runs} and the measured components N_{comp}. The lsqnonlin solver is chosen because, in addition to solving nonlinear least squares problems, allows to optionally set lower and upper bounds for the x regressed values; in fact, the regressed parameters, being kinetic constants, need to be greater than zero. The $w_{i,j}^{sim}$ mass fractions values are obtained from the solution of the ODEs system of mass balances in the form shown in equation (3.1). Given the high number of data measured during the laboratory experiments at different temperatures and H_2/CO ratios, it is possible to regress the needed kinetic parameters for different couplings of FT and WGS reactions. The examined seven couplings are reported in Table 3.1:

Table 3.1 - FT and WGS reaction sets

	Fischer-Tropsch reaction rate	**Water-gas shift reaction rate**
Zimmerman and Bukur $r_{FT_{ZB}} / r_{WGS_{ZB}}$	$r_{FT_{ZB}} = k_{FT}\frac{P_{H_2}P_{CO}}{P_{CO}+a_{FT}P_{H_2O}+b_{FT}P_{CO_2}}$	$r_{WGS_{ZB}} = k_{WGS}\frac{P_{CO}P_{H_2O}-\frac{P_{H_2}P_{CO_2}}{K_p}}{P_{CO}+a_{WGS}P_{H_2O}+b_{WGS}P_{CO_2}}$
van der Laan and Beenackers $r_{FT_{VB-I}} / r_{WGS_{VB-I}}$	$r_{FT_{VB-I}} = k_{FT}\frac{P_{H_2}^{0.5}P_{CO}}{\left(1+a_{FT}P_{CO}+b_{FT}P_{H_2O}\right)^2}$	$r_{WGS_{VB-I}} = k_{WGS}\frac{P_{CO}P_{H_2O}-\frac{P_{H_2}P_{CO_2}}{K_p}}{\left(1+a_{WGS}P_{CO}+b_{WGS}P_{H_2O}\right)^2}$
van der Laan and Beenackers $r_{FT_{VB-I}} / r_{WGS_{VB-II}}$	$r_{FT_{VB-I}} = k_{FT}\frac{P_{H_2}^{0.5}P_{CO}}{\left(1+a_{FT}P_{CO}+b_{FT}P_{H_2O}\right)^2}$	$r_{WGS_{VB-II}} = k_{WGS}\frac{\frac{P_{CO}P_{H_2O}}{P_{H_2}^{0.5}}-\frac{P_{H_2}^{0.5}P_{CO_2}}{K_p}}{\left(1+a_{WGS}P_{CO}+b_{WGS}P_{H_2O}\right)^2}$
van der Laan and Beenackers $r_{FT_{VB-II}} / r_{WGS_{VB-I}}$	$r_{FT_{VB-II}} = k_{FT}\frac{P_{H_2}P_{CO}}{\left(1+a_{FT}P_{CO}+b_{FT}P_{H_2O}\right)^2}$	$r_{WGS_{VB-I}} = k_{WGS}\frac{P_{CO}P_{H_2O}-\frac{P_{H_2}P_{CO_2}}{K_p}}{\left(1+a_{WGS}P_{CO}+b_{WGS}P_{H_2O}\right)^2}$
van der Laan and Beenackers $r_{FT_{VB-II}} / r_{WGS_{VB-II}}$	$r_{FT_{VB-II}} = k_{FT}\frac{P_{H_2}P_{CO}}{\left(1+a_{FT}P_{CO}+b_{FT}P_{H_2O}\right)^2}$	$r_{WGS_{VB-II}} = k_{WGS}\frac{\frac{P_{CO}P_{H_2O}}{P_{H_2}^{0.5}}-\frac{P_{H_2}^{0.5}P_{CO_2}}{K_p}}{\left(1+a_{WGS}P_{CO}+b_{WGS}P_{H_2O}\right)^2}$
van der Laan and Beenackers $r_{FT_{VB-III}} / r_{WGS_{VB-I}}$	$r_{FT_{VB-III}} = k_{FT}\frac{P_{H_2}P_{CO}}{1+a_{FT}P_{CO}+b_{FT}P_{H_2O}}$	$r_{WGS_{VB-I}} = k_{WGS}\frac{P_{CO}P_{H_2O}-\frac{P_{H_2}P_{CO_2}}{K_p}}{\left(1+a_{WGS}P_{CO}+b_{WGS}P_{H_2O}\right)^2}$
van der Laan and Beenackers $r_{FT_{VB-III}} / r_{WGS_{VB-II}}$	$r_{FT_{VB-III}} = k_{FT}\frac{P_{H_2}P_{CO}}{1+a_{FT}P_{CO}+b_{FT}P_{H_2O}}$	$r_{WGS_{VB-II}} = k_{WGS}\frac{\frac{P_{CO}P_{H_2O}}{P_{H_2}^{0.5}}-\frac{P_{H_2}^{0.5}P_{CO_2}}{K_p}}{\left(1+a_{WGS}P_{CO}+b_{WGS}P_{H_2O}\right)^2}$

The three FT reactions rates by van der Laan and Beenackers are coupled with the two WGS reactions from the same paper to check if, with the iron catalyst under examination, one of these combination is better than the others (in the original work the reaction rate models were statistically indistinguishable).

In addition to the kinetic constants of the FT and WGS reactions, also the parameters of the chain growth probability expression are regressed for each one of the reactions set shown in Table 3.1.

Recapping, the x parameters regressed for each set are listed in Table 3.2.

Table 3.2 - Regressed parameters

	Parameters
Chain growth probability (3.4-5)	$k_{ref,1}$ $k_{ref,2}$ $k_{ref,3}$ $E_{act,2}$ $E_{act,3}$
FT reaction rate (3.8, 3.10-12, 3.15)	k_{FT}^0 $E_{act,\mathrm{FT}}$ a_{FT} b_{FT}
WGS reaction rate (3.9, 3.13-15)	k_{WGS}^0 $E_{act,\mathrm{WGS}}$ a_{WGS} b_{WGS}

3.4 Kinetic model discrimination

The regressions, performed with MATLAB® R2014a, were calculated for all the reaction sets. The discrimination criterion chosen to determine the best reactions model set is the mean squared error (MSE), which has the following expression for the problem in question:

$$MSE = \frac{1}{\left(N_{runs} \times N_{comp}\right)} \sum_{i=1}^{N_{runs}} \sum_{j=1}^{N_{comp}} \left(w_{i,j}^{\exp} - w_{i,j}^{sim}\right)^2 \tag{3.17}$$

The values of the MSE for each regressed set are reported in the following table:

Table 3.3 - Regression results

	Fischer-Tropsch reaction rate	**Water-gas shift reaction rate**	**Mean Squared Error**
Zimmerman and Bukur $r_{FT_{ZB}} / r_{WGS_{ZB}}$	$r_{FT_{ZB}} = k_{FT} \frac{P_{H_2} P_{CO}}{P_{CO} + a_{FT} P_{H_2O} + b_{FT} P_{CO_2}}$	$r_{WGS_{ZB}} = k_{WGS} \frac{P_{CO} P_{H_2O} - \frac{P_{H_2} P_{CO_2}}{K_p}}{P_{CO} + a_{WGS} P_{H_2O} + b_{WGS} P_{CO_2}}$	5.8551×10^{-5}
van der Laan and Beenackers $r_{FT_{VB-I}} / r_{WGS_{VB-I}}$	$r_{FT_{VB-I}} = k_{FT} \frac{P_{H_2}^{0.5} P_{CO}}{\left(1 + a_{FT} P_{CO} + b_{FT} P_{H_2O}\right)^2}$	$r_{WGS_{VB-I}} = k_{WGS} \frac{P_{CO} P_{H_2O} - \frac{P_{H_2} P_{CO_2}}{K_p}}{\left(1 + a_{WGS} P_{CO} + b_{WGS} P_{H_2O}\right)^2}$	2.6160×10^{-4}
van der Laan and Beenackers $r_{FT_{VB-I}} / r_{WGS_{VB-II}}$	$r_{FT_{VB-I}} = k_{FT} \frac{P_{H_2}^{0.5} P_{CO}}{\left(1 + a_{FT} P_{CO} + b_{FT} P_{H_2O}\right)^2}$	$r_{WGS_{VB-II}} = k_{WGS} \frac{\frac{P_{CO} P_{H_2O}}{P_{H_2}^{0.5}} - \frac{P_{H_2}^{0.5} P_{CO_2}}{K_p}}{\left(1 + a_{WGS} P_{CO} + b_{WGS} P_{H_2O}\right)^2}$	1.2972×10^{-4}
van der Laan and Beenackers $r_{FT_{VB-II}} / r_{WGS_{VB-I}}$	$r_{FT_{VB-II}} = k_{FT} \frac{P_{H_2} P_{CO}}{\left(1 + a_{FT} P_{CO} + b_{FT} P_{H_2O}\right)^2}$	$r_{WGS_{VB-I}} = k_{WGS} \frac{P_{CO} P_{H_2O} - \frac{P_{H_2} P_{CO_2}}{K_p}}{\left(1 + a_{WGS} P_{CO} + b_{WGS} P_{H_2O}\right)^2}$	1.3855×10^{-4}
van der Laan and Beenackers $r_{FT_{VB-II}} / r_{WGS_{VB-II}}$	$r_{FT_{VB-II}} = k_{FT} \frac{P_{H_2} P_{CO}}{\left(1 + a_{FT} P_{CO} + b_{FT} P_{H_2O}\right)^2}$	$r_{WGS_{VB-II}} = k_{WGS} \frac{\frac{P_{CO} P_{H_2O}}{P_{H_2}^{0.5}} - \frac{P_{H_2}^{0.5} P_{CO_2}}{K_p}}{\left(1 + a_{WGS} P_{CO} + b_{WGS} P_{H_2O}\right)^2}$	1.2164×10^{-4}
van der Laan and Beenackers $r_{FT_{VB-III}} / r_{WGS_{VB-I}}$	$r_{FT_{VB-III}} = k_{FT} \frac{P_{H_2} P_{CO}}{1 + a_{FT} P_{CO} + b_{FT} P_{H_2O}}$	$r_{WGS_{VB-I}} = k_{WGS} \frac{P_{CO} P_{H_2O} - \frac{P_{H_2} P_{CO_2}}{K_p}}{\left(1 + a_{WGS} P_{CO} + b_{WGS} P_{H_2O}\right)^2}$	1.6316×10^{-4}
van der Laan and Beenackers $r_{FT_{VB-III}} / r_{WGS_{VB-II}}$	$r_{FT_{VB-III}} = k_{FT} \frac{P_{H_2} P_{CO}}{1 + a_{FT} P_{CO} + b_{FT} P_{H_2O}}$	$r_{WGS_{VB-II}} = k_{WGS} \frac{\frac{P_{CO} P_{H_2O}}{P_{H_2}^{0.5}} - \frac{P_{H_2}^{0.5} P_{CO_2}}{K_p}}{\left(1 + a_{WGS} P_{CO} + b_{WGS} P_{H_2O}\right)^2}$	1.9476×10^{-4}

From Table 3.3 it can be noted that the reactions set by Zimmerman and Bukur has the lowest MSE, thus proving to be the best model able to simulate the experimental kinetic data. On the other hand, the reactions sets by van der Laan and Beenackers present a more than double MSE compared to the best model; for this reason, they are therefore discarded.

In Table 3.4 the values of the regressed parameters for the chain growth probability equation by Lox and Froment and the FT and WGS reactions by Zimmerman and Bukur are reported.

Table 3.4 - Regressed parameters values for Lox and Froment-Zimmerman and Bukur reactions set

PARAMETER	REGRESSED VALUE	UNIT OF MEASURE
$k_{ref,1}$	1.4216×10^{-10}	$kmol/\left(kg\cdot s\cdot Pa\right)$
$k_{ref,2}$	4.9936×10^{-9}	$kmol/\left(kg\cdot s\cdot Pa\right)$
$k_{ref,3}$	1.5344×10^{-5}	$kmol/\left(kg\cdot s\right)$
$E_{act,2}$	3.9484×10^{5}	kJ/mol
$E_{act,3}$	3.3658×10^{-2}	kJ/mol
k_{FT}^{0}	7.1012×10^{5}	$mol/\left(s\cdot kg\cdot Pa\right)$
$E_{act,\mathrm{FT}}$	1.3601×10^{5}	J/mol
a_{FT}	8.7499×10^{-2}	Pa^{-1}
b_{FT}	1.7283×10	Pa^{-1}
k_{WGS}^{0}	1.9335×10^{9}	$mol/\left(s\cdot kg\cdot Pa\right)$
$E_{act,\mathrm{WGS}}$	1.6520×10^{5}	J/mol
a_{WGS}	1.0826×10	Pa^{-1}
b_{WGS}	$0.$	Pa^{-1}

Finally, the simulated ASF hydrocarbon distribution and molar compositions of H_2, CO, CO_2 and H_2O are compared with the corresponding experimental data in Figure 3.2 and Figure 3.3. The reactor simulation in general approximates the provided experimental data quite well. Only the ASF distribution tends to overestimate the production of heavier hydrocarbons; this deviation is probably due to the lower mass fractions in play for these components compared to the other ones, therefore affecting less the MSE final value.

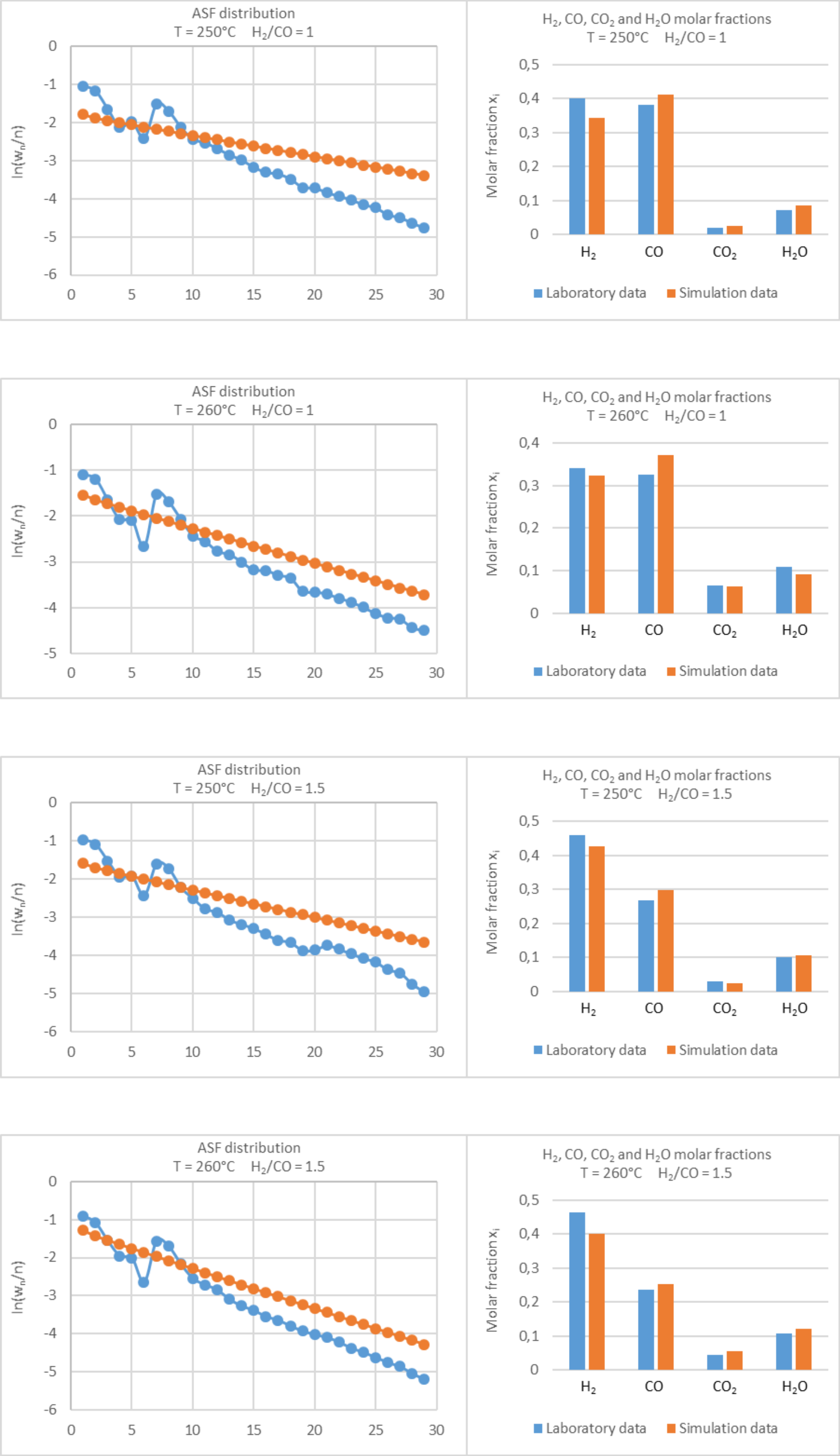

Figure 3.2 - Lox and Froment-Zimmerman and Bukur reactions model results (1)

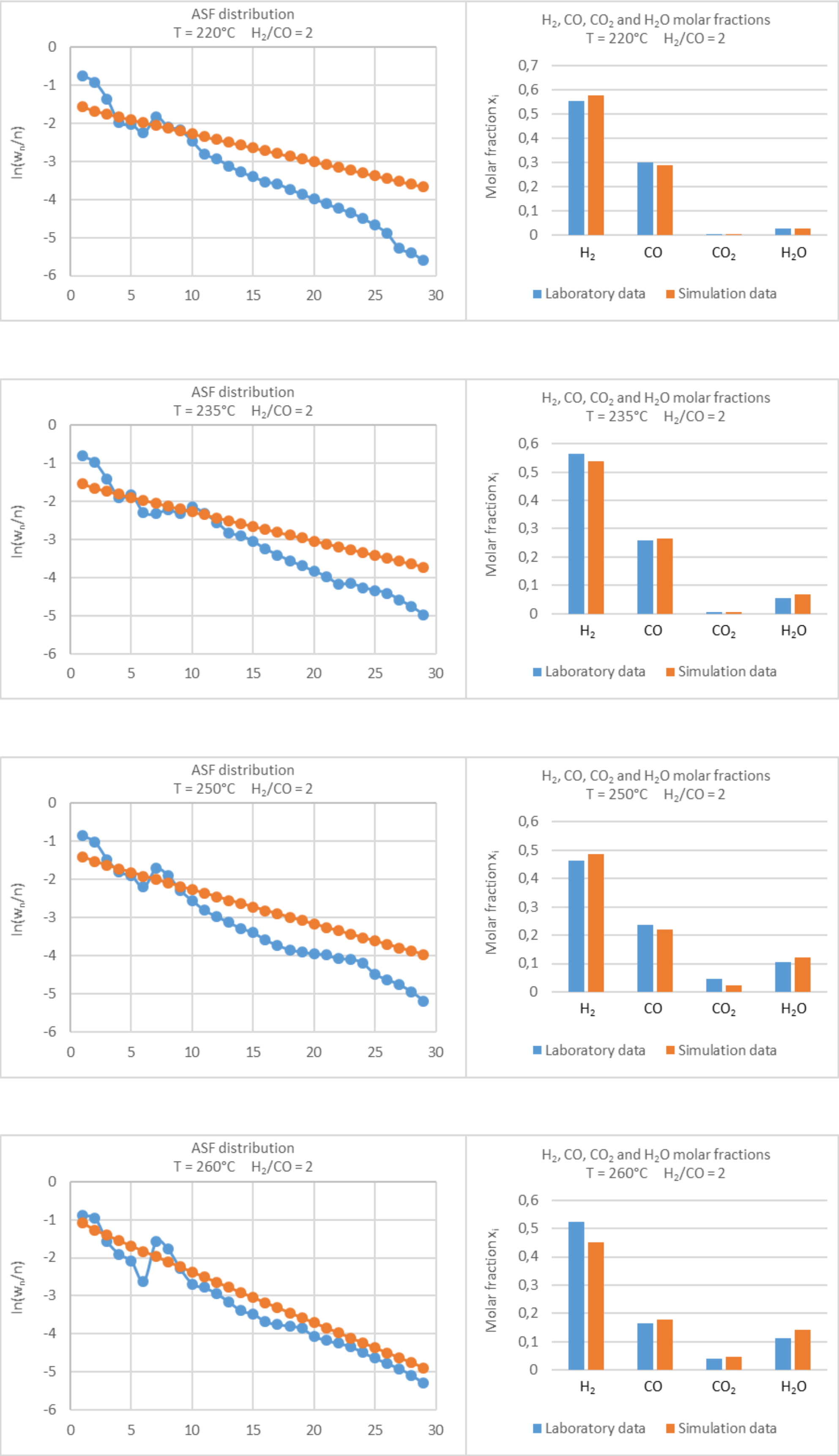

Figure 3.3 - Lox and Froment-Zimmerman and Bukur reactions model results (2)

4 Industrial Fischer-Tropsch reactor model

The kinetic model selected in the last chapter, with its regressed parameters, is now inserted in the simulation of the industrial FT reactor. The industrial reactor model, explained in the following sections, will be then used to perform the plant-wide economic optimization described in the next chapter.

In particular, this chapter focuses on the description of the mass and energy balances of the reactor model, taking into account the diffusion resistances within the catalyst pellet and the possible formation of a liquid phase of heavy hydrocarbon products.

4.1 Lumping of hydrocarbon components

First of all, given the high number of hydrocarbon species and respective mass balances which should be considered for the reactor model, it is preferred to group these components into lumps. The hydrocarbon species are thus divided into the following six groups:

1. C_1 methane
2. C_2 ethane and ethylene
3. C_3 propane and propene
4. C_4 butane and butene
5. C_5-C_{10} lump (gasoline)
6. C_{11+} lump (diesel and waxes)

The lump introduction in the reactor model changes the FT reaction balance expression (3.2):

$$CO + U_{H_2} H_2 \xrightarrow{r_{FT}} \nu_1 C_1 + \nu_2 C_2 + \nu_3 C_3 + \nu_4 C_4 + \nu_{[5-10]} C_{[5-10]} + \nu_{[11-\infty]} C_{[11-\infty]} + H_2O \tag{4.1}$$

The stoichiometric coefficient of a lump is equal to the sum of the stoichiometric coefficients of the hydrocarbons which compose that lump. The stoichiometric coefficient of a lump of hydrocarbons with i to j carbon atoms is then given by:

$$\nu_{[i-j]} = \sum_{k=i}^{j} \nu_k = (1-\alpha)\left(\alpha^{i-1} - \alpha^{j}\right) \tag{4.2}$$

$$\nu_{[i-\infty]} = \sum_{k=i}^{\infty} \nu_k = (1-\alpha)\alpha^{i-1} \tag{4.3}$$

The average carbon number for each lump can be similarly obtained using the ASF distribution as illustrated by Marano and Holder [52]:

$$n_{C_{[i-j]}} = i + \frac{\alpha}{1-\alpha} - \frac{(j-i+1)\alpha^{j-i+1}}{1-\alpha^{j-i+1}} \tag{4.4}$$

$$n_{C_{[i-\infty]}} = i + \frac{\alpha}{1-\alpha} \tag{4.5}$$

Consequently, also the mean molecular weight of each lump can be derived:

$$M_{[i-j]} = 14 n_{C_{[i-j]}} + \frac{2}{1+\gamma} \tag{4.6}$$

where the olefin to paraffin ratio γ is set to 0.35, as proposed by Rafiee and Hillestad [53].

The average carbon numbers of the lumps are also required to estimate critical properties needed for the vapour-liquid equilibrium. In fact, thanks to the asymptotic behaviour correlations proposed by Marano and Holder [54-56], it is possible to calculate the critical temperature, pressure and the acentric factor of each lump as a function of n_C.

4.2 Industrial reactor model

The industrial reactor type chosen to simulate is a multi-tubular fixed bed reactor as shown in Figure 4.1. The catalyst pellets are contained inside the tubes while outside boiling water is used to remove the heat of reaction.

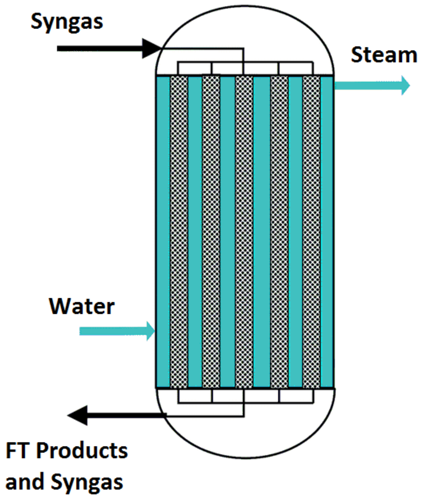

Figure 4.1 - Multi-tubular fixed bed reactor

The industrial reactor model, while dropping the simplifying assumptions introduced for the laboratory reactor model in section 3.1, does not take into account:

1. The interphase mass transfer resistances between fluid and solid phase, therefore considering a pseudo-homogeneous model.
2. The mass and temperature gradients of the reactor along the radial coordinate, therefore considering a one-dimensional axial model.

Based on these assumptions, the mass balance equations for each component are:

$$\dot{w}_{tot}\frac{d\omega_i}{dV}=\rho_{cat}\cdot(1-\varepsilon)\cdot\sum_{j=1}^{N_R}\nu_{i,j}\cdot r_{eff,j}\cdot M_i \tag{4.7}$$

It can be noted that the main difference with equation (3.1) is the introduction of the effective reaction rate $r_{eff,j}$ term, which takes into account the effectiveness factor of the catalyst pellet model discussed in section 4.3.

Similarly, the energy balance can be written as:

$$\dot{w}_{tot} \cdot \hat{c}_{p,mix} \frac{dT}{dV} = \rho_{cat} \cdot (1-\varepsilon) \cdot \sum_{j=1}^{N_R} \left(-\Delta\tilde{H}_{R,j}\right) \cdot r_{eff,j} + U \frac{4}{D_T} (T_{cool} - T) \tag{4.8}$$

where $\hat{c}_{p,mix}$ is the specific heat of mixture, $\Delta\tilde{H}_{R,j}$ the enthalpy of the j^{th} reaction, U the overall heat transfer coefficient and $4/D_T$ the specific area of a cylindrical tube. The energy balance is then modified to consider the possible condensation or vaporization of a dn amount of liquid:

$$\dot{w}_{tot} \cdot \hat{c}_{p,mix} \frac{dT}{dV} = \rho_{cat} \cdot (1-\varepsilon) \cdot \sum_{j=1}^{N_R} \left(-\Delta\tilde{H}_{R,j}\right) \cdot r_{eff,j} + \sum_{i=1}^{N_{comp}} \Delta\tilde{H}_{V,i} \cdot x_i \cdot dn + U \frac{4}{D_T} (T_{cool} - T) \tag{4.9}$$

where $\Delta\tilde{H}_{V,i}$ is the molar enthalpy of vaporization of the i^{th} component. The enthalpy of vaporization values are estimated at a given reactor temperature using correlations from Perry's Handbook [57]; for the hydrocarbons, the heat of vaporization is calculated as a function of temperature and chain length, with a regression similar to the one performed for the heat of reaction in the following section:

$$\Delta\tilde{H}_{V,i} = A(T)i + B(T) \tag{4.10}$$

At last, the pressure drop through the reactor is evaluated using the Ergun equation:

$$\begin{gathered} \frac{dP}{dV} = -\left(1.75 + 150\left(\frac{1-\varepsilon}{\mathrm{Re}}\right)\right)\left(\frac{u^2 \cdot \rho_{gas}}{D_p}\left(\frac{1-\varepsilon}{\varepsilon^3}\right)\right)\frac{1}{A_{i,tot}} \\ \mathrm{Re} = \frac{\rho_{gas} \cdot u \cdot D_p}{\mu_{gas}} \end{gathered} \tag{4.11}$$

where u is the gas velocity, ρ_{gas} the gas density, μ_{gas} the gas dynamic viscosity, D_p the pellet diameter and $A_{i,tot}$ the internal cross section area of all the tubes that compose the reactor.

4.2.1 Heat of reaction

The enthalpy of the j^{th} reaction is given by the following sum:

$$\Delta\tilde{H}_{R,j} = \sum_{i=1}^{N_{comp}} \nu_{i,j}\Delta\tilde{H}_{f,i} \tag{4.12}$$

The enthalpy of formation $\Delta\tilde{H}_{f,i}$ of each component involved in the j^{th} reaction at the reactor temperature is calculated starting from the reference temperature T_{ref}:

$$\Delta\tilde{H}_{f,i} = \Delta\tilde{H}^{0}_{f,i}\left(T_{ref}\right) + \int_{T_{ref}}^{T} \tilde{c}_p dT \tag{4.13}$$

where $\tilde{c}_p$ is the molar specific heat of component i. However, the enthalpy of formation of the hydrocarbon products is not evaluated with formula (4.13). It is instead estimated as a linear function of the chain length:

$$\Delta\tilde{H}_{f_{HC},i} = ai + b \tag{4.14}$$

The a and b coefficients are obtained through a regression performed using enthalpy values from Perry's Handbook [57] at a temperature close to the one inside the reactor, with a procedure similar to the one proposed by Chaumette et al. [58]. The enthalpy of the FT reaction is therefore equal to:

$$\Delta\tilde{H}_{R,\mathrm{FT}} = \sum_{i=1}^{\infty}\nu_i\Delta\tilde{H}_{f_{HC},\mathrm{i}} + \Delta\tilde{H}_{f,\mathrm{H}_2O} - \Delta\tilde{H}_{f,\mathrm{CO}} - U_{H_2}\Delta\tilde{H}_{f,\mathrm{H}_2} \tag{4.15}$$

This equation can be further reformulated by introducing the expression of the enthalpy of formation of the hydrocarbons (4.14) and the formula of the hydrogen usage (3.7):

$$\Delta\tilde{H}_{R,\mathrm{FT}} = a + b + \Delta\tilde{H}_{f,\mathrm{H}_2O} - \Delta\tilde{H}_{f,\mathrm{CO}} - 3\Delta\tilde{H}_{f,\mathrm{H}_2} + \left(\frac{1+2\gamma}{1+\gamma}\Delta\tilde{H}_{f,\mathrm{H}_2} - b\right)\cdot\alpha - \frac{\gamma}{1+\gamma}\Delta\tilde{H}_{f,\mathrm{H}_2}\cdot\alpha^2 \tag{4.16}$$

Written in this way, the enthalpy of the FT reaction shows to be a function of both the temperature and the chain growth probability. The enthalpy of the WGS on the other hand is a function of temperature alone:

$$\Delta\tilde{H}_{R,\mathrm{WGS}} = \Delta\tilde{H}_{f,\mathrm{H_2}} + \Delta\tilde{H}_{f,\mathrm{CO_2}} - \Delta\tilde{H}_{f,\mathrm{CO}} - \Delta\tilde{H}_{f,\mathrm{H_2}O} \tag{4.17}$$

4.2.2 Overall heat transfer coefficient

The value of the overall heat transfer coefficient U, necessary for the evaluation of the energy balance (4.9), can be calculated as the reciprocal of the sum of a series of thermal resistances shown in Figure 4.2.

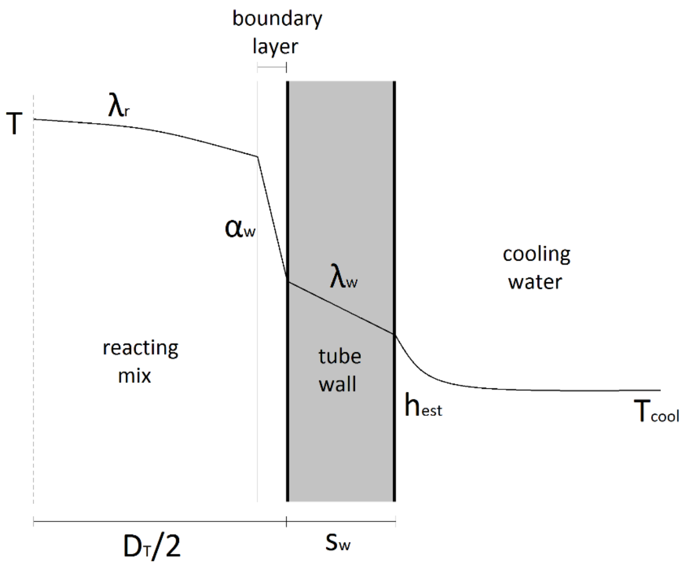

Figure 4.2 - Thermal resistances for a reactor tube

The U coefficient is equal to:

$$\frac{1}{U} = R_{\substack{reacting\\mix}} + R_{\substack{boundary\\layer}} + R_{\substack{tube\\wall}} + R_{\substack{cooling\\water}} = \frac{D_T}{8\lambda_r} + \frac{1}{\alpha_w} + \frac{s_w}{\lambda_w} + \frac{1}{h_{est}} \tag{4.18}$$

where λ_r is the effective radial conductivity of the reacting mixture, α_w the heat transfer coefficient of the boundary layer, λ_w the wall thermal conductivity and h_{est} the heat transfer of the cooling water. Since the values of λ_w for a metal tube and h_{est} for boiling water are very high, their corresponding resistances can be neglected. The formula of U then becomes:

$$\frac{1}{U} = \frac{D_T}{8\lambda_r} + \frac{1}{\alpha_w} \tag{4.19}$$

The values of the effective radial conductivity λ_r and the heat transfer coefficient α_w are estimated with the correlations proposed by Wen et al. [59].

4.3 Catalyst pellet model

The catalytic pellet size and the non-negligible presence of liquid hydrocarbon products inside the catalyst pores lead to consider the intraporous diffusional resistances. As opposed to the normal reaction rates r_j used in the laboratory model, the industrial reactor model uses the effective reaction rates $r_{eff,j}$ which take into account the internal mass transport resistances trough the η_j effectiveness factors:

$$r_{eff,j} = \eta_j \cdot r_j \tag{4.20}$$

where the r_j reaction rates are calculated at the pellet surface molar concentrations $C_{i,s}$. The effectiveness factor is therefore defined as:

$$\eta_j = \frac{\text{pellet average reaction rate}}{\text{superficial reaction rate}} = \frac{1}{r_j(C_{i,s})} \frac{\int_0^{V_p} r_j(C_i) dV}{V_P} \tag{4.21}$$

The catalyst pellet is assumed to be spherical and, due to its relatively small size, isothermal. In order to find the effectiveness value, the mass balance inside the pellet for a generic component i must be considered:

$$\mathcal{D}_{eff,i} \nabla^2 C_i = -\rho_{cat} \sum_{j=1}^{N_R} \nu_{i,j} \cdot r_j \tag{4.22}$$

where the diffusive mass flux is given by Fick's first law of diffusion formula. The effective diffusion coefficient $\mathcal{D}_{eff,i}$ for each component is obtained with the empirical formula proposed by Jianmin et al. [60] and corrected with the pellet void fraction and tortuosity:

$$\mathcal{D}_{eff,i} = \mathcal{D}_i \frac{\varepsilon_{cat}}{\tau_{cat}} \tag{4.23}$$

Equation (4.22) can be also written in spherical coordinates:

$$\frac{d^2 C_i}{dr^2} + \frac{2}{r}\frac{dC_i}{dr} = -\frac{\rho_{cat}}{\mathcal{D}_{eff,i}} \sum_{j=1}^{N_R} \nu_{i,j} \cdot r_j \tag{4.24}$$

The spatial coordinate is then normalized by dividing it for the pellet radius $\xi = r/R_P$ and the molar concentrations are replaced with the molar fractions to obtain the internal mass balance used in the calculations:

$$\frac{d^2 y_i}{d\xi^2} + \frac{2}{\xi}\frac{dy_i}{d\xi} = -R_P^2 \frac{\rho_{cat}}{\mathcal{D}_{eff,i}} \frac{R_{gas} \cdot T}{P} \sum_{j=1}^{N_R} \nu_{i,j} \cdot r_j \tag{4.25}$$

with the following boundary conditions

$$\frac{dy_i}{d\xi} = 0 \quad \text{for} \quad \xi = 0 \tag{4.26}$$

$$y_i = y_{i,s} \quad \text{for} \quad \xi = 1 \tag{4.27}$$

These equations are calculated only for H_2, CO, H_2O and CO_2, as they are the only components that directly affect the effectiveness factor values. The remaining chemical species are taken into account with an inert component, required for the sum of the molar fractions inside the pellet to be equal to one:

$$y_{inert} = 1 - y_{H_2} - y_{CO} - y_{H_2O} - y_{CO_2} \tag{4.28}$$

This PDAE system of mass balances is discretized in an algebraic system through orthogonal collocation on finite elements. The new system of equations to be solved requires initial guess points for the molar fractions as close as possible to their correct values. In order to facilitate the convergence of the system, a continuation method is used: an ODE solver integrates the internal mass balances for a limited period of time, and the obtained results are used as initial guesses for the algebraic system. In this way the solution of the dynamic equations provides values close to the steady state conditions, which are therefore more easily evaluated by the implemented algorithm.

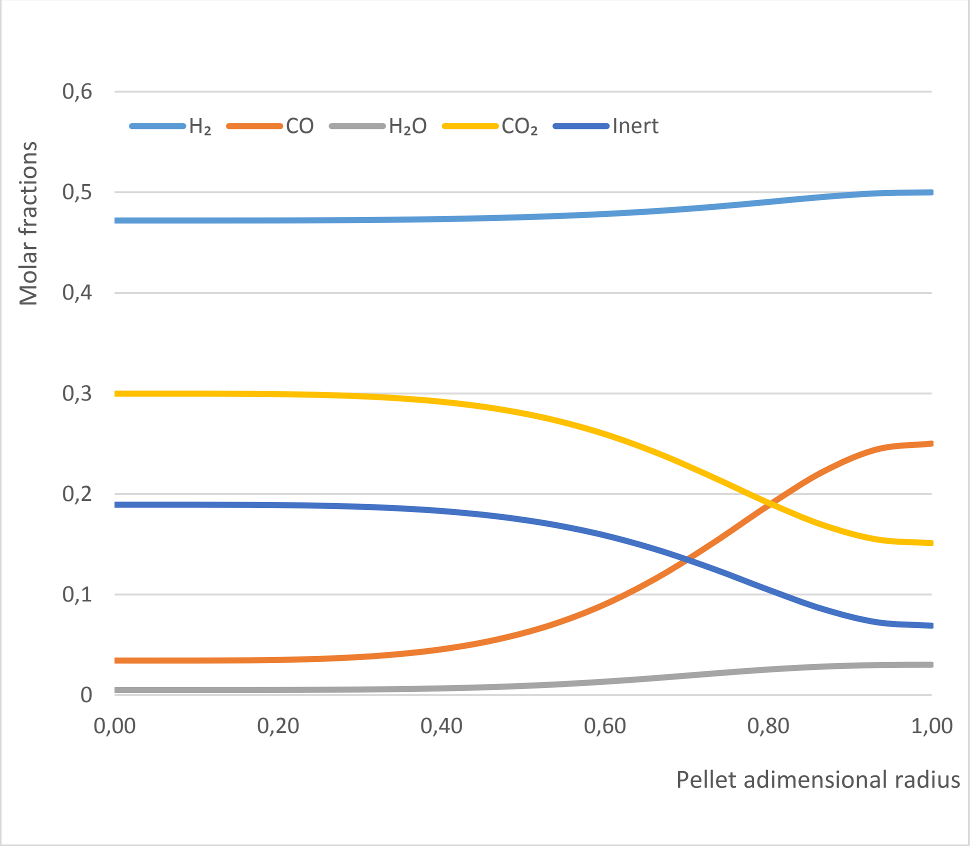

Figure 4.3 - Concentration profiles of the reacting components inside the catalytic pellet

The algebraic system, after reaching convergence, provides the concentration profiles for all the components considered inside the pellet as shown in Figure 4.3. The effectiveness factors, needed to obtain the effective reaction rates of the reactor model, are finally calculated with the following expression:

$$\eta_j = 3\frac{\int_0^1 r_j\left(y_i\right)\cdot\xi^2 d\xi}{r_j\left(y_{i,s}\right)} \tag{4.29}$$

4.4 Vapour-liquid equilibrium

The FTS reaction produces heavy hydrocarbons that, by increasing in chain length and quantity, could form a liquid phase if the reactor temperature reaches the dew point of the mixture. To evaluate this possibility a flash calculation is carried out to find the dew point temperature and, in the case its value is higher than the reactor temperature, to provide the liquid and vapour phase flow rates and compositions.

For the vapour-liquid equilibrium (VLE) calculation is assumed that the resistance to mass transport caused by the liquid film formed on the pellet surface is much lower than the intraporous resistances inside the catalyst, therefore making unnecessary the use of a trickle bed reactor model.

Observing the flash separator in Figure 4.4, the flow F with composition $\boldsymbol{z}$ splits in a vapour phase V and a liquid phase L, whose compositions are respectively $\boldsymbol{y}$ and $\boldsymbol{x}$; the condensation of the L phase releases the heat flow $\dot{Q}$. The mass balance for each component inside the flash separator can therefore be written as:

$$Fz_i = Vy_i + Lx_i \tag{4.30}$$

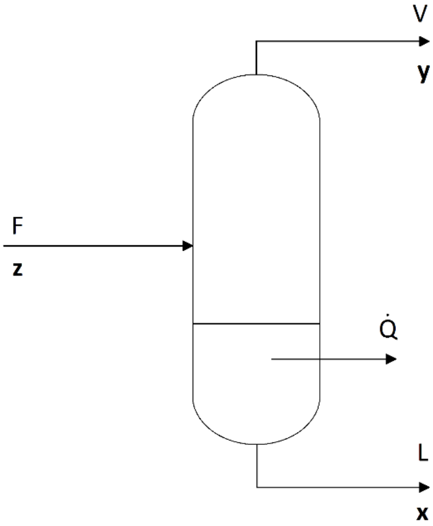

Figure 4.4 - Flash separator

The liquid and vapour phases, being in equilibrium between them, provide an additional set of equations to be respected:

$$\bar{f}_i^V\left(T,P,\mathbf{y}\right)=\bar{f}_i^L\left(T,P,\mathbf{x}\right) \tag{4.31}$$

where $\bar{f}_i$ is the vapour or liquid fugacity of the i^{th} component. The fugacities can be expressed as the product between the fugacity coefficient and the fugacity of the component in a mixture of ideal gases, which is equal to its partial pressure:

$$\bar{f}_i\left(T,P,\mathbf{z}\right)=\bar{\phi}_i\left(T,P,\mathbf{z}\right)\cdot\bar{f}_i^*\left(T,P,\mathbf{z}\right)=\bar{\phi}_i\left(T,P,\mathbf{z}\right)\cdot Pz_i \tag{4.32}$$

The formula (4.31) can then be rearranged as:

$$y_i=\frac{\bar{\phi}_i^L\left(T,P,\mathbf{x}\right)}{\bar{\phi}_i^V\left(T,P,\mathbf{y}\right)}x_i=k_i\cdot x_i \tag{4.33}$$

The fugacity coefficients are calculated solving Peng-Robinson equation of state (EoS), as done by Marano and Holder [52]. The binary coefficients, necessary for the mixing rule equations of the EoS parameters, are taken from the Aspen HYSYS database.

The heat flow $\dot{Q}$ can be directly obtained from the energy balance:

$$Fh_F=Vh_V+Lh_L+\dot{Q} \tag{4.34}$$

Using the global mass balance $F=L+V$ and introducing the vapour to feed ratio $\beta=V/F$, equations (4.30) and (4.33) can rewritten as:

$$x_i=\frac{z_i}{1+\beta\left(k_i-1\right)} \tag{4.35}$$

$$y_i=\frac{k_i\cdot z_i}{1+\beta\left(k_i-1\right)} \tag{4.36}$$

These expressions are inserted in the constitutive relations $\sum_{i=1}^{N_{comp}}y_i-\sum_{i=1}^{N_{comp}}x_i=0$, obtaining the Rachford and Rice equation:

$$\sum_{i=1}^{N_{comp}} \frac{z_i\left(k_i-1\right)}{1+\beta\left(k_i-1\right)}=0 \tag{4.37}$$

At this point, after deriving all the necessary equations, it is possible to solve the flash calculation by following these steps:

1. Assume the $\boldsymbol{x}$ and $\boldsymbol{y}$ phase compositions.
2. Solve the EoS equation to derive the equilibrium constants $\boldsymbol{k}$.
3. Solve Rachford and Rice equation to derive β.
4. Assume new $\boldsymbol{x}$ and $\boldsymbol{y}$ values and return to (2) until $\| \boldsymbol{x}_{NEW} - \boldsymbol{x} \|, \| \boldsymbol{y}_{NEW} - \boldsymbol{y} \| < \varepsilon$.
5. Solve the energy balance to obtain $\dot{Q}$.

Unfortunately, dealing with a non-ideal system, this method may not converge to the correct solution if a proper initial guess for the phase compositions is not chosen.

For this reason, the more robust method described in the work by Boston and Britt is implemented [61]. The Inside-Out algorithm they propose replaces the previous set of variables with a new one, which is weakly dependent on temperature and phase compositions.

The algorithm reaches the convergence using two nested loops: the main variables of the outer iteration loop are referred to as “volatility parameters” and are defined as:

$$u_i=\ln\left(\frac{k_i}{k_b}\right) \tag{4.38}$$

where k_b is a reference equilibrium ratio defined as a weighted average of the form:

$$\ln\left(k_b\right)=\sum_{i=1}^{N_{comp}} w_i \cdot \ln\left(k_i\right) \tag{4.39}$$

where the w_i are weighting factors, whose expressions are derived in Appendix B. The variables of the inner loop are:

$$R=\frac{k_b \cdot V}{k_b \cdot V+k_b^0 \cdot L} \tag{4.40}$$

$$p_i = \frac{L \cdot x_i}{1-R} \tag{4.41}$$

The variable R, like β, has values ranging from 0 to 1, which correspond respectively to the bubble and dew point of the system. k_b^0 is a reference value which is set equal to k_b at the beginning of the R loop, and held constant until convergence is achieved.

The VLE balances of the typical flash solution are then rewritten with the new set of variables, as shown in more detail in Appendix B. The solving steps of the Boston and Britt algorithm for a flash with known temperature and pressure conditions, as in our case, are here reported:

1. Assume $\boldsymbol{u}$, setting $k_b = 1$ and using Raoult's law or Wilson's formula, that do not depend on phase composition:

$$\ln(k_i) = \frac{P_{C,i}}{P} \exp\left(5.37\left(1+\omega_{Pitzer,i}\right)\left(1-\frac{T_{C,i}}{T}\right)\right) \tag{4.42}$$

2. Assume R $\left(0 < R < 1\right)$.
3. Calculate $\boldsymbol{p}, k_b, L, V$.
4. Assume a new R and return to (2) until $|R_{NEW} - R| < \varepsilon$.
5. Calculate $\boldsymbol{x}, \boldsymbol{y}$.
6. Solve Peng-Robinson EoS and obtain the equilibrium constants $\boldsymbol{k}$.
7. Assume new $\boldsymbol{u}$ and return to (2) until $\|\boldsymbol{u}_{NEW} - \boldsymbol{u}\| < \varepsilon$.
8. Solve the energy balance to obtain $\dot{Q}$.

This flash calculation is carried out only if the dew point temperature of the mixture is higher than the reactor temperature. The steps required to calculate the dew point temperature using the Boston and Britt algorithm are:

1. Assume T_{dew}.
2. Calculate $\boldsymbol{k}$ at T_{dew} and T' using Raoult's law or equation (4.42).
3. Evaluate k_b at T_{dew} and T' using equation (4.39).
4. Assume $\boldsymbol{u}$, A and B (expressions reported in Appendix B).

5. Set $L=0$ and $R=1$.
6. Calculate $\boldsymbol{p}$ and k_b.
7. Obtain a new T_{dew} from the k_b model.
8. Calculate $\boldsymbol{x}, \boldsymbol{y}$.
9. Solve Peng-Robinson EoS at T_{dew} and T' and obtain the equilibrium constants $\boldsymbol{k}$ at both temperatures.
10. Calculate a new k_b with the new constants.
11. Assume new $\boldsymbol{u}$, A, B and return to (6) until $\|\boldsymbol{u}_{NEW}-\boldsymbol{u}\|<\varepsilon$, $|A_{NEW}-A|<\varepsilon$ and $|B_{NEW}-B|<\varepsilon$.

The new procedure proposed by Boston and Britt, as seen, does not require an initial guess for the composition of the vapour and liquid phases, therefore reaching convergence in a robust and efficient way.

5 Industrial plant economic optimization

Having described the industrial reactor model in the previous chapter, it is now possible to use said model in a Fischer-Tropsch plant-wide simulation.

A GTL facility has been simulated using the Aspen HYSYS software, modelling both the syngas production and the FT process sections (with MATLAB still handling the FT reactor simulation).

Finally, MATLAB is used to maximise the plant profits through a FT reactor sizing and staging optimization.

5.1 MATLAB and HYSYS connection

MATLAB® R2014a is used as an activeX controller for Aspen HYSYS® Version 8.4, so that the two programs can communicate with each other and exchange the data needed to perform the profit maximization of the FT plant.

The hydrocarbon lumps are modelled as hypothetical components within the HYSYS environment; their properties are derived with the asymptotic behaviour correlations proposed by Marano and Holder [54-56]. Unfortunately, HYSYS cannot handle components with a changing molecular weight; for this reason, the lumps model is modified to follow the approach outlined by Hillestad [62].

In this model, each lump distribution is represented by two apparent constant α values, denoted α_L and α_H , in addition to the relative distribution between them, ϕ . The FT reaction is so rearranged:

$$CO+U_{H_2}H_2 \xrightarrow{r_{FT}} \ldots+\nu_{lump}(\alpha)\cdot C_{lump}(\alpha)+\ldots \qquad (5.1)$$

$$CO+U_{H_2}H_2 \xrightarrow{r_{FT}} \ldots+\phi\cdot\nu_{lump,L}(\alpha_L)\cdot C_{lump,L}(\alpha_L)+(1-\phi)\cdot\nu_{lump,H}(\alpha_H)\cdot C_{lump,H}(\alpha_H)+\ldots \qquad (5.2)$$

With the three introduced parameters is possible to reconstruct the distribution of the original lump (with a varying α) using two apparent lumps with constant chain growth probabilities:

$$\nu_{lump}\cdot M_{lump}=\phi\cdot\nu_{lump,L}\cdot M_{lump,L}+(1-\phi)\cdot\nu_{lump.H}\cdot M_{lump,H} \qquad (5.3)$$

This substitution, as described above, is only applicable to the C_{11+} lump, since its $\nu_{lump}\cdot M_{lump}$ function values (where the ν_{lump} and M_{lump} expressions are respectively given by equations (4.3) and (4.6) with $i=11$ and $j=\infty$) are monotonically increasing between the chosen α_L and α_H (respectively equal to 0.55 and 0.9) as shown in Figure 5.1:

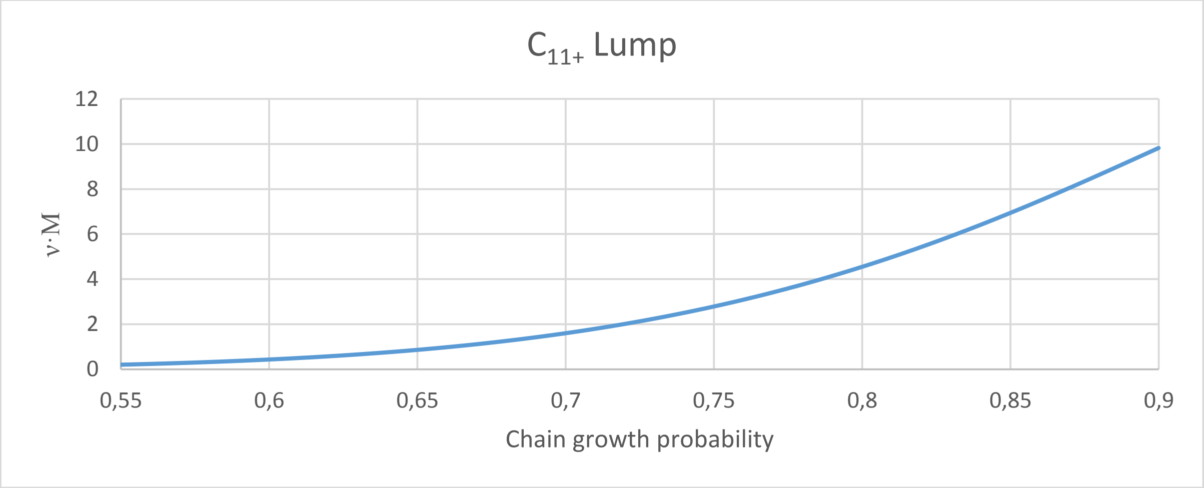

Figure 5.1 - C_{11+} lump function

Conversely the $\nu_{lump}\cdot M_{lump}$ function for the $C_{5\text{-}10}$ lump (where the ν_{lump} and M_{lump} expressions are respectively given by equations (4.2) and (4.6) with $i=5$ and $j=10$) has a maximum between its lower α_L and upper α_H bounds, as can be seen in Figure 5.2:

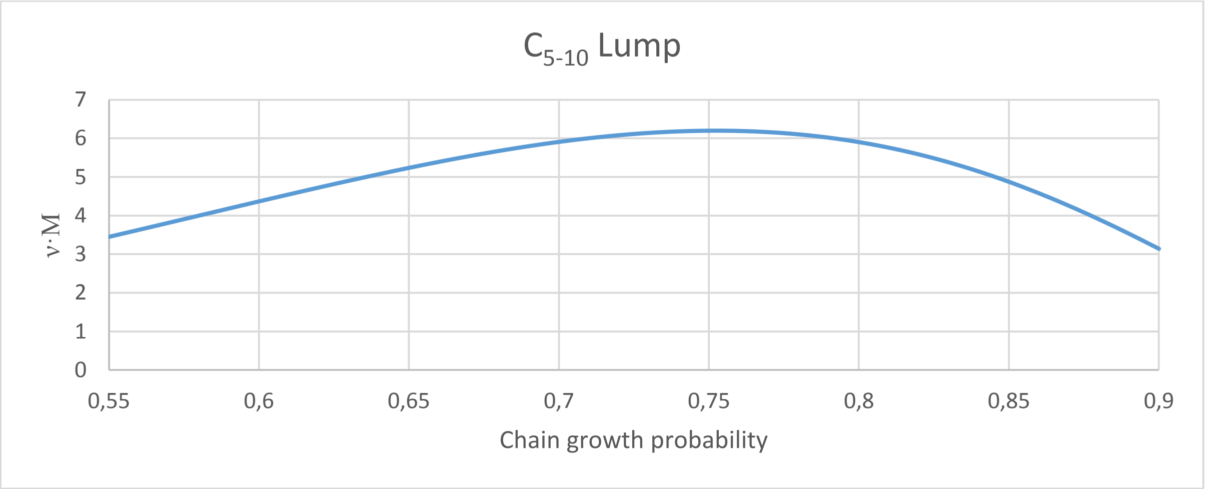

Figure 5.2 - $C_{5\text{-}10}$ lump function

It is therefore necessary to introduce another α_M value (approximately equal to 0.752471 in this work) corresponding to the function maximum. The $C_{5\text{-}10}$ lump is now split in three apparent lumps with constant chain growth probabilities α_L, α_M and α_H :

- If $\alpha < \alpha_M$ the $C_{5\text{-}10}$ lump is so divided:

$$\nu_{C_{5-10}} \cdot M_{C_{5-10}} = \phi \cdot \nu_{C_{5-10},L} \cdot M_{C_{5-10},L} + (1-\phi) \cdot \nu_{C_{5-10},\mathrm{M}} \cdot M_{C_{5-10},\mathrm{M}} \tag{5.4}$$

- If $\alpha > \alpha_M$ the $C_{5\text{-}10}$ lump is so divided:

$$\nu_{C_{5-10}} \cdot M_{C_{5-10}} = \phi \cdot \nu_{C_{5-10},\mathrm{M}} \cdot M_{C_{5-10},\mathrm{M}} + (1-\phi) \cdot \nu_{C_{5-10},\mathrm{L}} \cdot M_{C_{5-10},\mathrm{L}} \tag{5.5}$$

- If $\alpha = \alpha_M$ the $C_{5\text{-}10}$ lump is simply replaced with the middle apparent lump:

$$\nu_{C_{5-10}} \cdot M_{C_{5-10}} = \nu_{C_{5-10},\mathrm{M}} \cdot M_{C_{5-10},\mathrm{M}} \tag{5.6}$$

The so obtained apparent lumps, having a constant α and molecular weight, can therefore be handled by HYSYS without any problem.

5.2 Syngas plant section

The first section of the GTL plant takes care of the conversion of the natural gas to syngas. The process configuration considered uses a combination of steam methane reforming (SMR) and autothermal reforming reactors, as proposed by Baltrusaitis and Luyben in their work [63]. The process diagram, as simulated in Aspen HYSYS, is reported in Figure 5.3.

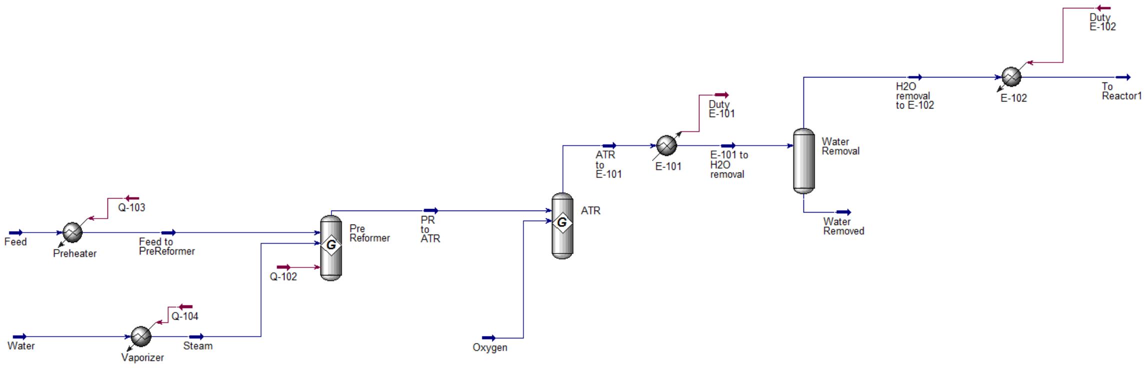
Duty
E-102
H2O
removal
to E-102
E-102
To
Reactor1
Duty
E-101
ATR
to
E-101
E-101
E-101 to
H2O
removal
Water
Removal
Water
Removed
ATR
Q-103
Feed
Preheater
Feed to
PreReformer
Pre
Reformer
PR
to
ATR
Q-102
Q-104
Water
Vaporizer
Steam
Oxygen

Figure 5.3 - Syngas plant section

Both the SMR and ATR reactors are assumed to achieve chemical equilibrium. The HYSYS Gibbs reactor model is therefore used for these two reactors. The SMR reactor is fed with 8195 kmol/h of natural gas and a small amount of water. The reactions occur in the catalyst-filled tubes in the reactor, which is heated by burning fuel with air:

- Hydrocarbon steam reforming:

$$C_nH_m + nH_2O \rightleftarrows nCO + \left(\frac{m}{2} + n\right)H_2 \tag{5.7}$$

- Water-gas shift reaction:

$$CO + H_2O \rightleftarrows CO_2 + H_2 \tag{5.8}$$

The outlet feed, partially converted to syngas, is sent to the ATR reactor, into which also oxygen is fed. Inside the reactor the exothermic heat of partial oxidation of the hydrocarbons provides the required endothermic heat for the reforming reaction:

- Hydrocarbon steam reforming:

$$C_nH_m + nH_2O \rightleftarrows nCO + \left(\frac{m}{2} + n\right)H_2 \tag{5.9}$$

- Water-gas shift reaction:

$$CO + H_2O \rightleftarrows CO_2 + H_2 \tag{5.10}$$

- Hydrocarbon partial oxidation:

$$C_nH_m + \frac{2n+m}{4}O_2 \longrightarrow nCO + \frac{m}{2}H_2O \tag{5.11}$$

The hot syngas feed obtained from the ATR reactor is first cooled to 30°C and then sent to a separator drum, to remove the liquid water which would otherwise slow down the FT reaction rate in the next plant section. Finally, the syngas flow, after being heated to 240°C, is sent to the first FT reactor.

5.3 Fischer-Tropsch plant section

At this point the syngas feed properties, like temperature, pressure, flow rate and composition, are passed to MATLAB, which solves the reactor model explained in chapter 4. At the end of the calculation the feed properties at the reactor outlet are returned to the simulation in Aspen HYSYS. Here, the outlet flow is cooled to 30°C and sent to a 3-phase separator as seen in Figure 5.4.

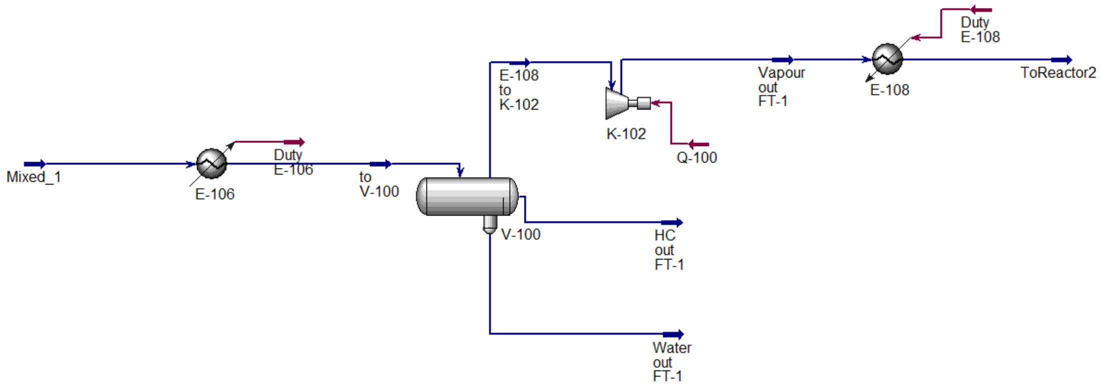
Duty
E-108
E-108
to
K-102
Vapour
out
FT-1
E-108
ToReactor2
K-102
Q-100
Mixed_1
Duty
E-106
E-106
to
V-100
V-100
HC
out
FT-1
Water
out
FT-1

Figure 5.4 - Fischer-Tropsch plant section

The water is therefore removed from the heavy hydrocarbon products, while the remaining reactants and products in gas phase are sent to the next reactor. Before entering it, the gas feed temperature and pressure are raised to the same values of the first reactor inlet to have appropriate reaction conditions for the FTS.

5.4 Profitability analysis

The economic analysis of the GTL plant requires first of all the evaluation of two different cost categories:

- Capital expenses (CAPEX), which include funds to eventually purchase land, design and purchase equipment, structures and buildings as well as to bring the facility into operation [64].
- Operating expenses (OPEX), which include the day-to-day expenditures required for the manufacturing of a product, like the purchasing of raw material and utilities, as well as the general overhead costs.

5.4.1 Capital expenses

The equipment costs of the first section of the plant, dedicated to the production of syngas, are taken from the economic study done by Baltrusaitis and Luyben [63]; tabulated information on equipment costs is provided in Appendix C.

The Fischer-Tropsch section of the plant is instead analysed in greater detail, using information by Guthrie [65, 66], Ulrich [67] and Navarrete [68], as described by Turton et al. [69].

Firstly, the purchase cost of each piece of equipment is calculated at base conditions, i.e. equipment made of the most common material, usually carbon steel, and operating at ambient pressures:

$$\log_{10}\left(C_p^0\right) = K_1 + K_2 \log_{10}\left(A\right) + K_3\left(\log_{10}\left(A\right)\right)^2 \tag{5.12}$$

where A is the capacity or size parameter for the equipment and the values of K depend on the type of equipment considered. The bare module cost is then obtained, correcting the base purchase cost C_p^0 with the F_M and F_P factors, which respectively account for the effective material of construction (MOC) and operating pressure:

$$C_{BM} = C_p^0\left(B_1 + B_2 \cdot F_M \cdot F_P\right) \tag{5.13}$$

where the values of B depend on the type of equipment considered. The bare module cost incorporates both the direct expenses, related to the purchase and installation of equipment, and indirect expenses, i.e. insurance, transport, taxes, construction overhead and contractor engineering expenses. All the parameter values and equations needed to calculate the bare module cost of each piece of equipment are reported in Appendix C.

The purchased costs for these types of equipment, obtained in 2003, have been normalized to 2001. These estimates are updated to 2015 by using the Chemical Engineering Plant Cost Index (CEPCI) [70]:

$$Cost_{2015} = Cost_{2001}\left(\frac{CEPCI_{2015}}{CEPCI_{2001}}\right) \tag{5.14}$$

The total module cost, which refers to the cost of making small to moderate expansions or alterations to an existing facility, is then calculated. Values of 15% and 3% of the bare module cost are assumed for contingency costs and fees respectively, increasing the overall cost by 18%:

$$C_{TM} = 1.18 \sum_{i=1}^{N_{equipment}} C_{BM,i} \tag{5.15}$$

Finally, the grassroots cost, that refers to a completely new facility in which the construction is started on essentially underdeveloped land, is evaluated. This correction is usually assumed to be equal to 50% of the bare module cost for the base conditions, i.e. $F_M = F_P = 1$:

$$C_{GR} = C_{TM} + 0.50 \sum_{i=1}^{N_{equipment}} C^0_{BM,i} \tag{5.16}$$

5.4.2 Operating expenses

There are many elements that affect the manufacturing-operating cost of chemicals production; they can be grouped into three categories:

- Direct costs, which include raw material and utilities expenses.
- Fixed costs, like depreciation, taxes, insurance and plant overhead costs.
- General expenses, consisting of costs for administration and research activities.

In this thesis only the direct costs are considered, being usually the biggest expense for a chemical plant. The raw materials and utilities costs used in this analysis are reported respectively in Table 5.1 and Table 5.2.

Table 5.1 - Utilities costs

Utility	**Cost [69]**	**Unit of measure**
Cooling water	0.354	\$/GJ
HP steam	17.7	\$/GJ
Electricity	16.8	\$/GJ

Table 5.2 - Raw materials costs

Raw material	Cost	Unit of measure
Oxygen	35 [71]	\$/ton
Natural gas	112.3 [72]	\$/m^3

5.4.3 Revenues

The hydrocarbons produced from the FTS reaction represent the primary source of profit of the industrial plant. The prices for the hydrocarbon are obtained by averaging their values on the Rotterdam market for years 2013 and 2014, as reported in the OPEC Annual Bulletin 2015 [73]. A price for the tail gas, mainly composed by syngas and carbon dioxide, is also considered, since this stream can be burnt to produce electricity or steam. The products prices are shown in Table 5.3.

Table 5.3 - Products costs

Product	Price	Unit of measure
Tail gas	1.4 [74]	\$/ton
LPG (C_3-C_4)	80 [75]	\$/bbl
Gasoline (C_{5-10})	115.532 [73]	\$/bbl
Gasoil 20 ppm (C_{11-20})	116.646 [73]	\$/bbl
Fuel oil (C_{21+})	89.048 [73]	\$/bbl

5.4.4 Net Present Value

After estimating the values of the CAPEX, OPEX and revenues, the cash flow analysis is now presented. The cash flow diagram reported in Figure 5.5 describes the relationships between revenue, cash operating expenses, depreciation and profit, necessary to calculate the annual cash flows:

$$CF_i = (R - C - D)(1 - t) + D \tag{5.17}$$

where R is the revenue, C the cash operating expenses, D the depreciation, t the tax-rate and CF_i the after-tax cash flow for year i. The following assumptions are also made:

- Tax-rate equal to 40%.
- A plant life of 20 years, with a null salvage value at the end of this period.
- A straight line depreciation using the half-year convention, for a recovery time of 10 years.
- Working capital estimated at 20% of the grassroots cost.

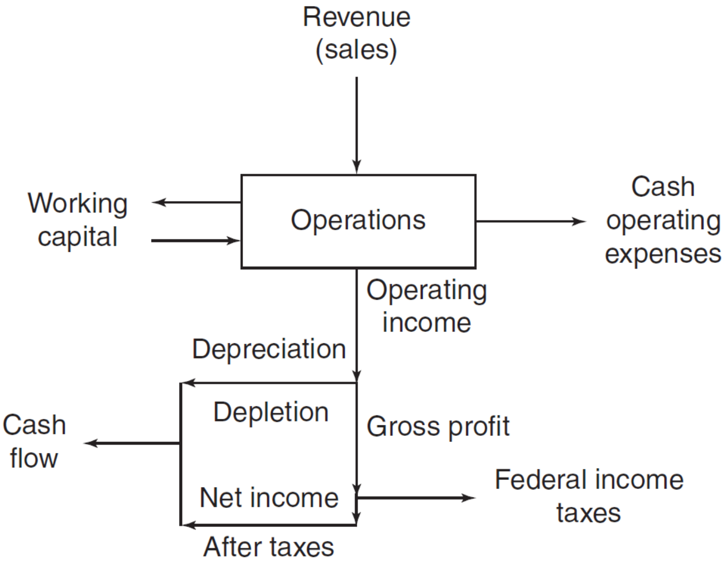
Revenue
(sales)
Working
capital
Operations
Cash
operating
expenses
Operating
income
Depreciation
Depletion
Cash
flow
Gross profit
Net income
Federal income
taxes
After taxes

Figure 5.5 - Cash flow model [57]

With the calculated CF_i values it is then possible to evaluate the Net Present Value (NPV) of the investment, which is the maximized parameter in the plant optimization study. The NPV method is used by many companies, as it reflects properly the time value of money and its effect on profitability. The equation for the NPV is:

$$NPV = \sum_{i=1}^{N_{years}} \frac{CF_i}{(1+d_R)^i} - CF_0 \tag{5.18}$$

where d_R is the discount rate, assumed in this case equal to 10%, and CF_0 is the cash flow at year 0, given by the sum of the initial investment and the working capital; each $CF_i/(1+d_R)^i$ term is the discounted cash flow (DCF) for year i, i.e. the present value of future cash flow CF_i discounted by d_R. When the NPV is calculated with equation (5.18), if the result is positive, the venture will earn more than the interest (discount) rate used; conversely, if the NPV is negative, the venture earns less than the rate.

5.5 Economic optimization

For this thesis, it is decided to maximize the NPV formula as a function of the FT reactors sizes for four different plant configurations (from 1 to 4 reactor stages). The size of each multi-tubular reactor depends on the number N_T and length L_T of the tubes of which the reactor is composed, but does not depend on the tubes diameter D_T, that here is set constant to 0.025 m. To reduce the number of variables of the optimization problem and to avoid operating the reactor with unrealistic flow rates values inside the tubes, it is decided to set the gas velocity v_{GAS} to 0.5 m/s at the entrance of each reactor:

$$N_{T,i} = \frac{\dot{V}_{IN,i}}{\left(\frac{\pi D_T^2}{4} \cdot v_{GAS} \left(= 0.5 \quad {}^{m}\!/_{s}\right)\right)} \tag{5.19}$$

where $\dot{V}_{IN,i}$ is the volumetric flow rate at the inlet of reactor i. According to these decisions, the maximization of the NPV value will then depend only on the length $L_{T,i}$ of each reactor stage considered.

The general structure of the optimization conducted with MATLAB and Aspen HYSYS for the four plant configurations is shown in Figure 5.6.

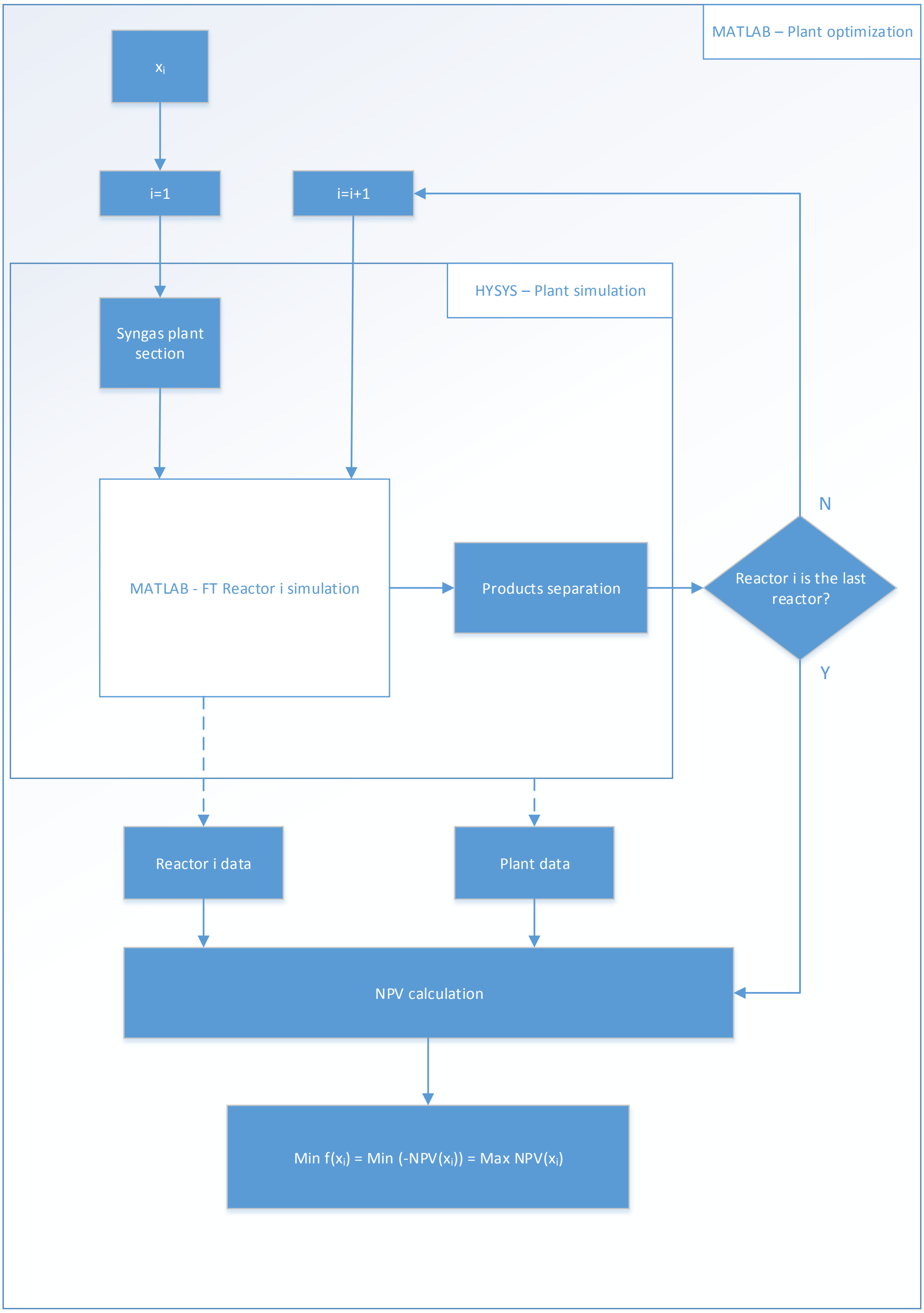
MATLAB – Plant optimization
x_i
i=1
i=i+1
HYSYS – Plant simulation
Syngas plant section
MATLAB - FT Reactor i simulation
Products separation
N
Reactor i is the last reactor?
Y
Reactor i data
Plant data
NPV calculation
Min f(x_i) = Min (-NPV(x_i)) = Max NPV(x_i)

Figure 5.6 - Optimization flow diagram

Within the MATLAB environment the fmincon nonlinear programming solver is used to find the minimum of the following minimization problem:

$$\begin{aligned} &\min_{x} f(\boldsymbol{x}) = \min_{x}\left(-NPV(\boldsymbol{x})\right) = \max_{x} NPV(\boldsymbol{x}) \\ &lb < \boldsymbol{x} < ub \end{aligned} \tag{5.20}$$

where $\boldsymbol{x}$ is the vector composed of the values of the reactor lengths $L_{T,i}$, while lb and ub are the set of lower and upper bounds on the design variables $\boldsymbol{x}$. The fmincon solver tries to find a minimizer $\boldsymbol{x}$ of the function $f(\boldsymbol{x})$, so that the solution is always in the range $lb < \boldsymbol{x} < ub$. For each set of reactor lengths that the solver assigns to the solution vector $\boldsymbol{x}$, the program written in MATLAB calculates the NPV value for that given plant configuration as seen in Figure 5.6 through the following steps:

1. The simulation of the syngas plant section in Aspen HYSYS provides the temperature, pressure, flow rate and feed composition at the inlet of the first FT reactor.
2. This information is passed to the FT reactor simulation in MATLAB which integrates the equations of the industrial model along the reactor length $x_i = L_{T,\mathrm{i}}$ and therefore calculates the outlet flow properties.
3. These flow properties are communicated to HYSYS which, through a separation stage, separates the heavier hydrocarbon products from the water and from the residual gas phase.
4. At this point, if there are other reactor stages, the residual gas phase is used as feed for the next reactor, returning to step (2); otherwise, the plant simulation ends.
5. The main program in the MATLAB environment finally calculates the NPV value, using the data provided by the plant simulation in HYSYS and the reactors simulations in MATLAB.

Unfortunately, the optimization problem formulated in this way has two major problems:

- The calculation of the pellet effectiveness factors (described in section 4.3) is relatively slow, so that the overall optimization time is too long with the available calculation tools.

- The solution found for the optimization is sensitive to the initial guess point $\boldsymbol{x}_0$ provided to the solver, so that it is not possible to know if a global minimum of the $f(\boldsymbol{x})$ function has truly been reached.

These issues are addressed in the following two subsections.

5.5.1 Calculation of the catalyst effectiveness factor

To speed up the optimization code, it is decided to write a separate MATLAB program which solves the catalyst pellet model for various combinations of compositions ($y_{H_2}, y_{CO}, y_{H_2O}, y_{CO_2}, y_{inert}$), temperatures and pressures. The effectiveness factors of the FT and WGS reactions thus calculated are therefore collected in a multidimensional array, which is used in the main optimization program.

In this way, every time that during the optimization process the effectiveness factors should be calculated, their values are instead quickly interpolated from the previously obtained effectiveness factors gathered in the multidimensional array. The procedure followed to create the multidimensional arrays can be found in Appendix D.

5.5.2 GlobalSearch algorithm

The global minimum of the $f(\boldsymbol{x})$ function can be found by using the GlobalSearch algorithm available in the Global Optimization Toolbox of MATLAB. This algorithm starts the local solver (fmincon) from a variety of start points, which are used to sample multiple basins of attraction. Analysing the objective function values and basins of attractions found, GlobalSearch therefore provides the desired global minimum of the objective function.

5.6 Results and discussion

The results of the economic optimization of the four plant configurations considered are shown in Table 5.4, with the three stages configuration being the most profitable. It can be seen that the CAPEX, OPEX and revenues values, all factors involved in the calculation of the NPV, increase with the number of reactor stages used in each plant configuration.

The CAPEX value increases approximately by the same amount for each stage added to the plant; it should be noted that each stage carries with it not only the cost of an extra FT reactor, but also the additional costs of a cooler, a 3-phase separator, a compressor and a heater, needed to collect the reaction products and send the gas stream to the next reactor stage.

The OPEX values follow the same upward trend of the capital expenses, due to the utilities costs associated with the equipment of each additional stage; furthermore, no energetic optimization is performed, leading to the worst situation for the evaluation of the utilities costs.

On the contrary the revenues, while still growing with the number of stages considered, tend to increase by a lower amount for each additional FT reactor. This decline in the growth of the revenues explains why the configuration with three stages has a higher NPV, and so it is more profitable, than the configuration with four stages, that fails to cover its additional capital and operating expenses with the increase in profits.

The gains in revenues from one to two and two to three reactors on the other hand are sufficient to cover the new expenses, leading to progressively increase the NPV for each additional stage. This proves that, for this simulation, the staging of the FT reactor is economically advantageous thanks to:

- The removal between one stage and the next of the reaction products, that otherwise would slow down the FTS reaction.
- The recompression of the gas stream before each reactor, to avoid low pressures that would decrease the chain growth probability value α and so shift the reaction selectivity to the less profitable lighter products.

In Table 5.4 the profitability index (PI) for each plant configuration are also reported. The PI attempts to identify the relationship between the costs and benefits of a proposed project and its formula is calculated as:

$$PI = \frac{\text{Present Value of future CFs}}{\text{Initial investment}} \tag{5.21}$$

where the sum of the cash flows does not include the initial investment; a project is therefore economically profitable if the value of PI is greater than 1. In this case, the configuration with two reactor stages is the best one according to the PI value. This fact may lead potential investors to prefer the two reactors configuration that, although having a 7.1% lower NPV than the three reactor configuration, has an 8.7% higher PI, therefore creating a greater amount of value per unit of investment.

Table 5.4 - Profitability analysis results of the four plant configurations

	CAPEX [M$]	OPEX [M$/year]	Revenues [M$/year]	NPV [M$]	Profitability Index
1	258.51	64.14	174.02	319.37	2.24
2	311.11	68.95	202.25	389.78	2.25
3	391.22	73.44	227.22	419.48	2.07
4	451.73	76.89	235.75	388.85	1.86

The cumulative sums of the discounted cash flows for the four plant configurations are shown in Figure 5.7. Prior to time zero, expenditures are made for the fixed capital investment and working capital. From that moment, start-up occurs and the production begins. The slopes of the lines representing the sum of the DCFs decrease over the years due to:

- The $(1+d_R)^i$ factor in the NPV formula (5.18) which progressively decreases the future cash flows.
- The full recovery of the initial investment with depreciation after 11 years (straight line depreciation using the half-year convention for 10 years).

Instead, at the end of the project life, the slopes increase due to the recovery of the working capital (while the salvage value has been previously assumed equal to zero).

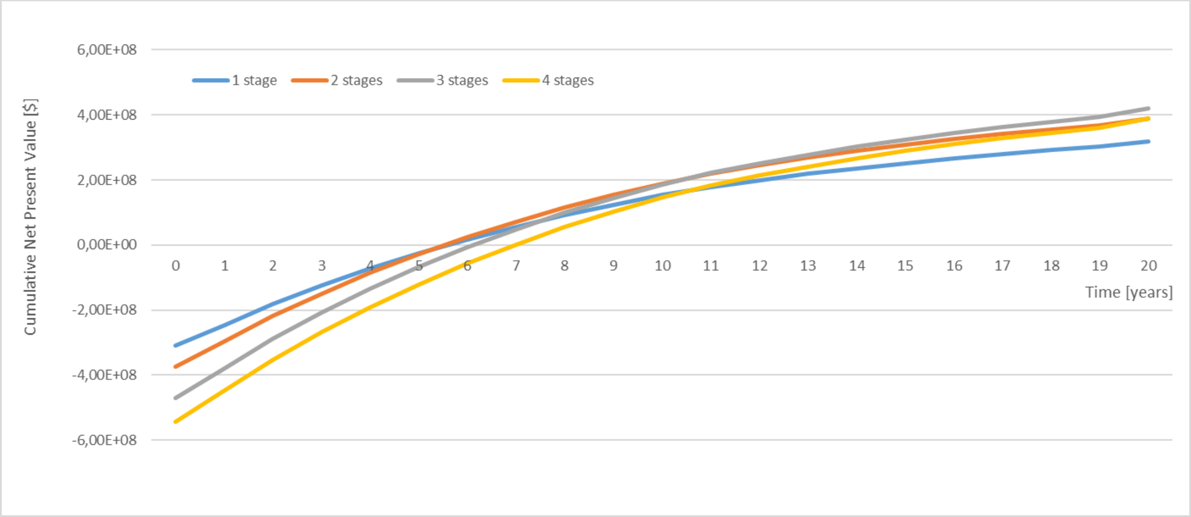

Figure 5.7 - Cumulative sums of the discounted cash flows for the four plant configurations considered

It should be noted that originally the plant configuration included two recycles as optimization variables. The outlet gas flow of the last 3-way separator was split into three flows, i.e. a tail gas stream and the two recycle streams; one recycle was sent to the first FT reactor inlet while the other was sent to the steam methane reformer. Anyway these recycles were eventually discarded since:

- The convergence time required for each plant configuration was relatively too high, leading to unacceptable optimization times.
- The recycles composition presented a H_2/CO ratio greater than 3, which would have probably worsened the hydrocarbon production in any case.

6 Conclusions

The main objectives treated in this thesis have been the kinetic model discrimination for a new Fischer-Tropsch iron catalyst and the profit maximization of a Gas-to-Liquids project by optimizing the size and number of stages of the Fischer-Tropsch reactor used in the industrial plant.

Experimental tests were performed by the Università degli Studi di Milano for their new iron based FT catalyst and it was therefore possible to obtain the data necessary for the kinetic model discrimination. Firstly, a simple plug-flow reactor was modelled in MATLAB for the pilot plant and used to process the experimental results obtained in the laboratory. Various kinetic models have been then taken into account from the literature to simulate the FT and WGS reaction rates of the studied catalyst; the kinetic parameters of the considered models were also regressed so that the simulated results could better fit the experimental data. The discrimination criterion chosen to determine the best reactions model set was the mean squared error between the actual observations and the observation values predicted by the reactor simulation. The model proposed by Zimmerman and Bukur [51], with regressed kinetic constants, has proven to be the best one to fit the experimental data. The mass fractions of the main components (i.e. H_2, CO, H_2O and CO_2) are predicted quite well, while the Anderson-Schulz-Flory distribution tends to overestimate the production of heavier hydrocarbons; this deviation is probably due to the lower mass fractions in play for these components compared to the other ones, therefore affecting less the MSE final value.

The selected kinetic model could be further improved with additional experimental runs, which would provide data for different operating conditions not previously analysed. It should also be noted that the program code written in MATLAB could be modified to perform kinetic model discriminations for different FT catalysts tested in the future with the same (or a similar) pilot plant.

The second part of this thesis has dealt instead with the economic evaluation of a GTL plant project. The FT industrial reactor used within the GTL plant was simulated in MATLAB with a more complex model than the one used for the pilot laboratory plant. In this case the reactor considered was a multi-tubular fixed bed reactor which used the iron catalyst and corresponding kinetic model studied in the first part of this thesis. In particular, in order to obtain a more realistic and accurate reactor model, the diffusion resistances within the catalyst pellet and the possible formation of a liquid phase of heavy hydrocarbon products have been taken into account along all the reactor length. The FT reactor model thus obtained was then connected to a GTL plant model, developed instead in Aspen HYSYS. The GTL model simulated both the production of the syngas fed to the FTS process and the separation stages after each FT reactor, where the heavier hydrocarbon products were separated from the water and from the residual gas phase.

At this point, the sizing and staging optimization of the FT reactor was finally performed with MATLAB, having as objective the maximization of the net present value of the GTL project. The calculations have then shown that the GTL facility with three reactor stages (and optimized reactor lengths) presented the highest possible NPV value between all the possible plant configurations. Thus this project, having a positive NPV value, will be a profitable investment since the projected earnings exceed the anticipated costs.

Future works could improve the study done in this thesis by simulating both the GTL facility and the FT reactor with a greater level of detail, or even considering new plant configurations and reactor types to try to increase the overall profitability of the project; it should be noted that these changes could be easily implemented in the developed MATLAB and HYSYS simulations given the almost modular structure of the program code.

Bibliography

1. Sabatier, P. and J. Senderens, *Hebd.* Seances Acad. Sci, 1902. **134**: p. 680.
2. Fischer, F. and H. Tropsch, *Uber die Herstellung synthetischer olgemische (Synthol) durch Aufbau aus Kohlenoxyd und Wasserstoff.* Brennst. Chem, 1923. **4**: p. 276-285.
3. *U.S. Dept. Interior Bur. Mines Technical Paper 709 (1948).*
4. Dry, M.E., *Practical and theoretical aspects of the catalytic Fischer-Tropsch process.* Applied Catalysis A: General, 1996. **138**(2): p. 319-344.
5. Jager, B., *Developments in Fischer-Tropsch technology*, in *Studies in Surface Science and Catalysis*, D.S.F.F.A.V. A. Parmaliana and F. Arena, Editors. 1998, Elsevier. p. 25-34.
6. Herranz, T., et al., *Carbon oxide hydrogenation over silica-supported iron-based catalysts: Influence of the preparation route.* Applied Catalysis A: General, 2006. **308**: p. 19-30.
7. Wood, D.A., C. Nwaoha, and B.F. Towler, *Gas-to-liquids (GTL): A review of an industry offering several routes for monetizing natural gas.* Journal of Natural Gas Science and Engineering, 2012. **9**: p. 196-208.
8. Rahmim, I.I. *Gas-to-liquid technologies: recent advances, economics, prospects*. in *26th IAEE Annual International Conference, Prague, June*. 2003.
9. Minnie, R., et al., *Where it all began.* Fundamentals of Gas to Liquids. 2nd ed. London: Petroleum Economist, 2005: p. 27-29.
10. de Klerk, A. *Gas-to-liquids conversion*. in *Natural Gas Conversion Technologies Workshop of ARPA-E. US Department of Energy, Houston, TX*. 2012.
11. Velasco, J.A., et al., *Gas to liquids: A technology for natural gas industrialization in Bolivia.* Journal of Natural Gas Science and Engineering, 2010. **2**(5): p. 222-228.
12. Steynberg, A. and M. Dry, *Fischer-Tropsch Technology*. 2004: Elsevier Science.
13. Pytte, T., *2005. GTL diesel: the way forward. In: Fundamentals of Gas to Liquids. 2nd ed. London: Petroleum Economist. Ch. 3.1, pp.32-35.*
14. Corke, M., *Securing a market. In: Fundamentals of Gas to Liquids.* second ed. Petroleum Economist, London, pp. 36e38 (Chapter 3.2).
15. Cherrillo, R.A., et al. *Shell Gas to Liquids in the context of a Future Fuel Strategy–Technical Marketing Aspects*. in *9th Diesel Engine Emissions Reduction Workshop. Newport, RI*. 2003.
16. Wood, D., *Consequences of a heavier and sourer barrel.* Petroleum Review vom April, 2007.

17. Herman, R.G., *Catalytic conversions of synthesis gas and alcohols to chemicals*. 2012: Springer Science & Business Media.
18. Seggiani, M., *Analisi e modellazione di processi e componenti per la produzione di syngas e combustibili liquidi da carbone.* 2011.
19. Van Der Laan, G.P. and A. Beenackers, *Kinetics and selectivity of the Fischer–Tropsch synthesis: a literature review.* Catalysis Reviews, 1999. **41**(3-4): p. 255-318.
20. Anderson, R.B., C.B. Lee, and J.C. Machiels, *The thermodynamics of the hydrogenation of oxides of carbon.* The Canadian Journal of Chemical Engineering, 1976. **54**(5): p. 590-594.
21. Zhang, Q., W. Deng, and Y. Wang, *Recent advances in understanding the key catalyst factors for Fischer-Tropsch synthesis.* Journal of Energy Chemistry, 2013. **22**(1): p. 27-38.
22. Zhao, Y.H., et al., *Carbon chain growth by formyl insertion on rhodium and cobalt catalysts in syngas conversion.* Angewandte Chemie International Edition, 2011. **50**(23): p. 5335-5338.
23. Cao, D.-B., et al., *Chain growth mechanism of Fischer–Tropsch synthesis on Fe 5 C 2 (001).* Journal of Molecular Catalysis A: Chemical, 2011. **346**(1): p. 55-69.
24. Cheng, J., et al., *Chain growth mechanism in Fischer-Tropsch synthesis: A DFT study of CC coupling over Ru, Fe, Rh, and Re surfaces.* The Journal of Physical Chemistry C, 2008. **112**(15): p. 6082-6086.
25. Lo, J.M. and T. Ziegler, *Theoretical studies of the formation and reactivity of C2 hydrocarbon species on the Fe (100) surface.* The Journal of Physical Chemistry C, 2007. **111**(35): p. 13149-13162.
26. Cheng, J., et al., *A quantitative determination of reaction mechanisms from density functional theory calculations: Fischer–Tropsch synthesis on flat and stepped cobalt surfaces.* Journal of Catalysis, 2008. **254**(2): p. 285-295.
27. Ciobîcă, I., et al., *Mechanisms for chain growth in Fischer–Tropsch synthesis over Ru (0001).* Journal of Catalysis, 2002. **212**(2): p. 136-144.
28. Todic, B., et al., *CO-insertion mechanism based kinetic model of the Fischer–Tropsch synthesis reaction over Re-promoted Co catalyst.* Catalysis Today, 2014. **228**: p. 32-39.
29. Storsæter, S., D. Chen, and A. Holmen, *Microkinetic modelling of the formation of C 1 and C 2 products in the Fischer–Tropsch synthesis over cobalt catalysts.* Surface Science, 2006. **600**(10): p. 2051-2063.
30. Pirola, C., *Novel supported iron based Fischer-Tropsch catalysts: Preparation, characterization and applications.*
31. Abelló, S. and D. Montané, *Exploring Iron-based Multifunctional Catalysts for Fischer–Tropsch Synthesis: A Review.* ChemSusChem, 2011. **4**(11): p. 1538-1556.
32. Torres Galvis, H.M. and K.P. de Jong, *Catalysts for production of lower olefins from synthesis gas: a review.* ACS catalysis, 2013. **3**(9): p. 2130-2149.
33. Janardanarao, M., *Direct catalytic conversion of synthesis gas to lower olefins.* Industrial & engineering chemistry research, 1990. **29**(9): p. 1735-1753.
34. Wang, C., L. Xu, and Q. Wang, *Review of directly producing light olefins via CO hydrogenation.* Journal of Natural Gas Chemistry, 2003. **12**(1): p. 10-16.

35. Bartholomew, C.H. and W.-H. Lee, *Effects of support on methane selectivity in cobalt-catalyzed Fischer-Tropsch synthesis: A kinetic model.* Studies in Surface Science and Catalysis, 2000. **130**: p. 1151-1156.
36. Sarup, B. and B. Wojciechowski, *Studies of the fischer-tropsch synthesis on a cobalt catalyst i. evaluation of product distribution parameters from experimental data.* The Canadian Journal of Chemical Engineering, 1988. **66**(5): p. 831-842.
37. Anderson, R.B., H. Kölbel, and M. Rálek, *The Fischer-Tropsch Synthesis*. 1984: Academic Pr.
38. Perego, C. and M. Ricci, *Diesel fuel from biomass.* Catalysis Science & Technology, 2012. **2**(9): p. 1776-1786.
39. Maitlis, P.M. and V. Zanotti, *The role of electrophilic species in the Fischer-Tropsch reaction.* Chemical Communications, 2009(13): p. 1619-1634.
40. Perego, C., R. Bortolo, and R. Zennaro, *Gas to liquids technologies for natural gas reserves valorization: The Eni experience.* Catalysis Today, 2009. **142**(1–2): p. 9-16.
41. Khodakov, A.Y., W. Chu, and P. Fongarland, *Advances in the Development of Novel Cobalt Fischer−Tropsch Catalysts for Synthesis of Long-Chain Hydrocarbons and Clean Fuels.* Chemical Reviews, 2007. **107**(5): p. 1692-1744.
42. Steynberg, A.P., et al., *High temperature Fischer–Tropsch synthesis in commercial practice.* Applied Catalysis A: General, 1999. **186**(1–2): p. 41-54.
43. Dry, M., *The Fischer-Tropsch Synthesis in Catalysis Sciences and Technology, Anderson, JR and Boudart, M.,(Eds.) 1*, 1981, Springer Verlag, Berlin.
44. *Ministero delle attività produttive: il processo GTL e la gassificazione dei combustibili solidi.*, 2006.
45. Pirola, C., et al., *High Loading Fe-supported Fischer–Tropsch Catalysts: Optimization of the Catalyst Performance.* Catalysis Letters, 2009. **131**(1): p. 294-304.
46. Pirola, C., et al., *Fischer Tropsch and Water Gas Shift chemical regimes on supported iron-based catalysts at high metal loading.* Catalysis Communications, 2009. **10**(6): p. 823-827.
47. Comazzi, A., *Catalizzatori a base di Fe o Co per la sintesi di Fischer-Tropsch: risultati sperimentali e relativa modellazione*, 2013, Università degli Studi di Milano.
48. van der Laan, G.P. and A.A.C.M. Beenackers, *Intrinsic kinetics of the gas–solid Fischer–Tropsch and water gas shift reactions over a precipitated iron catalyst.* Applied Catalysis A: General, 2000. **193**(1–2): p. 39-53.
49. Lox, E.S. and G.F. Froment, *Kinetics of the Fischer-Tropsch reaction on a precipitated promoted iron catalyst. 1. Experimental procedure and results.* Industrial & Engineering Chemistry Research, 1993. **32**(1): p. 61-70.
50. Lox, E.S. and G.F. Froment, *Kinetics of the Fischer-Tropsch reaction on a precipitated promoted iron catalyst. 2. Kinetic modeling.* Industrial & Engineering Chemistry Research, 1993. **32**(1): p. 71-82.
51. Zimmerman, W.H. and D.B. Bukur, *Reaction kinetics over iron catalysts used for the fischer-tropsch synthesis.* The Canadian Journal of Chemical Engineering, 1990. **68**(2): p. 292-301.
52. Marano, J.J. and G.D. Holder, *Characterization of Fischer-Tropsch liquids for vapor-liquid equilibria calculations.* Fluid Phase Equilibria, 1997. **138**(1–2): p. 1-21.

53. Rafiee, A. and M. Hillestad, *Staging of the Fischer–Tropsch reactor with an iron based catalyst.* Computers and Chemical Engineering, 2012. **39**: p. 75-83.
54. Marano, J.J. and G.D. Holder, *General Equation for Correlating the Thermophysical Properties of n-Paraffins, n-Olefins, and Other Homologous Series. 1. Formalism for Developing Asymptotic Behavior Correlations.* Industrial & Engineering Chemistry Research, 1997. **36**(5): p. 1887-1894.
55. Marano, J.J. and G.D. Holder, *General Equation for Correlating the Thermophysical Properties of n-Paraffins, n-Olefins, and Other Homologous Series. 2. Asymptotic Behavior Correlations for PVT Properties.* Industrial & Engineering Chemistry Research, 1997. **36**(5): p. 1895-1907.
56. Marano, J.J. and G.D. Holder, *A General Equation for Correlating the Thermophysical Properties of n-Paraffins, n-Olefins, and Other Homologous Series. 3. Asymptotic Behavior Correlations for Thermal and Transport Properties.* Industrial & Engineering Chemistry Research, 1997. **36**(6): p. 2399-2408.
57. Green, D. and R. Perry, *Perry's Chemical Engineers' Handbook, Eighth Edition*. 2007: McGraw-Hill Education.
58. Chaumette, P., C. Verdon, and P. Boucot, *Influence of the hydrocarbons distribution on the heat produced during Fischer-Tropsch synthesis.* Topics in Catalysis. **2**(1): p. 301-311.
59. Wen, D. and Y. Ding, *Heat transfer of gas flow through a packed bed.* Chemical Engineering Science, 2006. **61**(11): p. 3532-3542.
60. Jianmin, W., et al., *Diffusion and Reaction Model of Catalyst Pellets for Fischer-Tropsch Synthesis.* China Petrol Proc & Petrochem Techn, 2013. **15**: p. 77-86.
61. Boston, J.F. and H.I. Britt, *A radically different formulation and solution of the single-stage flash problem.* Computers & Chemical Engineering, 1978. **2**(2–3): p. 109-122.
62. Hillestad, M., *Modeling the Fischer-Tropsch product distribution and model implementation.* 2014.
63. Baltrusaitis, J. and W.L. Luyben, *Methane Conversion to Syngas for Gas-to-Liquids (GTL): Is Sustainable CO2 Reuse via Dry Methane Reforming (DMR) Cost Competitive with SMR and ATR Processes?* ACS Sustainable Chemistry & Engineering, 2015. **3**(9): p. 2100-2111.
64. Couper, J.R., *Process Engineering Economics*. 2003: CRC Press.
65. Guthrie, K., *Process Plant Estimating Evaluation and Control Craftsman.* Solana Beach, Calif, 1974.
66. Guthrie, K.M., *Data and techniques for preliminary capital cost estimating.* Chemical Engineering, 1969. **76**(6): p. 114-&.
67. Ulrich, G.D., *A guide to chemical engineering process design and economics*. 1984: Wiley New York.
68. Navarrete, P.F. and W.C. Cole, *Planning, estimating, and control of chemical construction projects*. 2001: CRC Press.
69. Turton, R., et al., *Analysis, Synthesis and Design of Chemical Processes*. 2008: Pearson Education.
70. Chemical Engineering, (May 2015): p. 104.
71. Alptekin, G.O., et al., *Oxygen Sorbents for Oxy-Fuel Combustion*, in *AIChE Annual Meeting 2008*: Philadelphia, PA.

72. *https://www.eia.gov/dnav/ng/ng_pri_sum_dcu_nus_m.htm*.
73. *OPEC Annual Statistical Bulletin*. Available from: http://www.opec.org/opec_web/en/publications/202.htm.
74. Tong, Y., *Cost analysis and evaluation os syngas synthesis through anaerobic digestion*, 2012, University of Dayton, OH.
75. Rafiee, A. and M. Hillestad, *Techno-Economic Analysis of a Gas-to-Liquid Process with Different Placements of a CO2 Removal Unit.* Chemical Engineering & Technology, 2012. **35**(3): p. 420-430.

Appendix A – Kinetic Parameters

The parameters of all the equations used in section 3.2 are reported in this appendix. The chain growth probability α_{ASF} is calculated based on the correlation developed by Lox and Froment [49, 50]:

$$\alpha_{ASF} = \frac{k_1 P_{CO}}{k_1 P_{CO} + k_2 P_{H_2} + k_3} \tag{A.1}$$

where the k_i parameters are given by:

$$k_i = k_{ref,i} \exp\left(-\frac{E_{act,i}}{R_{gas}} \left(\frac{1}{T} - \frac{1}{T_{ref}} \right) \right) \tag{A.2}$$

The values of the parameters for the α_{ASF} are reported in Table A.1 ($T_{ref} = 573K$):

Table A.1 - Parameters values for the chain growth probability evaluation

Parameter	Value	Unit of measure
k_1	1.22×10^{-10}	$kmol/(kg \cdot s \cdot Pa)$
k_2	1.05×10^{-11}	$kmol/(kg \cdot s \cdot Pa)$
k_3	2.36×10^{-6}	$kmol/(kg \cdot s)$
E_1	$0.$	kJ/mol
E_2	94.5	kJ/mol
E_3	132.3	kJ/mol

The parameters values of the FT and WGS reaction rates that have been examined in this thesis are now reported. The kinetic constants k_i (k_{FT} and k_{WGS}) of the reaction models have all the following form:

$$k_i = k_i^0 \exp\left(-\frac{E_{act,i}}{R_{gas}T}\right) \tag{A.3}$$

while the WGS equilibrium constant is given by $K_P = \exp^{\left(\frac{4578}{T}-4.33\right)}$.

Reaction set proposed by Zimmerman and Bukur [51]:

$$r_{FT_{ZB}} = k_{FT}\frac{P_{H_2}P_{CO}}{P_{CO}+a_{FT}P_{H_2O}+b_{FT}P_{CO_2}} \tag{A.4}$$

Table A.2 - Kinetic parameters of the FT reaction proposed by Zimmerman and Bukur

Parameter	**Value**	**Unit of measure**
k_{FT}^0	8.58	$mol/(kg \cdot s \cdot Pa)$
$E_{act,FT}$	8.6×10^4	J/mol
a_{FT}	4.8	Pa^{-1}
b_{FT}	0.33	Pa^{-1}

$$r_{WGS_{ZB}} = k_{WGS}\frac{P_{CO}P_{H_2O}-\dfrac{P_{H_2}P_{CO_2}}{K_p}}{P_{CO}+a_{WGS}P_{H_2O}+b_{WGS}P_{CO_2}} \tag{A.5}$$

Table A.3 - Kinetic parameters of the WGS reaction proposed by Zimmerman and Bukur

Parameter	**Value**	**Unit of measure**
k_{FT}^0	9.33×10^6	$mol/(kg \cdot s \cdot Pa)$
$E_{act,FT}$	1.32×10^5	J/mol
a_{FT}	21	Pa^{-1}
b_{FT}	0.	Pa^{-1}

Reactions sets proposed by van der Laan and Beenackers [48]:

$$r_{FT_{VB-I}} = k_{FT} \frac{P_{H_2}^{0.5} P_{CO}}{\left(1 + a_{FT} P_{CO} + b_{FT} P_{H_2O}\right)^2} \tag{A.6}$$

Table A.4 - Kinetic parameters of the first FT reaction proposed by van der Laan and Beenackers

Parameter	**Value**	**Unit of measure**
k_{FT}^0	4.88×10^{-11}	$mol/\left(kg \cdot s \cdot Pa^{-1.5}\right)$
$E_{act,FT}$	$1. \times 10^3$	J/mol
a_{FT}	5.63×10^{-7}	Pa^{-1}
b_{FT}	4.05×10^{-6}	Pa^{-1}

$$r_{FT_{VB-II}} = k_{FT} \frac{P_{H_2} P_{CO}}{\left(1 + a_{FT} P_{CO} + b_{FT} P_{H_2O}\right)^2} \tag{A.7}$$

Table A.5 - Kinetic parameters of the second FT reaction proposed by van der Laan and Beenackers

Parameter	**Value**	**Unit of measure**
k_{FT}^0	5.56×10^{-14}	$mol/\left(kg \cdot s \cdot Pa^{-2}\right)$
$E_{act,FT}$	$1. \times 10^3$	J/mol
a_{FT}	1.25×10^{-7}	Pa^{-1}
b_{FT}	$7. \times 10^{-6}$	Pa^{-1}

$$r_{FT_{VB-III}} = k_{FT} \frac{P_{H_2} P_{CO}}{1 + a_{FT} P_{CO} + b_{FT} P_{H_2O}} \tag{A.8}$$

Table A.6 - Kinetic parameters of the third FT reaction proposed by van der Laan and Beenackers

Parameter	**Value**	**Unit of measure**
k_{FT}^{0}	7.79×10^{-14}	$mol/\left(kg\cdot s\cdot Pa^{-2}\right)$
$E_{act,FT}$	$1.\times10^{3}$	J/mol
a_{FT}	5.36×10^{-7}	Pa^{-1}
b_{FT}	3.227×10^{-5}	Pa^{-1}

$$r_{WGS_{VB-I}} = k_{WGS}\frac{P_{CO}P_{H_2O} - \dfrac{P_{H_2}P_{CO_2}}{K_p}}{\left(1 + a_{WGS}P_{CO} + b_{WGS}P_{H_2O}\right)^2} \tag{A.9}$$

Table A.7 - Kinetic parameters of the first WGS reaction proposed by van der Laan and Beenackers

Parameter	**Value**	**Unit of measure**
k_{WGS}^{0}	1.77×10^{-12}	$mol/\left(kg\cdot s\cdot Pa^{-2}\right)$
$E_{act,\mathrm{WGS}}$	$1.\times10^{3}$	J/mol
a_{WGS}	2.1×10^{-6}	Pa^{-1}
b_{WGS}	2.419×10^{-5}	Pa^{-1}

$$r_{WGS_{VB-II}} = k_{WGS}\frac{\dfrac{P_{CO}P_{H_2O}}{P_{H_2}^{0.5}} - \dfrac{P_{H_2}^{0.5}P_{CO_2}}{K_p}}{\left(1 + a_{WGS}P_{CO} + b_{WGS}P_{H_2O}\right)^2} \tag{A.10}$$

Table A.8 - Kinetic parameters of the second WGS reaction proposed by van der Laan and Beenackers

Parameter	**Value**	**Unit of measure**
k_{WGS}^{0}	1.13×10^{-9}	$mol/\left(kg\cdot s\cdot Pa^{-1.5}\right)$
$E_{act,\mathrm{WGS}}$	$1.\times10^{3}$	J/mol
a_{WGS}	2.78×10^{-6}	Pa^{-1}
b_{WGS}	1.227×10^{-5}	Pa^{-1}

It should be noted that the kinetic constants k_i proposed by van der Laan and Beenackers had no activation energies values since they were derived at a constant temperature of 523 K. To take in consideration the temperature dependence of these reactions it has therefore been decided to consider a standard energy of activation of $1.\times10^3\ J/mol$, whose value is then regressed using the experimental data.

Appendix B – Boston and Britt algorithm

The Boston and Britt [61] equations introduced in section 4.4 for the flash and dew point calculations are here shown in detail. The algorithm proposed by Boston and Britt removes the need of an initial guess for phase composition close to the solution. The new variable introduced in the outer loop is:

$$u_i = \ln\left(\frac{k_i}{k_b}\right) \tag{B.1}$$

where k_i are the equilibrium constants and k_b is given by a weighted average:

$$\ln(k_b) = \sum_{i=1}^{N_{comp}} w_i \cdot \ln(k_i) \tag{B.2}$$

The weights w_i used to solve a flash with known pressure and vapour flow rate values, as is the case for the calculation of the dew point temperature of the mixture, are given by the following formula:

$$w_i = \frac{t_i}{\sum_{i=1}^{N_{comp}} t_i} \tag{B.3}$$

where t_i is:

$$t_i = \frac{V \cdot y_i}{1-\beta+\beta \cdot k_i} \tag{B.4}$$

The dependence of k_b on the temperature is represented by the model:

$$\ln\left(k_b\right) = A + B\left(\frac{1}{T} - \frac{1}{T_{ref}}\right) \tag{B.5}$$

where T_{ref} is a reference temperature, e.g. 298.15 K. The parameters A and B are obtained by evaluating k_b at two different temperatures, T and T':

$$B = \frac{\ln\left(k_b'/k_b\right)}{\frac{1}{T} - \frac{1}{T'}} \tag{B.6}$$

$$A = \ln\left(k_b\right) - B\left(\frac{1}{T} - \frac{1}{T_{ref}}\right) \tag{B.7}$$

The variables used in the inner loop are:

$$R = \frac{k_b \cdot V}{k_b \cdot V + k_b^0 \cdot L} \tag{B.8}$$

$$p_i = \frac{L \cdot x_i}{1 - R} \tag{B.9}$$

The traditional VLE equations are then rearranged introducing these just mentioned variables:

- The material balance for each component is combined with the phase equilibrium equation ($y_i = k_b \cdot e^{u_i} \cdot x_i$) to provide another expression for p_i:

$$p_i = \frac{F \cdot z_i}{1 - R + k_b^0 \cdot R \cdot e^{u_i}} \tag{B.10}$$

- With the constitutive equation ($\sum_{i=1}^{N_{comp}} y_i - \sum_{i=1}^{N_{comp}} x_i = 0$), k_b can be also obtained by:

$$k_b = \frac{\sum_{i=1}^{N_{comp}} p_i}{\sum_{i=1}^{N_{comp}} e^{u_i} \cdot p_i} \tag{B.11}$$

- The liquid flow rate L is given by the sum of all the p_i values:

$$L = \left(1 - R\right) \sum_{i=1}^{N_{comp}} p_i \tag{B.12}$$

The vapour flow rate V is obtained from the global material balance, while the phase compositions are given by:

$$x_i = \frac{p_i}{\sum_{i=1}^{N_{comp}} p_i} \tag{B.13}$$

$$y_i = \frac{e^{u_i} \cdot p_i}{\sum_{i=1}^{N_{comp}} e^{u_i} \cdot p_i} \tag{B.14}$$

The Boston and Britt algorithm is used at each integration step of the reactor model to first calculate the dew point temperature of the mixture (solving a flash problem with known pressure and vapour flow rate); if the dew point temperature found is higher than the reactor temperature, then another flash evaluation (with known temperature and pressure) is performed to quantify the liquid and vapour phases flow rates and compositions.

The main difference between the two algorithms used, the first for the dew point temperature evaluation and the second for the flash calculation, is that in the latter the temperature is a specified quantity and, therefore, the model for k_b is not needed.

Appendix C – Plant Costs

In this appendix are reported the equipment costs for the syngas production section of the plant, taken from Baltrusaitis and Luyben's study [63], and the equations used to estimate the costs of the remaining pieces of equipment used in the GTL project, taken from Turton et al. [69].

Syngas plant section cost

The equipment costs used for the syngas production section of the plant are shown in the following table:

Table C.1 - Equipment costs of the syngas production section

	Q [MW]	**Area [m^2]**	**Capital [10^6 \$]**
Preheater	14.55	461	0.3930
Vaporizer	8.31	89	0.1352
SMR	7.4	-	2.738
SMR catalyst	-	-	1.910
ATR	-	-	7.652
Cooler 1	159.8	1308	0.7743
Cooler 2	50.34	1646	0.8990
Cooler 3	47.57	3556	1.483

Purchased equipment costs

The purchased cost of the equipment is evaluated with the following equation:

$$\log_{10}\left(C_p^0\right) = K_1 + K_2\log_{10}\left(A\right) + K_3\left(\log_{10}\left(A\right)\right)^2 \tag{C.1}$$

where A is the capacity or size parameter for the equipment. The values for K_1, K_2 and K_3 required for this thesis are reported in Table C.2.

Table C.2 - Coefficients values for the purchased cost evaluation

Equipment type	**Equipment description**	K_1	K_2	K_3	A **parameter**
Compressors	Centrifugal, axial and reciprocating	2.2897	1.3604	-0.1027	Fluid power, kW
	Rotary	5.0355	-1.8002	0.8253	
Heat exchangers	Floating head	4.8306	-0.8509	0.3187	Area, m^2
	Fixed tube	4.3247	-0.3030	0.1634	
	Kettle reboiler	4.4646	-0.5277	0.3955	
Heaters	Hot water heater	2.0829	0.9074	-0.0243	Duty, kW
	Steam boiler	6.9617	-1.4800	0.3161	
Process vessels	Horizontal	3.5565	0.3776	0.0905	Volume, m^3
	Vertical	3.4974	0.4485	0.1074	
Pumps	Reciprocating	3.8696	0.3161	0.1220	Shaft power, kW
	Centrifugal	3.3892	0.0536	0.1538	

Pressure factors

The costs of equipment increase with increasing operating pressure. These changes are accounted through the use of pressure factors F_P. The pressure factor for horizontal and vertical process vessels of diameter D meters and operating at a pressure of P barg is first considered. At base material conditions, using carbon steel with a maximum allowable stress S of 944 bar, a weld efficiency E of 0.9, a minimum allowable vessel thickness of 0.0063 m and a corrosion allowance CA of 0.00315, the pressure factor is given by the following formula:

$$F_{P,vessel} = \frac{\frac{(P+1)D}{2(850-0.6(P+1))} + 0.00315}{0.0063} \quad for \quad t_{vessel} > 0.0063m \tag{C.2}$$

If $F_{P,vessel}$ is less than 1 (corresponding to a value of $t_{vessel} < 0.0063m$) then $F_{P,vessel} = 1$. For pressures less than -0.5 barg the $F_{P,vessel}$ value is instead set to 1.25.

The pressure factors for other process equipment are given by the following general form:

$$\log_{10}(F_P) = C_1 + C_2 \log_{10}(P) + C_3 (\log_{10}(P))^2 \tag{C.3}$$

The unit of measure of pressure used is the bar gauge or barg (with 1 bar equal to 0 barg). The coefficient values C are listed in Table C.3.

Table C.3 – Coefficients values for the pressure factor evaluation

Equipment type	**Equipment description**	C_1	C_2	C_3	**Pressure range (barg)**
Compressors	Centrifugal, axial, rotary and reciprocating	0	0	0	-
Heat exchangers	Floating head, fixed tube, kettle reboiler	0	0	0	P < 5
		0.03881	-0.11272	0.08183	5 < P < 140
Heaters	Hot water heater	0	0	0	P < 2
		-0.01633	0.056875	-0.00876	2 < P < 200
	Steam boiler	0	0	0	P < 20
		2.594072	-4.23476	1.722404	20 < P < 40
Process vessels	Horizontal and vertical	Equation C.3			
Pumps	Reciprocating	0	0	0	P < 10
		-0.245382	0.259016	-0.01363	10 < P < 100
	Centrifugal	0	0	0	P < 10
		-0.3935	0.3957	-0.00226	10 < P < 100

Material factors and bare module factors

The costs of equipment changes with the MOC chosen. This variation in costs is evaluated through the use of a material factor F_M and a bare module factor F_{BM}. These factors, together with the pressure factor, allow to calculate the bare module cost C_{BM} of the equipment.

Bare module cost for heat exchangers, process vessels and pumps

The material factors for heat exchangers, process vessels and pumps are given in Table C.4. The bare module factor values for these types of equipment are calculated with the following expression:

$$F_{BM} = B_1 + B_2 \cdot F_M \cdot F_P \tag{C.4}$$

where the values of the B constants are given in Table C.5. The bare module cost is then evaluated:

$$C_{BM} = C_p^0 \cdot F_{BM} = C_p^0 \left(B_1 + B_2 \cdot F_M \cdot F_P \right) \tag{C.5}$$

Table C.4 – Coefficients values of the bare module factor for heat exchangers, process vessels and pumps

Equipment type	**Equipment description**	B_1	B_2
Heat exchangers	Floating head, fixed tube and kettle reboiler	1.63	1.66
Process vessels	Horizontal	1.49	1.52
	Vertical	2.25	1.82
Pumps	Reciprocating	1.89	1.35
	Centrifugal	1.89	1.35

Table C.5 - Material factors for heat exchangers, process vessels and pumps

Equipment type	Equipment description	MOC	F_M
Heat exchangers	Floating head, fixed tube and kettle reboiler	CS-shell/CS-tube	1.00
		CS-shell/Cu-tube	1.35
		Cu-shell/Cu-tube	1.65
		CS-shell/SS-tube	1.80
		SS-shell/SS-tube	2.75
		CS-shell/Ni alloy tube	2.65
		Ni alloy shell/Ni alloy tube	3.75
		CS-shell/Ti-tube	4.65
		Ti-shell/Ti-tube	11.35
Process vessels	Horizontal and vertical	CS	1.00
		SS clad	1.75
		SS	3.10
		Ni alloy clad	3.60
		Ni alloy	7.05
		Ti clad	4.65
		Ti	9.40
Pumps	Reciprocating	Cast iron	1.00
		CS	1.45
		Cu alloy	1.25
		SS	2.35
		Ni alloy	3.95
		Ti	6.45
	Centrifugal	Cast iron	1.00
		CS	1.55
		SS	2.25
		Ni alloy	4.35

Bare module cost for the remaining process equipment

The bare module costs for the remaining types of equipment used in this dissertation are calculated as follows:

- Compressors

$$C_{BM} = C_p^0 \cdot F_{BM} \tag{C.6}$$

- Fired heaters and furnaces:

$$C_{BM} = C_p^0 \cdot F_{BM} \cdot F_P \cdot F_T \tag{C.7}$$

where F_T is the superheat correction for steam boilers (equal to 1 for other heaters and furnaces).

The bare module factors F_{BM} for these equations are reported in Table C.6.

Table C.6 – Bare module factors for the remaining process equipment

Equipment type	**Equipment description**	**MOC**	F_{BM}
Compressors	Centrifugal	CS	2.70
		SS	5.70
		Ni alloy	11.45
	Axial	CS	3.80
		SS	8.00
		Ni alloy	15.90
	Reciprocating	CS	3.40
		SS	7.00
		Ni alloy	13.90
Fired heaters and furnaces	Tube for furnaces and nonreactive process heater	CS	2.10
		Alloy steel	2.50
		SS	2.80

Appendix D – Program Code

In this appendix are reported parts of the program code written in MATLAB that might be useful in future works.

MATLAB and HYSYS interface

The simulation of the GTL plant seen in chapter 5 has only been possible thanks to the connection between MATLAB® R2014a and Aspen HYSYS® Version 8.4. To allow the exchange of information needed for the simulation, MATLAB is used as an activeX controller for HYSYS. This can be simply done using the following lines of MATLAB code:

```
% Create an ActiveX server
hyServer     = actxserver('Hysys.Application');

% Call the active simulation HYSYS case
hyCase       = hyServer.Activedocument;

% Call HYSYS solver
hySolver     = hyCase.Solver;

% Call the current HYSYS case flowsheet
hyFlowsheet  = hyCase.Flowsheet;

% Access the material streams of the HYSYS case
hyMatStreams = hyFlowsheet.MaterialStreams;

% Access operations of the HYSYS case
hyOperations = hyFlowsheet.Operations;

% Access energy streams of the HYSYS case
hyEneStreams = hyFlowsheet.EnergyStreams;
```

At this point MATLAB can import many values from the HYSYS flowsheet as shown below:

```
% Mass flow value of a stream in [kg/s]
mTOT = hyMatStreams.Item('Stream_Name').MassFlowValue;

% Molar flow value of a stream in [kmol/s]
F    = hyMatStreams.Item('Stream_Name').MolarFlowValue;

% Temperature value of a stream in [°C]
T    = hyMatStreams.Item('Stream_Name').TemperatureValue;

% Pressure value of a stream in [kPa]
P    = hyMatStreams.Item('Stream_Name').PressureValue;

% Power value of an energy stream in [kW]
Power=hyEneStreams.Item('Stream_Name').PowerValue;

% Mass composition of a stream
w    = hyMatStreams.Item('Stream_Name').ComponentMassFractionValue;

% Molar composition of a stream
z    = hyMatStreams.Item('Stream_Name').ComponentMolarFractionValue;
```

Likewise, MATLAB can also send values to the HYSYS flowsheet; in this situation MATLAB stops the HYSYS solver until all the new values are communicated:

```
% Stop HYSYS solver
hySolver.CanSolve=0;

% Mass flow value of the stream set in [kg/s]
hyMatStreams.Item('Stream_Name').MassFlowValue    = mTOT;

% Molar flow value of the stream set in [kmol/s]
hyMatStreams.Item('Stream_Name').MolarFlowValue   = F;

% Pressure value of the stream set in [kPa]
hyMatStreams.Item('Stream_Name').PressureValue    = P;

% Temperature value of the stream set in [°C]
hyMatStreams.Item('Stream_Name').TemperatureValue = T;

% Power value of the energy stream set in [kW]
hyEneStreams.Item('Stream_Name').PowerValue       = Power;

% Run HYSYS solver
hySolver.CanSolve=1;
```

It should be noted that since the composition of a stream cannot be directly communicated to HYSYS, the flow rates values of each component are first sent to a set of pure streams in HYSYS, which are then gathered in a single stream.

Catalyst effectiveness factor approximation

To speed up the plant optimization, the catalyst effectiveness factors of the FT and WGS reaction are calculated for various combinations of compositions ($y_{H_2}, y_{CO}, y_{H_2O}, y_{CO_2}, y_{inert}$), temperatures and pressures, and then collected in two multidimensional arrays, one for each reaction efficiency. The program written is the following:

```
function Pellet_Approximation
global n NcPellet Deff P0init

% Hydrogen molar composition values
yH2i=[];
for i=0.3:0.02:0.7
yH2i=[yH2i i];
end
lengthH2=length(yH2i);

% Carbon monoxide molar composition values
yCOi=[];
for i=0.001:0.01:0.401
yCOi=[yCOi i];
end
lengthCO=length(yCOi);

% Water molar composition values
yH2Oi=[];
for i=0.001:0.001:0.061
yH2Oi=[yH2Oi i];
end
lengthH2O=length(yH2Oi);

% Carbon dioxide molar composition values
yCO2i=[];
for i=0.001:0.01:0.251
yCO2i=[yCO2i i];
end
lengthCO2=length(yCO2i);

% Temperature values
Ti=[];
```

```
for i=513.15:0.5:516.15
Ti=[Ti i];
end
lengthT=length(Ti);

% Pressure values
Pi=[];
for i=1500000:500000:2500000
Pi=[Pi i];
end
lengthP=length(Pi);

% Preallocation of the efficiency arrays
etaFTi=zeros(lengthH2,lengthCO,lengthH2O,lengthCO2,lengthT,lengthP);
etaWGSi=etaFTi;

% Preallocation of the molar fraction vector
yi=[];

% Loop for every possible composition-T-P combination
for i=1:lengthH2
    for j=1:lengthCO
        for k=1:lengthH2O
            for l=1:lengthCO2
                for m=1:lengthT
                    for o=1:lengthP

% Input Variables for each iteration
% y = molar fraction of H2, CO, H2O, CO2 (row vector)
% T = temperature [K]
% P = pressure [Pa]

yi(1) = yH2i(i);
yi(2) = yCOi(j);
yi(3) = yH2Oi(k);
yi(4) = yCO2i(l);
T     = Ti(m);
P     = Pi(o);

% Check if sum of molar fraction <=1
SumFrac=yi(1)+yi(2)+yi(3)+yi(4);

if SumFrac>1
    etaFTi(i,j,k,l,m,o)  = 0;
    etaWGSi(i,j,k,l,m,o) = 0;
else

% Efficiency factor calculation

% Number of components
NcPellet=5;

% Interior collocation points
n=14;
[r,A,B,q]=colloc(n,1,1);

% Diffusion coefficients
```

```
DCO=5.584e-7*exp(-1786.29/T);
DH2=1.085e-6*exp(-1624.63/T);
DCO2=3.449e-7*exp(-1613.65/T);
DH2O=DCO+(DH2-DCO)/(2-28)*(18-28);
epsiP=0.30;
tort=3.5;
Deff=[DH2 DCO DH2O DCO2]*epsiP/tort; % [m^2/s]

% Superficial molar fractions: H2 CO H2O CO2 INERT
yS=[yi 1-sum(yi)];

% Initial molar fractions inside the pellet
y0=yS;

% Superficial partial pressures
P0init=P.*y0;

% Solving the DYNAMIC system, in order to give to fsolve a first guess
closer to the real solution of the system

% Initial STATE
y0Dyn=[ones(n+2,1)*y0(1); ones(n+2,1)*y0(2); ones(n+2,1)*y0(3);
ones(n+2,1)*y0(4); ones(n+2,1)*y0(5)];
tSpan=0:5:30;                    %[s]
% Mass matrix
M=eye(5*(n+2));
M(1,1)=0;
M(n+2,n+2)=0;
M(n+3,n+3)=0;
M(2*(n+2),2*(n+2))=0;
M(2*(n+2)+1,2*(n+2)+1)=0;
M(3*(n+2),3*(n+2))=0;
M(3*(n+2)+1,3*(n+2)+1)=0;
M(4*(n+2),4*(n+2))=0;
M(4*(n+2)+1:end,4*(n+2)+1:end)=0;

optionsODE=odeset('RelTol',1e-8,'AbsTol',1e-
12,'Mass',M,'MassSingular','yes');
[t,yDyn]=ode15s(@(t,y)PelletDynBalance(t,y,T,P,r,A,B),tSpan,y0Dyn,optionsOD
E);

yH2fin=yDyn(end,1:n+2)';
yCOfin=yDyn(end,n+3:2*(n+2))';
yH2Ofin=yDyn(end,2*(n+2)+1:3*(n+2))';
yCO2fin=yDyn(end,3*(n+2)+1:4*(n+2))';
yINERTfin=yDyn(end,4*(n+2)+1:end)';

% Solving the STEADY STATE

%Initial GUESS
y0fsolve=[yH2fin yCOfin yH2Ofin yCO2fin yINERTfin];
optionsFSOLVE=optimset('MaxFunEvals',1e4,'MaxIter',1e4,'Display','Final');

y=fsolve(@(y)PelletBalance(y,T,P,r,A,B),y0fsolve,optionsFSOLVE);

% Superficial effectiveness factors
[rFTs, rWGSs]=React(yS,T,P);    % [mol/(kgCAT*s)]
```

```
if rWGSs==0
    rWGSs=1e-6;
end

% Effectiveness factors calculation
etaFT=0;
etaWGS=0;
for p=1:n+2
    [rFT, rWGS]=React(y(p,:),T,P);           %[mol/(kgCAT*s)]
    etaFT=etaFT+3/rFTs*(q(p)*rFT*r(p)^2);
    etaWGS=etaWGS+3/rWGSs*(q(p)*rWGS*r(p)^2);
end

% Assigning effectiveness factors values to the multidimensional arrays
etaFTi(i,j,k,l,m,o)=etaFT;
etaWGSi(i,j,k,l,m,o)=etaWGS;

                         end
                    end
                end
            end
        end
    end
end

% Saving the efficiency factor arrays
save EfficiencyArray etaFTi etaWGSi yH2i yCOi yH2Oi yCO2i Ti Pi
```

The effectiveness factors values can now be quickly obtained during the plant optimization by interpolating the multidimensional arrays elements:

```
% Efficiency factor values
etaFT=interpn(yH2i,yCOi,yH2Oi,yCO2i,Ti,etaFTi,yVap(1),yVap(2),yVap(3),yVap(
4),T);
etaWGS=interpn(yH2i,yCOi,yH2Oi,yCO2i,Ti,etaWGSi,yVap(1),yVap(2),yVap(3),yVa
p(4),T);
```

Ringraziamenti

Desidero innanzitutto ringraziare il mio relatore, il Prof. Flavio Manenti, per avermi proposto questo interessante lavoro di tesi, che mi ha permesso di mettere alla prova ed approfondire le competenze acquisite in tutti questi ultimi anni di università. Ringrazio poi il Prof. Carlo Pirola, per aver supervisionato e fornito utili consigli riguardo alla parte sperimentale della dissertazione. Ringrazio quindi il Prof. Magne Hillestad, per avermi aiutato a sviluppare il progetto di tesi durante la mia esperienza presso la Norwegian University of Science and Technology di Trondheim.

Grazie a Alberto, sempre disponibile a fornirmi qualsiasi informazione di cui avessi bisogno, e a Davide, per i preziosi consigli che mi hanno portato a terminare la tesi.

Grazie a Andrea, Antonio, Fabio, Francesco e Matteo, non solo semplici compagni di corso ma soprattutto grandi amici con cui ho condiviso bellissimi momenti dentro e fuori l’università.

Infine il ringraziamento più grande va ai miei genitori, a mio fratello e a mia sorella, sempre pronti ad aiutarmi e sostenermi; senza di voi non avrei mai potuto raggiungere questo traguardo.

Enea